Enhancing the Interlayer Bond in Printed Concrete Structures

Presented by:

Oliver Brochu
Gordon Murray
Paul Rivera

Submitted to:

Professor Nima Rahbar and the Worcester Polytechnic Institute Civil & Environmental Engineering Department in partial fulfillment of the requirements for the Degree of Bachelor of Science

2019-2020

Abstract

3D printing with concrete is a new, innovative technology with promising benefits for the construction industry. Additive manufacturing of concrete has the potential to save costs on labor, formwork, and material and is a more sustainable means of producing the built environment for the future. Although potential exists, there are many obstacles to overcome before concrete 3D printing can be applied on a construction scale. This project first aimed to determine an optimal mixture design for printable concrete by experimenting with two different viscosity modifying admixtures: Acti-Gel and polyacrylamide. Polyacrylamide, a polymer-based flocculent, was found to enhance the rheology and cohesiveness of concrete in doses as low as 0.6% by weight of binder. Secondly, this project investigated improvements to the interfacial bond between layers of concrete using a liquid adhesive and sinusoidal layer geometries. Although there was insufficient data to make specific conclusions on the ideal bond improvement, test results indicated an enhanced shear strength from the sinusoidal layer geometries and an enhanced tensile strength from the adhesive. Finally, scanning electron microscopy completed on the interface between printed layers with polyacrylamide revealed the polymer's microstructure bridging across the interface and anchoring to the hydrated C-S-H structure. It is concluded that polyacrylamide is the most suitable viscosity modifying admixture for printable concrete.

Acknowledgements

Our project team would like to recognize the contributions of a few individuals to this project. Firstly, we thank Professor Nima Rahbar for inspiring this research into the innovative field of concrete 3D printing. Without his guidance and technical knowledge, this project would not have been possible. Secondly, we acknowledge Jessica Rosewitz for her commitment to the success of this project. Without being asked, Jessica took on the role of co-advisor for this project aiding with lab work, sample preparation, technical analysis, and writing on a day to day basis. Her contributions to this project were selfless and impactful. Russell Lang assisted with lab work and the ordering of materials, and we acknowledge and thank him for his contributions. Finally, this group acknowledges Mason Guarino from SSG Pools for generously donating two admixtures for use in this project. As a member of the American Shotcrete Association, Mason also invited us to observe the shotcrete process on a construction site and provided information and advice which was critical to the success of this project.

Capstone design statement

Through research and iterative design, an economical mix design was developed for enhancing the performance of printed concrete in structural applications. The scope of the project included two main components. The project began with a literature review on the most current research and developments in the field of concrete 3D printing. It was discovered through our research that one of the main difficulties with printed structures is the lack of homogeneity between printed layers. In order to address this issue, our group devised a scope that encompassed first iterating different mix designs of concrete until an optimal and reproducible mixture was determined. The second portion of our project scope included testing two different methods of improving the bond between layers to increase the homogeneity of printed structures.

Within the project scope there were three overall design objectives. First, devise an optimal mixture design which could potentially be used for printing in the construction industry using sustainable and easily accessible materials. Second, test methods of interlayer bond enhancement to determine the effects of increasing the contact area and using a bonding adhesive at the layer interface. The final design objective was to use the results from the interlayer bond testing to develop a nozzle geometry capable of creating the optimal layer geometry for improving the interlayer bond.

In order to achieve our first objective of determining the optimal mix design for printing, we conducted an organized experimentation of trial mixture designs. The first trial mixtures began with base materials including cement, sand, silica fume, and water. Then, using an iterative approach, trial mixtures with various additives were evaluated and redesigned until a select number of suitable mixtures for printing were achieved for a specific admixture. Next, a new admixture was added, and the process was repeated, narrowing down on the best mix designs for printing. In total, 51 trial mixtures were evaluated, using various combinations of admixtures including superplasticizers, fibers, and viscosity modifying admixtures. Following experimentation, the most suitable mixtures were tested for the three critical properties of printable concrete: pumpability, extrudability, and buildability. Pumpability was assessed using a standard slump test; extrudability was evaluated using a prototype extrusion nozzle; and buildability was evaluated by performing a series of scaled-down slump tests at timed intervals. Four mix designs were chosen for further testing with viscometry and compression tests. The results were compiled, and one mix was chosen as the optimal mix design for 3D printing of concrete.

After the determination of the optimal mixture design, investigation of interlayer bond strength began. A modified version of the Brazilian disk test was used to evaluate the bond strength of samples created to simulate the interface between printed layers. The first method of interlayer bond improvement used was a common bonding adhesive applied to a flat interface. The second method investigated was a sinusoidal geometry at the interface between printed layers. Nine different sinusoidal shapes were investigated for their effects on bond strength. The Brazilian disk samples were tested at two different angles to understand the improvement to the interlayer bond in tension and shear. In total, 48 samples were tested, and the best improvement method was determined through analysis. The optimal sinusoidal shape was used to design a nozzle capable of extruding a filament of that shape.

The design of a printable concrete mixture and of an innovative nozzle geometry were done within realistic engineering constraints to maintain applicability to the construction industry. The development of a printable concrete was completed within the constraints of economy and sustainability. The availability and cost of the materials and admixtures chosen for the mixture designs were considered to ensure that the mix designs posed in this report could be economically produced on a construction scale.

Professional licensure statement

Professional licensure indicates that an engineer has a certain level of competency within his or her engineering discipline. For civil engineers, a professional engineering license allows an engineer to prepare, sign, and seal engineering plans and drawings. Licensure is a legal requirement for private and consulting engineers who are responsible for their work. It is also a requirement for many governmental engineering jobs as well as educational positions in many states.

However, professional licensure is not easily obtained. It is a long-term commitment that lasts for the entire career of a practicing engineer. To begin with, an engineer must complete at least a four-year college degree from an ABET-accredited engineering program and pass the Fundamentals of Engineering (FE) Exam to become an Engineer in Training (EIT). The FE exam is a six-hour exam comprised of 110 questions. Following this, an engineer has to accumulate four years of experience underneath a licensed professional engineer. Accurate records of this experience need to be kept and endorsed by a supervising professional engineer. These records are part of the review process as each state requires a detailed work history before the final step toward licensure can be taken: successful completion of Principles and Practice of Engineering (PE) exam. Once an engineer's credentials have been verified, he or she can register to take the PE exam. It is an eight-hour exam which consists of 80 questions covering all five areas of civil engineering: construction, geotechnical, structural, transportation, and water resources and environment. Both the FE and PE exams are organized by the National Council of Examiners for Engineering and Surveying (NCEES).

Once professional licensure is obtained, the process of maintaining licensure through continued industry education begins. Each state has varying requirements for maintaining professional licensure, but in 42 states, there is a certain standard of continued education that must be completed before an engineer's license can be renewed. There are online courses, conferences, webinars, and other forms of continuing education for professional engineers, all of which count for a certain number of Professional Development Hours (PDHs). Each state has its own requirements as to how many PDHs are needed to renew a license and how often an engineer needs to renew his or her license. It is important for a professional engineer to remain up to date on the requirements of any of the states within which he or she is registered. There is some reciprocity between states that allows engineers to obtain and maintain a PE license in multiple states, but in some instances the PE exam must be retaken to obtain a license in another state depending on the requirements.

Professional licensure is crucial for the public, the individual, and the civil engineering profession as a whole. Prior to 1907, no state regulated who was permitted to offer engineering services to the public. This meant that there was no standard method for designating who was and was not competent enough to practice as an engineer which was a significant danger to the public. However, in 1907, Wyoming passed the first engineering licensure law which established a minimum level of competency for engineers to protect the safety of the public and uphold a certain standard of ethics. Today, professional licensure continues to uphold the safety of the public. It is also beneficial to the individual. It enables engineers to take on more responsibility and often reach a higher and more lucrative position within the industry. Further, becoming a professional engineer opens the gate to a community of high achieving individuals and

resources that can help an engineer develop his or her career. It is a mark of integrity and achievement that sets an engineer apart in the industry. Finally, professional licensure is beneficial to the civil engineering profession as it ensures that the field of civil engineering continues to develop and grow, continually reaching higher standards of safety and creativity.

Table of contents

List of figures

List of tables

1. Introduction

1.1. Additive manufacturing in the construction sector

As the demand for sustainability grows, carbon emissions and material waste associated with construction are increasing concerns to the world population. To put it into perspective, the industry consumes 50% of the global steel production and is responsible for 30% of the world's greenhouse gas emissions (Craveiro, Duarte, Bártolo, & Bártolo, 2019). These concerns demand for new technologies that are capable of addressing these environmental issues by producing a more sustainable means of constructing the built environment. The construction industry has great potential for growth in terms of sustainability and efficiency. Typically, it is considered to lag behind other industries in terms of adopting new technological trends (Wangler, Roussel, Bos, Salet, & Flatt, 2019). This is because the construction industry continues to rely, overwhelmingly, on traditional craft-based methods (Craveiro et al., 2019). However, in recent years, there have been signs that the industry is taking strides towards digitalization. One example of digitalization and automation within the construction industry can be seen in the fabrication process of modular precast components. Many precasting plants have fully automated the production of modular building components such as hollow cast floors, decreasing fabrication and construction times (Seraderian, 2019). Building information modeling (BIM) is another innovation that has become widely used in the construction sector; it has revolutionized the way that buildings are visualized from the design and construction phases into operation and maintenance (Craveiro et al., 2019; Wangler et al., 2019). The adoption of new technology and automated processes opens the gate for further digitalization and automation within the construction industry.

Concrete is by far the most economical and environmentally-friendly building material when compared to other materials such as steel and wood (Scrivener, John, & Gartner, 2018). Consequently, concrete is the most viable construction material when it comes to meeting the growing demands for infrastructure and development across the globe. However, despite concrete's comparatively low carbon footprint, concrete production accounts for as high as 10% of global anthropogenic CO_2 emissions simply because of the sheer volume of concrete produced (Scrivener et al., 2018; Wangler et al., 2019). One can only expect that this number will rise as the demand for infrastructure continues to increase, unless alternate construction techniques are adopted. Additive manufacturing of concrete structures has the potential to help reduce carbon emissions through increased material and energy efficiency (De Schutter et al., 2018; Wangler et al., 2016; Wangler et al., 2019).

Additive manufacturing is a topic that has received much attention by researchers in recent decades with hopes of optimizing the production method for use in a number of industries. It has become a popular means of production in manufacturing and is being used on a daily basis to produce products from toys to aerospace parts and medical devices (Craveiro et al., 2019; De Schutter et al., 2018). The benefit of additive manufacturing and the reason for its rapid growth is its efficiency in terms of material, energy, and cost over the more traditional subtractive manufacturing methods. For the construction industry, concrete is a promising material for the purposes of additive manufacturing. Concrete is the most used construction material in the world for a number of reasons. The raw materials used in concrete production are available and easily accessible globally, and when compared to other building materials, the

production of concrete is relatively inexpensive (Wangler et al., 2019; Wangler, Nov 11, 2018). Further, the ability of concrete to behave as a liquid and mold to any shape and subsequently carry structural loads makes it a prolific construction material (Wangler et al., 2016; Wangler et al., 2019; Wangler, Nov 11, 2018). In particular, it is the ability of concrete to behave as a liquid before curing that makes it a viable additive material for improving efficiency in construction. In fact, engineers are already capable of designing material efficient concrete members with a method called topology optimization, and concrete 3D printing could allow for construction scale production of these optimized members.

Topology optimization is a design tool which aids engineers in creating more efficient structures in terms of shape for any given design domain. This is accomplished with a number of mathematical equations which are able to determine the underutilized areas of a structural member and remove material from these locations (Jewett & Carstensen, 2019). In essence, topology optimization generates designs with little to no wasted material, as can be seen below in Fig. 1. According to Jewett and Carstensen (Jewett & Carstensen, 2019), the designs stemming from topology optimization have also been shown to outperform conventional low-weight designs in terms of strength. Theoretically, topology optimization can improve design performance while minimizing the amount of wasted material. However, the feasibility of constructing these optimized designs still requires development because of their complexity and the inability of traditional formwork to cost-efficiently produce them (Jewett & Carstensen, 2019; Wangler et al., 2019). However, emerging technologies including CNC-milled formwork, fabric forming, and concrete 3D printing are quickly making the use of topology optimization in the industry feasible (Jewett & Carstensen, 2019).

Figure 1: Example of a topology optimized beam design taken from "Topology-optimized design, construction and experimental evaluation of concrete beams" (Jewett & Carstensen, 2019).

In addition to material efficiency, concrete 3D printing has the potential to greatly reduce the cost of construction which accounts for approximately six percent of the global GDP

(Craveiro, Duarte, Bártolo, & Bártolo, 2019). The use of formwork is costly, requiring large amounts of time, labor, and material. The costs associated with formwork can account for anywhere from a quarter to half of the total cost of concrete construction (De Schutter et al., 2018). Concrete 3D printing, however, can eliminate the use of formwork, thus it has the potential to greatly reduce construction expenses and increase construction speeds. Automation of the building process could also improve worker safety by replacing many of the dangerous construction jobs (Wangler et al., 2016). However, it should be noted that, although digitalization of concrete construction is a revolutionary development, concrete 3D printing is not without its limitations. For example, 3D printing and other methods of concrete additive manufacturing, in their current state of development, remain unable to surpass traditional formwork methods in terms of cost for low complexity designs (Labonnote & Rüther, 2016; Wangler et al., 2019). Figure two illustrates how the cost of digital concrete fabrication compares to that of conventional construction in regard to design complexity. Additionally, achieving a printable concrete mixture is a complex task, requiring a precise mix of admixtures and additives. Some admixtures are expensive and harmful to the environment, countering the potential goals of 3D printing, which are to reduce cost and environmental footprint (De Schutter et al., 2018). The following sections aim to outline the complex material demands of concrete 3D printing by extrusion and propose a cost-efficient and sustainable mixture design that can achieve these demands and perform in structural applications.

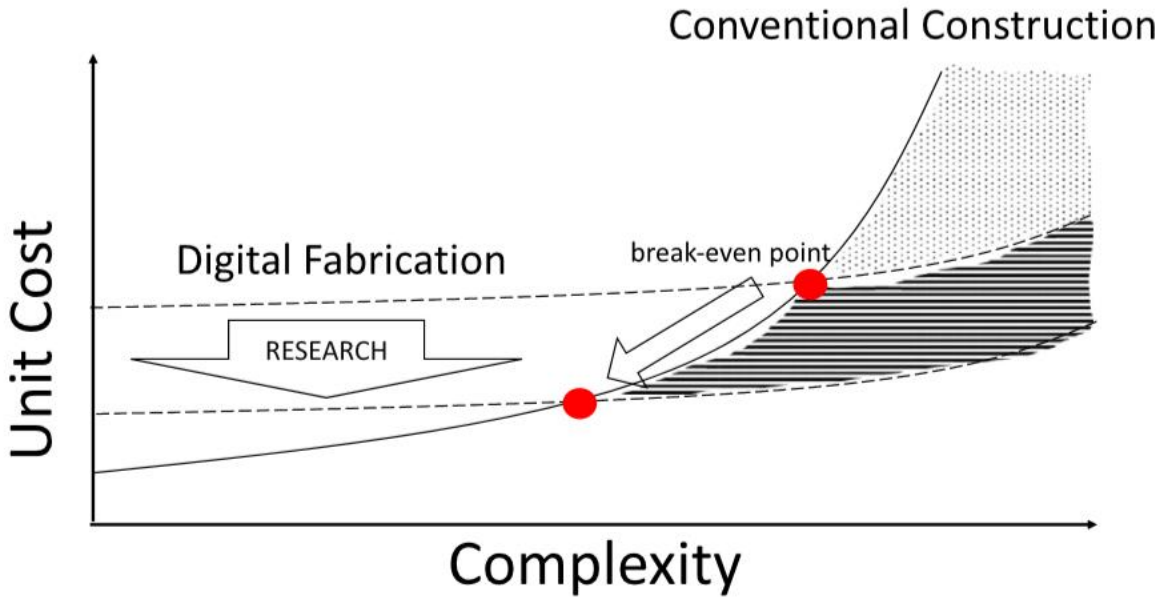

Figure 2: Graph, taken from "Digital concrete: A review" (Wangler et al., 2019), showing the cost of conventional construction (solid line) compared to that of digital fabrication (dotted line). Digital fabrication begins to outperform conventional construction.

2. Background

2.1. Rheological requirements for printable concrete

Before discussing the specifics of concrete 3D printing, the general process along with the fundamental terminology needs to be defined. This paper focuses on concrete 3D printing by extrusion. However, it should be noted that there are other methods of concrete 3D printing including slipforming and controlled casting (Wangler, Nov 11, 2018). Figure three provides a general schematic of concrete 3D printing by extrusion. The first step in any concrete printing process is the mixing of the fresh concrete. The fresh concrete is then added to a hopper which feeds a pump. The mixing process can also be automated, constantly mixing fresh concrete in a hopper and delivering it to the pumping system. In the pumping stage, the fresh concrete then moves through a tube to the extrusion nozzle. Once the fresh concrete reaches the nozzle, it moves to the second stage, extrusion. In some printing processes, a quick acting accelerator is added at the nozzle. This process, called inline mixing, will be discussed in section 2.4.4. The concrete is extruded as a filament with height, h, which depends on the geometry of the nozzle. At this stage, the fresh concrete displays an initial strength called green strength, and the subsequent evolution over time of the concrete's yield stress at rest is referred to as structuration (Reiter, Wangler, Roussel, & Flatt, 2018; Wangler et al., 2019). The concrete is placed layer by layer until the final height called the build height, depicted as H in Fig. 3, is achieved. The velocity, V, at which the nozzle moves is the print speed, and the total length of one full layer pass in the printing process is called the contour length, L. The deposition of layers is the third stage in concrete printing, referred to as the build stage. This stage is where the concrete makes its transition from fresh concrete to set concrete, building up its strength over time.

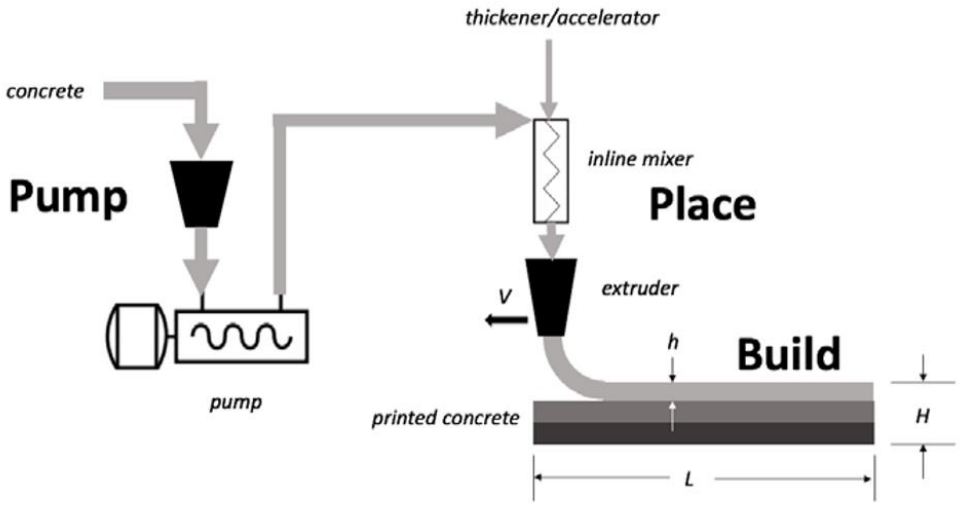

Figure 3: Schematic of concrete 3D printing by extrusion taken from Wangler's publication "Digital concrete processing: A review" (Wangler, Nov 11, 2018).

The required material properties of a printable concrete can be divided into three main categories (pumpability, extrudability, and buildability) according to each of the three stages (Wangler et al., 2019; Wangler, Nov 11, 2018). Each of the three stages of concrete printing require the concrete to meet specific rheological requirements at precise times. In fact, the very concept of 3D printing requires somewhat contradicting rheological properties of the extruded material. The fresh concrete needs to be liquid enough to flow through a delivery system and then, immediately after being extruded, have sufficient green strength to hold its own weight without significant deformation.

Before discussing the specific rheological requirements for each stage of printing, there are a few technical concepts and terms which need to be explained. Firstly, concrete, in its fresh state, is a visco-plastic Bingham fluid which means that it behaves as a pseudo-elastic solid until it is subjected to a high enough shear stress at which point it begins to flow (Roussel, 2018). Its behavior can be accurately predicted through the Bingham parameters, yield stress and plastic viscosity, shown in Eq. 1 (Roussel, 2018; Wallevik, 2006).

Eq. 1) $$\tau = \mu\gamma + \tau_o$$

$\tau = \ shear\ stress\ [Pa]$
$\mu = \ plastic\ viscosity\ [Pa \cdot s]$
$\gamma = shear\ rate\ [s^{-1}]$
$\tau_o = yield\ stress\ [Pa]$

Yield stress is the critical stress above which concrete will begin to flow (Roussel, 2018). Once concrete begins to flow, its resistance to flow is described by the material's plastic viscosity (Marchon, Kawashima, Bessaies-Bey, Mantellato, & Ng, 2018). These two fundamental parameters dictate the rheological behavior of fresh concrete and will be used to discuss the specific requirements for pumpability, extrudability, and buildability. Additionally, the term thixotropy will be used to discuss the rheology of fresh concrete and can be defined as the decrease in plastic viscosity of fresh concrete under shear and subsequent recovery at rest (Marchon et al., 2018).

2.1.1. Pumpability

The first stage of concrete 3D printing is the delivery of the fresh concrete to the nozzle, typically done through a pumping system. At this stage, it is advantageous for the fresh concrete to have as low a plastic viscosity as possible to allow for ease of pumping while still having sufficient yield stress to meet the stability requirements of the extrusion stage (Wangler, Nov 11, 2018). If the plastic viscosity and yield stress are too high, the pressure in the delivery system can become large and impede pumping or damage the system. A mixture with low plastic viscosity and high resting yield stress is achievable by designing a mixture which exhibits shear-thinning (Wangler, Nov 11, 2018). Shear-thinning is a thixotropic process through which the plastic viscosity of a material decreases with increasing shear rate (Marchon et al., 2018). This phenomenon can be achieved in concrete through the addition of thixotropic agents such as

nano-clays which will be discussed in section 2.4.2.2. Quantitatively defining pumpability by the Bingham parameters is easily accomplished in research settings using an apparatus called a coaxial cylinder viscometer and the corresponding equations below (Wallevik, 2006).

Eq. 2) $$\mu = \frac{H(1/R_i^2 - 1/R_O^2)}{8\pi^2 h}$$

Eq. 3) $$\tau_o = \frac{G(1/R_i^2 - 1/R_O^2)}{4\pi h \cdot ln(R_O/R_i)}$$

$R_i = \ inner\ cylinder\ radius\ [m]$
$R_o = \ outer\ cylinder\ radius\ [m]$
$h = cylinder\ height\ [m]$
$H = slope\ of\ torque\ vs. rotational\ velocity\ curve\ [Nm \cdot s]$
$G = y - intercept\ of\ torque\ vs. rotational\ velocity\ curve\ [Nm]$

However, viscometers are cumbersome and difficult to use, making them an inefficient means of assessing pumpability in the field. In construction, it is much more common to determine the pumpability or workability of a mixture using the standard slump test (Marchon et al., 2018). Research by Wallevik at the Norwegian University of Science and Technology (Wallevik, 2006) indicated a relationship between slump and yield stress (Eq. 4), but further work is needed to provide a standard field test method for accurately predicting the plastic viscosity.

Eq. 4) $$S = 300 - 0.416\frac{(\tau_o + 394)}{\rho_{sg}}$$

$S = \ slump\ [mm]$
$\rho_{sg} = \ specific\ gravity\ of\ concrete$

2.1.2. Extrudability

Once the concrete reaches the nozzle, it is extruded layer by layer to create the desired structure. Extrudability refers to the ability of the fresh concrete and nozzle to create a well-controlled filament (Wangler et al., 2019). At this stage, the concrete filament needs to have sufficient green strength to maintain its form under the stress of its own weight. The required yield stress is estimated to be about 150 Pa (0.022 psi) for a typical filament height of 1 cm (0.39 in) (Reiter et al., 2018). The initial yield stress required for a layer to support its own weight is given by Eq. 5 (Wangler et al., 2016).

Eq. 5) $$\tau_o = \rho g h/\sqrt{3}$$

$\rho = \ concrete\ density\ [kg/m^3]$
$g = gravity\ constant\ [m/s^2]$
$h = \ layer\ height\ [m]$

The early structuration of fresh concrete is primarily dependent on its thixotropic behavior, building up green strength by two mechanisms: flocculation and precipitation of early hydrates (Reiter et al., 2018; Roussel, 2018). In the first mechanism, flocculation, colloidal attractive forces between cement particles cause them to clump together forming a network capable of resisting stress with an initial elastic modulus and an initial yield stress (Roussel, 2018). The second mechanism by which concrete's thixotropy increases is through early hydration (Marchon et al., 2018). C-S-H precipitates, which are the main binding phase in concrete (see section 2.3.1.1 for details on cement hydration), develop on the contact points between flocculated cement grains forming bridges between them, further increasing the yield stress (Marchon et al., 2018; Reiter et al., 2018; Roussel, 2018). Flocculation and early hydration contribute to the green strength of freshly extruded concrete and the performance of the layer filament in terms of extrudability. However, as the printing process continues, each fresh concrete filament needs to gain strength more rapidly because it becomes a building element for the following layers.

2.1.3. Buildability

The buildability of concrete can be described as its ability to retain its shape as subsequent layers are added (Wangler, Nov 11, 2018). As layers are deposited, the stresses in the bottom layers due to the weight of those above increase as the structure increases in height. One study. (Wangler et al., 2019) estimated that the yield stress in the bottom layer would need to be approximately 30 kPa (4.35 psi) to support the weight of a typical wall height of 2.5 m (8.2 ft). The required yield stress for the bottom layer at the end of printing can be calculated with Eq. 6 (Wangler et al., 2016).

Eq. 6) $$\tau_o = \rho g H_m/\sqrt{3}$$

$\rho = \ concrete\ density\ [kg/m^3]$
$g = gravity\ constant\ [m/s^2]$
$H_m = \ final\ height\ [m]$

As discussed earlier with extrudability, flocculation and early hydration are responsible for the initial structuration of concrete. However, flocculation only continues until cement particles settle in to their final network structure at which point the increase in yield stress levels off until the accelerated phase of cement hydration begins (Reiter et al., 2018); Roussel, 2018; Wangler et al., 2019). Figure four shows how the evolution of fresh concrete's yield stress changes over time. The timing of the onset of accelerated structuration is one of the major difficulties with concrete 3D printing, and it controls a key parameter in the printing process: print

speed. There is a precise window of time referred to as the operation window or open time within which successful deposition of a layer is possible (Buswell, Leal, Jones, & Dirrenberger, 2018; Wangler et al., 2016). The print speed cannot be too fast as the previous layers need to have a sufficient green strength prior to the deposition of another layer (Le et al., 2012). The upper bound on print speed displayed in Eq. 8 depends on the rate of structuration (Eq.7) (Wangler et al., 2016).

Eq. 7) $$A_{thix} = \rho g H_m / \sqrt{3}\, t_{Hm,min} = \rho g h / \sqrt{3}\, t_{h,min}$$

$A_{thix} = \ structuration\ rate\ [Pa/s]$
$t_{Hm,min} = minimum\ time\ to\ reach\ final\ height\ [s]$
$t_{h,min} = minimum\ time\ before\ layer\ deposition\ [s]$

Eq. 8) $$V < \sqrt{3} L A_{thix} / (\rho g h)$$

$V = \ print\ speed\ [m/s]$
$L = contour\ length\ [m]$

However, there is also a lower bound on print speed. If the material cures too quickly, weak interfaces between layers called cold joints can develop (Wangler et al., 2019). The maximum time between deposition of layers and the corresponding lower bound for print speed can be estimated with Eq. 9 & 10 (Wangler et al., 2016).

Eq. 9) $$t_{h,max} = \frac{\sqrt{\frac{(\rho g h)^2}{12} + (\frac{2\mu V}{h})^2}}{A_{thix}}$$

$t_{h,max} = maximum\ time\ between\ layer\ deposition\ [s]$

Eq. 10) $$V > \frac{\rho g h^2}{4\mu}$$

Cold joints are a consequence of a lack of bonding between successive layers. This occurs when the previous layer is too stiff or has insufficient surface moisture to bond across the layer interface (Le et al., 2012; Wangler et al., 2019). A precise balance between print speed and structuration rate needs to be achieved in order to ensure that layer deposition occurs within the operation window, avoiding both collapse of the structure and the formation of cold joints. The topic of interfacial bonding is of particular interest to researchers and is an area which will be addressed in more detail in section 2.5.2.

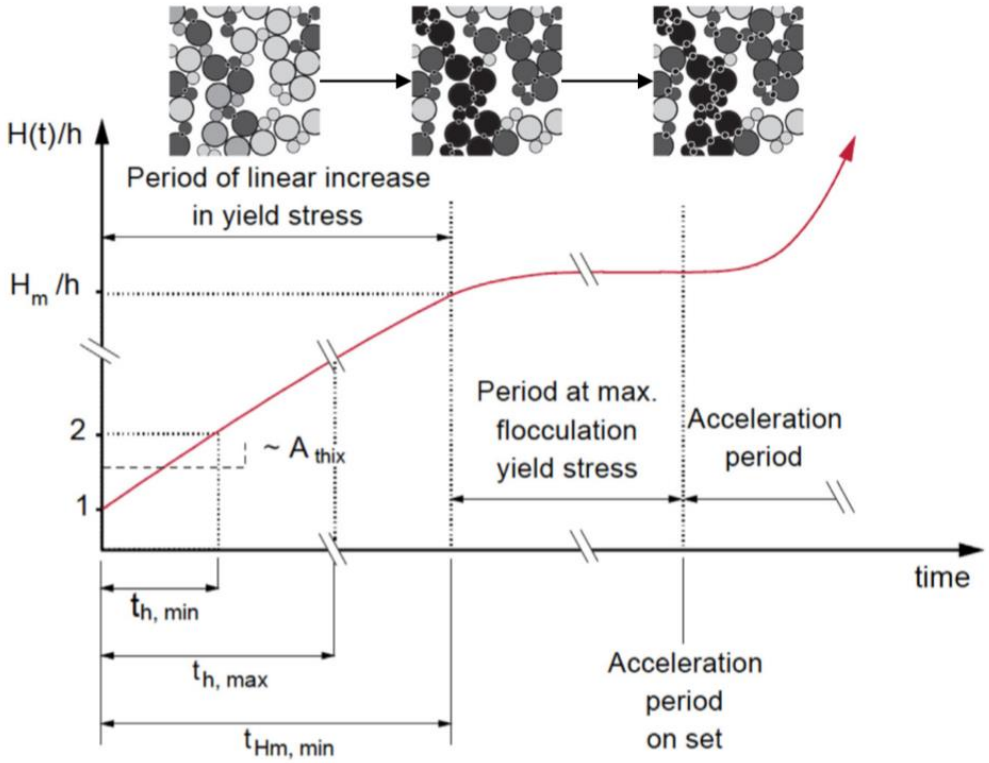

Figure 4: Plot of total building height relative to layer height by time taken from "The role of early age structural build-up in digital fabrication with concrete" (Reiter et al., 2018). The yield stress linearly increases until the maximum yield stress due to flocculation is reached. Then, growth in yield stress accelerates due to hydration.

Although the complexity of the rheological requirements of the concrete printing process are only outlined by this discussion, it is clear that there are many obstacles to overcome. Despite this, many companies and institutions have been able to develop functional 3D printing techniques as discussed in the following section.

2.2. Concrete 3D printing in practice

Concrete 3D printing is an emerging innovative practice that is revolutionizing the construction process due to its sustainability and scalability. It is increasing productivity by shifting the industry towards fully digitized construction processes, combining computer-aided design (CAD) and BIM. This decreases construction time, labor, and assembly errors, while improving the overall quality in the manufacturing process (Buswell et al., 2018). The scalability of concrete printing is also on the rise. Many companies emerging in the industry are now able to print entire buildings as opposed to individual structural members and have already put this technology to use on construction scale projects.

2.2.1. Industry leaders

There are a variety of concrete printing companies that are part of this emerging market including Contour Crafting (El Segundo, California), Total Kustom (Excelsior, Minnesota), COBOD (Copenhagen, Denmark), and XTreeE (Rungis, France). All of these companies are unique, each targeting different areas of construction. Contour Crafting, the first pioneer of concrete extrusion technology, is working towards printing homes, emergency shelters, and large multi-unit structures for low-income populations (Contour Crafting Corporation, 2017). The company is even looking at integrating other building components such as insulation and wiring into the printing process. Contour Crafting also uses a unique nozzle design with side trowels to provide a smooth layer finish (Khoshnevis, 2004). A sample print by Contour Crafting is shown below in Fig. 5.

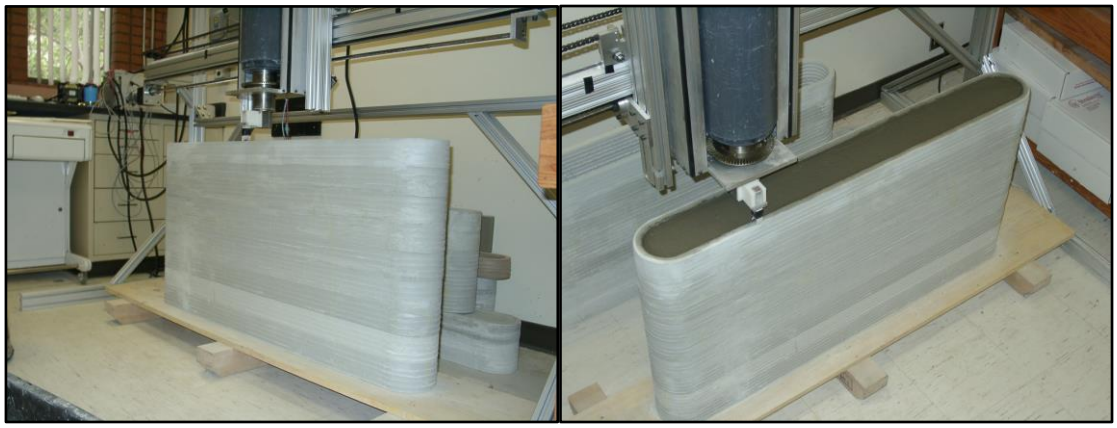

Figure 5: Contour Crafting gantry style machines printing a wall (Contour Crafting Corporation, 2017).

Total Kustom is another leader in the industry with the ability to print functional buildings using a large-scale gantry printer. For example, this company partnered with the Lewis Grand Hotel to print a hotel suite that measured 10.5 m (34.4 ft) by 12.5 m (41.0 ft) with a height of four meters (13.1 ft). The print, including installation of plumbing and electricity, took about a week to complete and consisted of two bedrooms, a living room, and a jacuzzi room (Fig. 6) (Total Kustom, n.d.).

Figure 6: The intricate layout of the 3D printed hotel by Total Kustom (Total Kustom, n.d.).

COBOD makes use of an innovative gantry style concrete printer known as the Building on Demand II (BOD2) which has a modular setup. A modular system is capable of being subdivided into independent components that can be added or subtracted from one another. The modular design of the BOD2 allows the printer to be adjusted to fit an array of project size requirements. This modular design also makes it possible to easily transport the printer to different job sites (COBOD International, 2019). Figures seven and eight shows a 50 m^2 (538 ft^2) building printed by COBOD in Nordhavn, Copenhagen.

Figure 7: This image is an up-close picture of the COBOD nozzle extruding cement.

Figure 8: This image shows the finished product in Copenhagen (COBOD International, 2019).

Unlike the other companies previously stated, XTreeE uses a robotic arm to create complex concrete structures that would be nearly impossible to create without additive manufacturing (XTreeE, n.d.). For example, XTreeE printed a concrete artificial coral reef that is now being used to restore the lost ecological habitat in Calanques National Park, France. The intricate design of the coral reef shown in Fig. 9 and Fig. 10, illustrates the potential with concrete 3D printing to create complex structures that could not be produced with traditional formwork.

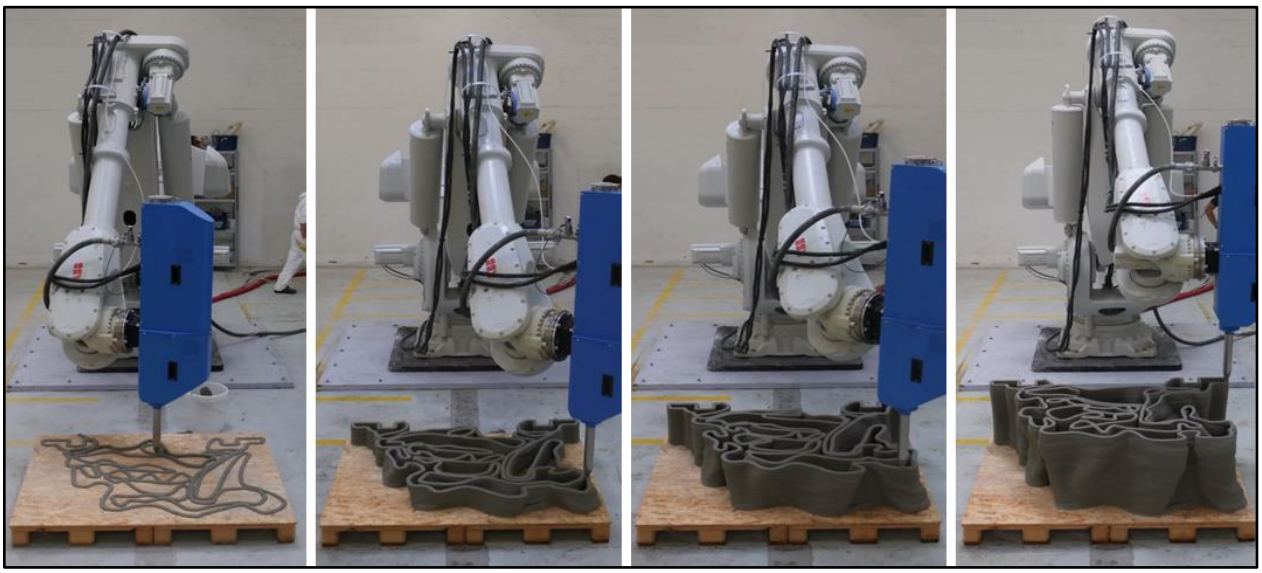

Figure 9: The robotic arm from XTreeE printing an artificial coral reef. The intricate reef displays the freedom of design with additive manufacturing (XTreeE, n.d).

Figure 10: The artificial coral reef printed by XtreeE submerged in the ocean near Calanques National Park, France (XTreeE, n.d.).

2.3. Cementitious materials

2.3.1. Ordinary Portland cement

2.3.1.1. Hydration of Portland cement

To understand how concrete is to be additively manufactured, it is crucial to understand the fundamental component of almost all cement mixes, ordinary Portland cement (OPC). The chemical makeup of OPC consists of five major compounds: tricalcium silicate, dicalcium silicate, tricalcium aluminate, tetracalcium aluminoferrite, and gypsum (calcium sulfate). The two silicates help the concrete harden when mixed with water through a chemical reaction known as hydration (University of Illinois, n.d.). The equation for the hydration of the most reactive silicate, tricalcium silicate, is as follows (University of Illinois, n.d.):

$$2\,Ca_3SiO_5 + 7H_2O \rightarrow 3\,CaO * 2SiO_2 * 4H_2O + 3\,Ca(OH)_2 + 173.6kJ$$

The two products of this hydration reaction are calcium silicate hydrate and calcium hydroxide (University of Illinois, n.d.). The formation of calcium and hydroxide ions continues until the cement is saturated, at which point the ions begin to crystalize into calcium hydroxide and calcium silicate hydrate crystals begin to precipitate. The early formation of these two crystals provides seeds which become sites for further formation of calcium silicate hydrate (C-S-H). C-S-H creates bridging connections between cement particles and holds the system together. C-S-H precipitation contributes to concrete's initial thixotropy, and eventually its strength and stiffness once mass precipitation of this chemical occurs throughout the concrete during the accelerated phase of hydration. Dicalcium silicate's hydration also affects the strength of concrete (University of Illinois, n.d.). This reaction is similar to that of tricalcium silicate except that it is slower and releases less heat. The equation for the hydration of dicalcium silicate is as follows (University of Illinois, n.d.):

$$2\,Ca_2SiO_4 + 5\,H_2O \rightarrow 3\,CaO * 2SiO_2 * 4H_2O + Ca(OH)_2 + 58.6\,kJ$$

Gypsum is added to OPC to control the setting rate and prevent premature and rapid precipitation of C-S-H by the reaction of tricalcium aluminate (Taylor, 1990). Ionic pairs produced by the calcium sulfate latch onto the tricalcium aluminate particles and slow the reaction to avoid flash setting, thus extending the workable period of the concrete mix. The reaction of gypsum with calcium aluminate forms a byproduct called ettringite (Marchon et al., 2018). Ettringite, a long needle-like crystal, also helps control the stiffening of fresh concrete by filling cracks and voids (Portland Cement Association, 2010). The hydration process of OPC is crucial to understanding the behavior of concrete and will play a major role in the development of a printable concrete mixture.

2.3.1.2. Portland cement's environmental impact

Because cement is a key component of the concrete used in construction every day, OPC is produced on a massive scale. In the industrial production of OPC, CO_2 is emitted not only by the chemical reaction that produces the cement, but also by the massive amount of energy used in cement production (S. Kabir, 2012). About one ton of CO_2 is released into the environment for every ton of OPC that is produced (Pailyn, Watcharapong, & Arnon, 2014). Take this one to one ratio and apply it to the more than 120 countries that produce OPC on an industrial level every day, and it is apparent that the production of OPC has an enormous environmental impact. On top of this, there are finite natural materials that can be used to create Portland cement (Rodríguez et al., 2012). Industry leaders, with the environment and economy in mind, have found ways to reduce CO_2 emissions and save production costs by partially replacing Portland cement with supplementary cementitious materials. Some materials including silica fume, fly ash, and slag, all byproducts of manufacturing which normally would go to waste, are now recycled as a binding supplement for cement mixes. These supplementary cementitious materials have properties which affect the pumpability, extrudability, and buildability of printable concrete.

2.3.2. Supplementary cementitious materials

2.3.2.1. Silica fume

One common mineral used as a supplementary cementitious material (SCM) is a byproduct of silicon production, silica fume. Silica fume is a nanocrystalline dust that, when used as a SCM in concrete mixes, increases mechanical strength and improves durability by reducing the size of pores in the cured concrete (Rodríguez et al., 2012). The reaction of silica fume with cement produces longer C-S-H chains than those created by OPC alone, making a stronger bond (Rodríguez et al., 2012). One downside to using silica fume as a replacement for OPC is that a high content in a mixture can be detrimental to pumpability, as these particles easily clump together in mixes. These clumps make the dispersion of cement particles uneven within the mix causing segregation and affecting concrete's cured performance (Rodríguez et al., 2012). Segregation can reduce the pumpability of the concrete, as these flocculated clumps increase plastic viscosity and can become obstructions in the delivery system, impeding extrusion. Overall, silica fume's ability to heighten strength and increase durability suggests that it is beneficial for use as an SCM in the additive manufacturing of concrete.

2.3.2.2. Fly ash

Another material used to replace Portland cement is fly ash, one of the main byproducts of energy production from coal power plants. This material is used as a replacement for Portland cement because it is more environmentally friendly to use recycled fly ash, which has already been created, than to produce more OPC and release unnecessary CO_2 into the environment. ASTM C618 defines two types of fly ash, Class F and Class C (Pailyn et al., 2014). These two classes have different properties depending on the type of coal that was burned. Class F, coming from a bituminous coal has strictly pozzolanic properties as it is primarily composed of alumino-silicate glasses and has a low calcium content. Class C fly ash, coming from sub-bituminous coal, has both pozzolanic and cementitious properties, as it has a high calcium content. Class C is more like a cement on its own while Class F needs a source of calcium to cause hydration reactions resulting in C-S-H (Thomas & Birchall, 1983). Research has provided a way to replace up to 30% by weight of Portland cement with fly ash without having a negative effect on strength or durability (Pailyn et al., 2014). Using any higher fly ash content will lead to longer set times, resulting in a lower green strength of the fresh concrete, which is not optimal for additive manufacturing (Thomas & Birchall, 1983). If the fly ash content is limited, it is an adequate SCM. However, the longevity of this product is questionable because the use of coal is trending towards termination. Therefore, fly ash should not be used as an SCM for the future of 3D printing.

2.3.2.3. Slag

In the process of forging steel, a by-product called slag is produced, which has cementitious properties. Steel production is a huge industry worldwide, resulting in an excess of slag produced. Approximately 400 million tons of slag are produced annually in the process of steel and iron manufacturing (Carvalho, Vernilli, Almeida, Demarco, & Silva, 2017). Specifically, about 100-200 kg (220-441 lbs) of slag is produced per ton of steel manufactured, depending on its grade (Belhadj, Diliberto, & Lecomte, 2012). There are multiple types of slag: blast furnace slag and basic oxygen furnace slag. Blast furnace slag comes from the production of pig-iron from iron ore in a blast furnace. It has cementitious properties as well as a high silica content, making it a great replacement for OPC as silica is one of the main components in C-S-H. Basic oxygen furnace slag is another by-product of steel production that is not used as often in cement production due to a lower silica content. However, it does have a chemical composition that resembles OPC, so it is considered to be a binder. A high content of CaO in basic oxygen furnace slag can lead to volumetric expansion causing instability of the cured concrete, so it is recycled more often in the form of granular borrow for railways (Carvalho et al., 2017). Blast furnace slag is a proper SCM for 3D printing of concrete, and unlike fly ash, the production of steel will continue for the foreseeable future, ensuring long-term availability of slag for use as a SCM.

2.4. Admixtures and additives: their applicability to concrete 3D printing

Because of the contradicting rheological requirements for concrete printing, there needs to be an intricate mix design including precise portions of admixtures to achieve a printable

concrete. Defined in ASTM C125, an admixture is any material added to a cement mix before or during the mixing process, excluding water, cement, aggregate, and fibers. Admixtures have a wide variety of uses and functions such as reducing water, lowering slump, slowing or accelerating set time, and improving workability, durability, and strength. It takes a specific combination of admixtures such as accelerators, retarders, and water-reducers to create a mix suitable for the additive manufacturing of concrete.

2.4.1. Superplasticizers

In the first stage of concrete 3D printing, the fresh concrete mixture needs to have a low enough plastic viscosity in order to achieve the pumpability required for material delivery. One way of lowering the plastic viscosity of fresh concrete is through the use of superplasticizers. Superplasticizers are a dispersant that have been used in concrete since the 1930's to reduce the yield stress and, consequently, the required water content of the mix. Superplasticizers help produce a more durable concrete, as a lower water content leads to fewer air voids within the cured concrete. Since their discovery, superplasticizers have been studied and improved, providing more workable concrete mixes with even less water (Flatt & Schober, 2012).

For the purpose of additive manufacturing with concrete, altering the concrete mix so it is less viscous and behaves more like a liquid without additional water is crucial. This reduces the pressure required to pump a mix through the delivery system. The lower water content will also help it retain its shape once extruded from the nozzle. Moreover, a lower water content in the mix directly correlates to a higher compressive strength of the cured concrete (Chan, Young-Rojanschi, & Li, 2018).

Superplasticizers, also known as high-range water-reducers, are chemicals that have the capability to reduce the required amount of water in a concrete mix by up to 30% (Ramachandran, n.d.). A superplasticizer disperses the cement particles, restricting flocculation when water is added to the mix and increasing the flowability of the concrete mix. This is especially key for printable concretes which typically incorporate only fine aggregates because a greater packing density is achieved, notably increasing the plastic viscosity and lowering pumpability (Marchon et al., 2018). There are multiple classes of superplasticizers which have been developed. In the initial developments of superplasticizers, a by-product of wood pulp was used called lignosulfonate. However, this natural polymer often resulted in extended set times. In the 1960's and 70's, high-range water-reducers started being used such as polyamine sulfonates and polynaphthalene sulfonates, due to their more powerful dispersion forces. Currently, the state-of-the-art superplasticizer is polycarboxylate ether, which has been used to greatly reduce the water to binder ratio. This comb-shaped polymer has advanced concrete construction by giving life to the concept of self-consolidating concrete, which has made pouring concrete more cost efficient and less labor intensive (Flatt & Schober, 2012). Self-consolidating concrete displays much of the desired initial behavior for printable concrete because it is often pumped in a similar manner, and thus has been used as a reference for 3D printing mix designs (Jiao, El Cheikh, Shi, Lesage, & De Schutter, 2019). Superplasticizers are an important admixture, and a polycarboxylate ether-based superplasticizer is essential for achieving a pumpable concrete mix (Marchon et al., 2018).

2.4.2. Thixotropy

2.4.2.1. Fiber reinforcement

One challenge facing concrete 3D printing is the inclusion of tensile reinforcement. Concrete, being weak in tension, requires a reinforcing material to carry tensile loads. Traditionally, this is achieved through the use of mild-carbon reinforcement (rebar) for concrete structures that are poured in traditional formwork. However, including rebar in the layered structure is a challenge with 3D printed concrete. This leads to the investigation of fibers as an alternative type of reinforcement. Additionally, fibers have an effect on the rheology of fresh concrete. Fiber reinforcements increase the viscosity of fresh concrete but improve the stability of the extruded filament. This is crucial for the deposition stage as it allows for retainage of the shape under the weight of the deposited material (Marchon et al., 2018). In all cases, the inclusion of fiber reinforcements showed higher compressive strength, splitting tensile strength, and flexural strength when compared to non-reinforced concrete (Song & Hwang, 2004; Song, Hwang, & Sheu, 2005). Fibers also increase the initial yield stress of fresh concrete which is advantageous for 3D printing as the printed layers need to have enough green strength to support the subsequent layers without deformation (Marchon et al., 2018). Fiber size is an important consideration for concrete 3D printing as the size of the fibers need to be directly correlated with the size of the nozzle. Fiber size can also have an effect on the cured properties. One study using polyvinyl alcohol fibers (PVA) with 6 mm (0.24 in) and 12 mm (0.47 in) lengths found that the shorter 6 mm (0.24 in) fibers led to higher compressive strength in concrete (Noushini, Samali, & Vessalas, 2013).

There are many options when looking at fiber reinforcement including polyvinyl alcohol, steel, polypropylene and nylon. A study by Noushini (Noushini et al., 2013) investigated the effects of PVA reinforcement with regards to the dampening of concrete, which is dependent on the interfacial relationships of the microstructure. This is especially important as PVA contains hydroxyl groups that form hydrogen bonds between the molecules to boost the surface bond strength (Noushini et al., 2013). The surface bond strength increase is due to the interlocking of particles across the layer interface increasing the homogeneity of the built structure. In 3D concrete printing, this is valuable as the bonding between layers is a crucial area of research as will be detailed in section 2.5.2. A study by Weng (Weng, Li, Tan, & Qian, 2018) examined the buildability and pumpability of fiber reinforced concrete based on yield stress, plastic viscosity, extrudability, and setting time. PVA fibers used in this study were found to be extremely successful as an additive in printable concrete. The extrudability was excellent, and the rheological performance was deemed acceptable for large-scale printing (Weng et al., 2018). This assertion was based on the fact that the setting time for the mix was 59.2 minutes, and that the static, dynamic, and plastic viscosities were 3289 Pa (0.48 psi), 314.7 Pa (0.046 psi), and 32.5 Pa•s (0.0047 psi•s), respectively. Based on previous research, the setting time for the mix demonstrated its good extrudability, and the stresses and plastic viscosity demonstrated its strong rheological performance. The strong performance of the PVA fiber mix was further illustrated when it was used to construct a large-scale printed structure (Weng et al., 2018). Due to its rheological performance, PVA is useful as a thixotropic agent in printable concrete. A study by Lawler (Lawler, Zampini, & Shah, 2005) looked into the workability and mechanical performance of a PVA fiber reinforced concrete compared to a steel fiber reinforced concrete. PVA fiber reinforced concrete outperformed the steel fiber concrete in flexural strength and

shrinkage cracking (Lawler et al., 2005). This research also showed that the PVA mix had the best workability in its early state, as opposed to the steel fiber mix which had the worst workability (Lawler et al., 2005). For concrete 3D printing, steel fibers are not a viable means of reinforcement due to their poor workability and larger thickness which causes difficulty with extrusion, but PVA fibers are ideal in terms of rheological and cured performance.

Polypropylene and nylon fibers are other fiber reinforcement options. A study by Song (Song et al., 2005) compared these two fibers and tested dispersion, compressive strength, splitting tensile strength, modulus of rupture, impact resistance, and shrinkage cracking control. The fibers worked to mitigate cracks through the brittle concrete which increases the cracking control. In every test, the nylon fiber reinforced concrete outperformed the polypropylene fiber reinforced concrete (Song et al., 2005). A study by Kazemian (Kazemian, Yuan, Cochran, & Khoshnevis, 2017) found that the design mix including polypropylene actually had the lowest shape stability, whereas the inclusion of nano-clays, another thixotropic agent, enhanced the shape stability of the fresh concrete over the other three design mixes (Kazemian et al., 2017). For this project, either PVA or nylon fiber reinforcement will be ideal due to the strong rheological performance of both fibers and the sustainability of these alcohol and rubber-based fibers in contrast to the plastic based fiber, polypropylene (Noushini et al., 2013).

2.4.2.2. Nano-clays

Nano-clays are layered silicates of one nanometer thickness (Barua, Gogoi, Khan, & Karak, 2019) and range from 50 to 150 nm in length (Yu, 2019). Nano-clays are used in concrete as inorganic additions to modify rheology because they exhibit an important thixotropic behavior called shear-thinning. Nano-clays provide rapid fresh-state stiffening which controls the shape stability immediately after extrusion with little effect on the delivery process (Marchon et al., 2018). They are able to affect a high initial yield stress while exhibiting a low plastic viscosity under shear when added to fresh concrete. However, the individual particles within the nano-clays are incredibly small, and they can become contaminated by organic materials or heavy metals, which reduces the rheological benefits (Marchon et al., 2018). There are several families of clay such as attapulgite, bentonite, kaolinite, and sepiolite, but the most commercially accessible clays are montmorillonite clays (Marchon et al., 2018; Tolinski, 2009). Research has shown that the attapulgite and bentonite families have the highest structuration rate which correlates directly to a stiffer fresh-state and higher yield stress of the concrete (Kaci, Chaouche, & Andréani, 2011). This is further corroborated by the Kazemian study which concluded that the nano-clay mix designs with attapulgite had the highest shape stability of all design mixes studied (Kazemian, Yuan, Cochran, & Khoshnevis, 2017). Nano-clays work best when they are equally dispersed throughout the mix (Martins et al., 2018). However, it is difficult to achieve a homogenous distribution as a result of the extreme hydrophilicity that clays exhibit (Martins et al., 2018). In order to combat this, the clays are often surface treated with charged quaternary ammonium compounds and other coupling agents, but still, even treated clays are often found to be unevenly distributed throughout the mix (Tolinski, 2009).

Due to the variability in quality of nano-clays as well as difficulties with achieving a homogenous distribution that demonstrates the optimal rheology, nano-clays will not be used for this project. Instead, PVA fibers will be used to enhance the rheology of fresh concrete and provide reinforcement.

2.4.3. Viscosity modifying admixtures

Frequently used in industrial practice, viscosity modifying admixtures (VMAs), increase yield strength evolution and control water transport and the porous structure in fresh and cured concrete (Marchon et al., 2018). VMAs also control the risk of segregation for highly flowable mix designs, improve water retention, and promote particle flocculation. Flocculation is an important mechanism involved in early structuration and contributes to the extrudability of printed concrete. VMAs increase the effective solid content and the amount of contacts between the cement particles which allows for bridges to form between cement grains (Reiter et al., 2018). It is important to note that a VMA's efficiency as a flocculant depends on the molecular weight and their attraction to the cement paste (Marchon et al., 2018). The thixotropic build up due to flocculation can be reversed by the shear forces during pumping which minimizes issues with starting or stopping the printing process (Reiter et al., 2018).

There have been many studies into VMAs such as welan gum, diutan gum, and polyacrylamides. Welan and diutan gum have very pronounced thixotropy within the first minutes after being extruded, but these admixtures are limited in strength due to the specific range of the colloidal interactions for these admixtures (Reiter et al., 2018). This is a key consideration, as the effectiveness of the particle flocculation is limited for welan and diutan gum compared to other VMA admixtures. Studies looking into the effects of polyacrylamide (PAM) on fresh cement paste have found that this polymer has pronounced effects as a flocculant in fresh concrete. PAM is able to adsorb simultaneously on several cement grains bridging them to increase the yield stress (Bessaies-Bey, Baumann, Schmitz, Radler, & Roussel, 2015). This enhanced thixotropy helps printed layers support more weight during the building phase. Because PAM is able to adsorb on multiple layers, it is also suggested that this admixture is able to improve the bond between layers creating a more cohesive finished product. PAM also delays bleeding and significantly increases fresh concrete cohesion (Bessaies-Bey et al., 2015). Bleeding is important for printed concrete as surface moisture is essential for hydration to occur across the layer interface which improves interlayer bonding. PAM's delayed effect on bleeding may be advantageous for interlayer bonding as hydration does not begin until after particle flocculation at which point excess water would be desirable. The key parameter for VMA adsorption is the particle surface covered by the polymer. Marchon determined that the optimum bridging flocculation between cement grains of subsequent layers is attained when the VMA fibers accounts for half of the area of the layer surface on top of which the next layer will be printed (Marchon et al., 2018). PAM's adsorption is enhanced by its anionicity, whereas welan and diutan gum adsorption decreases with a rising concentration of hydroxyl groups (Bessaies-Bey et al., 2015). This means that the use of PVA fibers, which include hydroxyl groups, may negatively impact the effectiveness of welan and diutan gum, but could enhance the effects of PAM. Due to its compatibility with PVA fibers, superior effect on structuration, and ability to bridge across layers of cement paste, PAM is the most suitable VMA for printable concrete and will be used in this project (Marchon et al., 2018).

2.4.4. Accelerators

Accelerators come into play within the third rheological requirement for 3D printing: buildability. Accelerators affect the structuration rate as their main use is for rapid strength gain

in fresh concrete. Most accelerators are broken into three categories: soluble inorganic salts, shotcrete accelerators, and C-S-H seeds.

Inorganic salts increase the concentration of ions in the fresh concrete which enhances the precipitation of the hydrate phases (Reiter et al., 2018). This is key for the initial structuration of concrete. A few inorganic salts are chlorides, bromides, carbonates, and nitrates. Among the inorganic salts, calcium chloride is the most efficient (Marchon et al., 2018). One study identified that the mechanism of acceleration is not entirely understood for calcium chloride, though it is thought that the calcium ions affect the nucleation and growth of hydrates leading to its effectiveness as an accelerator (Nicoleau, Schreiner, & Nonat, 2014). With that being said, the chloride ions inside of calcium chloride tend to corrode reinforcement, and in many countries, the use of this accelerant is limited or prohibited (Marchon et al., 2018). This will not be a problem for this project as steel will not be included in the printed structure, but in real world applications, steel may be used in which case this accelerator should be avoided, despite it being the most cost-effective option for accelerators (Marchon et al., 2018).

Shotcrete accelerators have proven to be a promising additive for printable concrete. The most commercially used shotcrete accelerators are aluminum salts which fall into two categories: alkali and alkali-free. The main advantage to using alkali-free shotcrete accelerators is that they are non-hazardous (Marchon et al., 2018). Alkali-free accelerators cause quick flocculation of the system due to the precipitation of ettringite (Marchon et al., 2018). In concrete 3D printing, this is advantageous as the layers stiffen quickly and develop sufficient yield stress to support the load of subsequent layers without deformation aiding buildability. Due to the rapid setting time associated with shotcrete accelerators, it is necessary to add them at the nozzle through a process called inline mixing. In this process, the accelerator is mixed with the fresh concrete directly at the nozzle to avoid setting within the delivery system (Marchon et al., 2018). One study looking into 3D printed concrete concluded that due to the addition of shotcrete accelerators, the set time is reduced to milliseconds as compared to hours for traditional cast concrete (Wangler et al., 2019). This is why the addition of shotcrete accelerators must be at the nozzle to avoid clogging in the delivery lines. Despite the potential upside to shotcrete accelerators, there is one major point of concern with their use referred to as flash setting. Flash setting is a rapid development of rigidity of concrete which leads to negative effects on long-term strength development and severely affects the interlayer bonding by causing cold joints, discussed in section 2.5.2 (Reiter et al., 2018).

C-S-H seeds are another option for increasing the structuration rate of the concrete filaments. They strongly increase the surface available for hydrate precipitation leading to an earlier onset and faster acceleration period (Marchon et al., 2018). C-S-H seeds do not have as radical an effect as the previously mentioned accelerators but do show promise. Unlike shotcrete accelerators, which may lead to sulphate depletion and flash set, the reaction of C-S-H seeds with silicate leads to a faster development of long-term strength. The amount of sulphate is directly correlated to the amount of ettringite produced. Ettringite fills up air voids within the concrete to boost the yield stress. The main drawback with regards to C-S-H seeds is the necessity of a high water and superplasticizer content to reduce the yield stress of the mix (Marchon et al., 2018).

Shotcrete accelerators are the best admixture for achieving buildability in printable concrete because this accelerant leads to a very rapid increase in strength. This rapid strength

increase decreases the minimum time between layer deposition and consequently decreases building times. The challenge with shotcrete accelerators is that they cannot be added into the initial mix and therefore require an inline mixing process. One way to work around this challenge is to use retarders in conjunction with accelerators.

2.4.5. Retarders

While accelerators, such as those in shotcrete, are very helpful in concrete printing, they can be detrimental to pumpability if the mix begins to harden before being extruded from the nozzle. To avoid this, chemicals known as retarders can be used, which delay hydration, therefore preserving the pumpability of the mix for a longer period of time. Retarders encase the microstructure of the cement particles, prolonging the time until the hydration process takes place (Belous, Koshevar, & Rodtsevich, 2009). However, once the hydration process begins, the reaction rate is often accelerated by these retardant chemicals, especially when carbohydrates are used as a retarder. Retarders also work better when mid-range water reducers are added to the mix, such as lignosulfonate (Marchon et al., 2018; Young, 1972). Sugars, such as glucose, sucrose, maltose, etc. are also often used as retarders because of their reaction with the cement. Sugars combine with calcium oxide, aluminum oxide, and iron oxides to create a metal-organic coating which covers the cement particles keeping hydration from taking place (Thomas & Birchall, 1983). In general, the way these retarding agents react is complex depending on the types of admixtures in the mix, the water content, and at what point the retarder is added. These are important factors to monitor, especially the admixtures in the mix, because retarding chemicals have the possibility to reduce compressive strength or even enhance the effects of superplasticizers (Belous et al., 2009). In additive manufacturing, the hydration process must be delayed while the concrete is being delivered from the pump to the nozzle of the printer, and quickly begin once the concrete is extruded. Because the behavior of retarders is widely variable depending on its interactions with the other admixtures included, it is difficult to predict its actual effect. As a result, it is more feasible to add a shotcrete accelerator at the nozzle using an in-line mixture, rather than use this accelerator in conjunction with a retarder.

2.5. Areas of improvement

2.5.1. Alternative binders

Supplementary cementitious materials such as fly ash are limited especially when looking at the future hopes for digitalization of concrete construction. This is because they can only replace about 10-50% of OPC without lengthening setting times and lowering concrete's green strength (Juenger, Winnefeld, Provis, & Ideker, 2011; Shi, Jiménez, & Palomo, 2011). In addition, OPC itself has a relatively low structuration rate which is an obstacle for the buildability of printed concrete (Marchon et al., 2018). Although accelerators can be used to speed up the structuration rate, another potential solution is the use of alternative binders. Calcium sulfoaluminate (CSA) cement is one alternative binder which could be used to compliment or entirely replace OPC (Marchon et al., 2018; Shi et al., 2011; Winnefeld & Lothenbach, 2010). The hydration of CSA cement results primarily in the formation of ettringite rather than C-S-H as

with OPC (Shi et al., 2011; Winnefeld & Lothenbach, 2010). The hydration phase of ettringite has a long, crystalline structure which takes up more space and causes the cured concrete to have a lower permeability therefore making it more durable (Winnefeld & Lothenbach, 2010). Further, CSA cements are said to reach higher strength both early in hydration and after curing depending on the reactivity of the calcium sulfate used in the binder (Juenger et al., 2011; Shi et al., 2011; Winnefeld & Lothenbach, 2010). This is a large benefit of CSA cements compared to OPC when considering the need for green strength during extrusion and quick structuration during building. Although complete hydration of CSA cement requires a water to cement ratio of around 0.60, ratios of as low as 0.30-0.45 are typically used (Juenger et al., 2011). CSA concrete can set in as quick as five minutes for a water to cement ratio of 0.35 (Shi et al., 2011). CSA also works with most traditional admixtures including retarders, viscosity modifiers, and superplasticizers to the same degree as OPC (Marchon et al., 2018; Shi et al., 2011). Another benefit of CSA cement for concrete 3D printing is the binder's expansive nature which can reduce the amount of cracking due to drying shrinkage, a large problem with 3D printed concrete (De Schutter et al., 2018; Juenger et al., 2011). The environmental issues associated with OPC, namely finite material use and carbon emissions, are another reason why alternate binders should be investigated for use over OPC. CSA clinker can be produced at 1250^{o}C, 200^{o}C less than OPC, and is easier to grind making its production much more sustainable (Juenger et al., 2011; Shi et al., 2011; Winnefeld & Lothenbach, 2010). CSA cement is also not the only alternative which could be used for the purpose of 3D printing. Calcium aluminate cement (CAC) and various alkali-activated binders are other cement types with many of the same potentials as CSA, the latter having the potential to be comprised entirely of waste materials (Juenger et al., 2011). The environmental benefits of concrete 3D printing including material efficiency could only be advanced if alternative, low-CO_2 binders are developed for use with concrete printing. Experimenting with the use of alternative binders is beyond the scope of this research, but investigating the adaptability of alternative binders for concrete printing would be an excellent topic for future research.

2.5.2. Interlayer bonding

One of the limitations of concrete 3D printing which requires further consideration and research is the bond strength between layers of extruded concrete referred to as the interlayer strength. The interface between layers tends to be a major weakness of printed concrete structures due to the lack of adhesion between layers and is an area where flaws often occur creating stress concentrations (Sanjayan, Nematollahi, Xia, & Marchment, 2018). In addition, because homogeneity of printed concrete is not yet achievable due to weak interlayer bonding, the strength of printed concrete is anisotropic, exhibiting different strength behavior depending on the orientation of loading (Buswell et al., 2018; Sanjayan et al., 2018; Wangler et al., 2019). This is an important consideration and a significant limitation on the viability of concrete 3D printing for structural applications. As discussed in the earlier section on buildability, there are a number of variables which affect the interlayer strength of printed concrete: namely, structuration rate and print speed (Buswell et al., 2018; Le et al., 2012; Wangler et al., 2016; Wangler et al., 2019). The time delay between printed layers should be long enough to allow for sufficient green strength to build up in the previous layer, but it must also be short enough to allow for adequate bonding between layers (Sanjayan et al., 2018). Determining the proper

delay time is a balance between print speed and structuration rate. However, this delay time varies depending on the contour length and the environment in which printing is taking place (Roussel, 2018; Wangler et al., 2019).

The issue of interlayer bonding and the reason behind the formation of cold joints is important to understand if greater homogeneity between layers is to be achieved. Research has indicated that evaporation of surface moisture could be one main factor contributing to inadequate bonding (Sanjayan et al., 2018). Traditionally, in concrete construction, formwork encases the concrete and reduces the amount of moisture loss due to drying. However, during the time delay between deposition of layers in 3D printing, the layer surface is exposed to the environment and becomes a site for moisture loss. Other research (Keita, Bessaies-Bey, Zuo, Belin, & Roussel, 2019) determined that the source of the decrease in layer adhesion is superficial extremely localized drying at the layer surface leaving insufficient water at the interface for hydration to take place. Roussel (Roussel, 2018) confirms these results finding that when compared to a reference bond protected from drying, a layer exposed to drying loses approximately 50% of its interlayer bond strength in a matter of about ten minutes. In addition to moisture level, other studies have indicated that a lack of contact area between the two layers could also be a cause of reduced interlayer strength from a lack of mechanical bonding (Nerella, Hempel, & Mechtcherine, 2019).

The weak bond interface between layers is considered to be the “Achilles heel of 3D printing with concrete structures” (Nerella et al., 2019). It is of critical importance to the realization of construction scale 3D printing that a method of enhancing the interlayer bond be discovered. There is already ongoing research into this topic and progress is being made. For example, increasing interlayer bonding through topological interlocking is one such posed solution. Topological interlocking is a design principal considering the ability of elements to resist separation purely by geometrical constraints (Zareiyan & Khoshnevis, 2017). Khoshnevis, the first pioneer into concrete 3D printing by extrusion, using his Contour Crafting technology is creating a type of topological interlocking by troweling the outer surface between layers (Khoshnevis, 2004; Zareiyan & Khoshnevis, 2017). Khoshnevis and Zareiyana found that creating a grooved interlocking between layers increases layer adhesion by expanding the contact area at the interface (Zareiyan & Khoshnevis, 2017). They also predict that this type of interlocking can improve a printed structure’s ability to resist vibration and lateral loads (Zareiyan & Khoshnevis, 2017). Other proposed methods of increasing bond strength include a chemical adhesive spray applied to the top layer before deposition of the following layer of concrete (Verian, Carli, Bright, & Maandi, 2018; Wangler et al., 2019) and a cement paste layer deposited between layers of concrete to improve the effective contact area (Marchment, Sanjayan, & Xia, 2019; Wangler et al., 2019). However, the issue of interlayer bonding remains largely unsolved and further work is required if concrete 3D printing is to be integrated into the construction industry (Wangler et al., 2019). Therefore, this research aims to investigate new methods of enhancing interlayer bonding in order to advance the cured performance of printed concrete structures.

2.5.3. Active rheology control/active stiffening control

As explained throughout the Background, controlling the rheology of fresh concrete is a difficult task. Currently, it is achieved through the use of admixtures, but ensuring that the

desired properties are developed at exactly the right time is extremely difficult. The optimal timeline of rheological development can vary depending on the contour length and size of the printed structure, requiring different mix designs. However, a concept referred to as active rheology control or active stiffening control could enhance rheological control during the extrusion phase with magnetic particles (De Schutter et al., 2018). Magnetorheological fluids are a type of smart material composed of magnetic particles and a carrier fluid (Jiao et al., 2019). When a magnetic field is applied to a magnetorheological fluid, the magnetic particles align with the magnetic field and result in higher elastic behavior of the fluid (Jiao et al., 2019). Fresh concrete, as a Bingham fluid, is a potential material for use as a carrier fluid because it already has an initial yield stress (Jiao et al., 2019). Theoretically, by adding magnetic nano-particles to fresh concrete, the elastic behavior of an extruded filament could be increased. Research considering the effects of ferroferric oxide (Fe_3O_4) nano-particles on concrete found that even without the application of magnetic fields, nano-Fe_3O_4 increases compressive strength with no effect on the consistency of the fresh paste up to approximately 5% by weight of cement (Sikora, Horszczaruk, Cendrowski, & Mijowska, 2016). Another publication indicated that nano-Fe_3O_4 also accelerates hydration and reduces water adsorption and chloride penetration (Jiao et al., 2019). This research investigated the effect of varying magnetic field strengths on cementitious paste. It was determined that the higher magnetic field strength resulted in a higher elastic or solid-like behavior of the paste (Jiao et al., 2019). Although, the study also found that immediately after an increase in the magnetic field strength, the nano-Fe_3O_4 particles reorganized into the chain-like structure aligned with magnetic fields. During reorganization, flocculated networks were broken resulting in a sharp decrease in elastic behavior for a brief period of time (Jiao et al., 2019). However, once magnetic fields were completely removed residual chain-like structures remained intact and increased the structuration rate of the cementitious paste (Jiao et al., 2019). Other research also reported an increase in shear strength of cement paste with applied magnetic fields (De Schutter et al., 2018). Although the research into active rheology control of printable concretes is limited, this method shows promise in enhancing control over green strength and structuration during printing. The research completed in this work does not focus on active rheology control of printed concrete, but it is discussed here because it is another critical development which should be considered in future research on concrete 3D printing.

2.6. Testing methods literature review

2.6.1. Brazilian disk test

The Brazilian disk test is a variation of a tensile test commonly used to investigate the mixed-mode fracture toughness of bi-materials (Huang, Liu, & Stout, 1996). The specimens for this test are cylindrical in shape and are subjected to a pair of concentrated forces at the perimeter. The type of fracture that the sample undergoes is controlled by adjusting the loading angle, θ, depicted in Fig.11. Fracture type varies from Mode I, crack opening fracture, to Mode II, in-plane shear fracture, with any range of mode mixities between the two modes (Melo, Rahbar, & Soboyejo, 2011). The fracture toughness can be determined with Eq. 11 (Rahbar, Nima, Yang, & Soboyejo, 2008). In a study by Huang, it was found that pure Mode I fracture can be determined from a loading angle of zero degrees, while pure Mode II fracture can be

determined from a loading angle of around 23 degrees, measured from the crack interface to the loading axis (Huang et al., 1996). This is further corroborated in a study by Rahbar, where Mode II fracture is found to occur at 25 degrees (Rahbar et al., 2008). Typically, a notch is created in the middle of the specimen to promote crack propagation along the interface between materials (Huang et al., 1996). In Mode I fracture, the largest stress concentrations happen at and around the contact points between the load cell and the specimen (Markides, Pasiou, & Kourkoulis, 2015). This compressive stress is transferred through the center of the specimen directly along the load axis resulting in tensile forces at the interface. Fig.12 illustrates the stress development during Mode I fracture. In Mode II fracture, compressive forces are distributed to either side of the angled interface resulting in the development of shear at the interface between materials (Markides et al., 2015). Fig. 13 illustrates this type of stress development resulting in shear forces during a Brazilian disk test for a mixed-modal fracture subject to a combination of shear and tensile stresses.

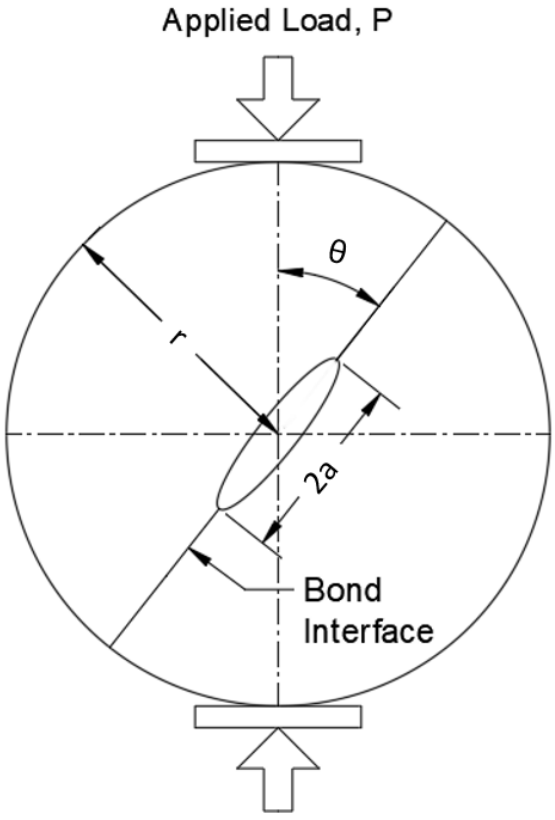

Figure 11: Schematic of the Brazilian disk test showing a typical Brazilian disk specimen. The load angle, θ, controls the type of fracture with Mode I, tensile fracture, at zero degrees and Mode II, in-plane shear fracture at 25 degrees. Specimens generally have a notch with length 2a as shown, but for the purposes of this research no notch was created at the interface.

Eq. 11) $$G_c = \frac{1}{\underline{E}}(K_I^2 + K_{II}^2)(\frac{P^2 l}{\pi a^2 t^2})$$

$G_c = fracture\ toughness\ [J/m^2]$
$\underline{E} = plane\ strain\ Young's\ modulus\ [Pa]$
$K_{I/II} = stress\ intensity\ factors, K_{I/II} = f_{I/II} P\sqrt{a},$
$where\ f_{I/II}\ are\ non-dimensional\ calibration\ factors$
$P = max\ load\ [N]$
$l = half\ crack\ length\ [m]$
$a = disk\ radius\ [m]$
$t = disk\ thickness\ [m]$

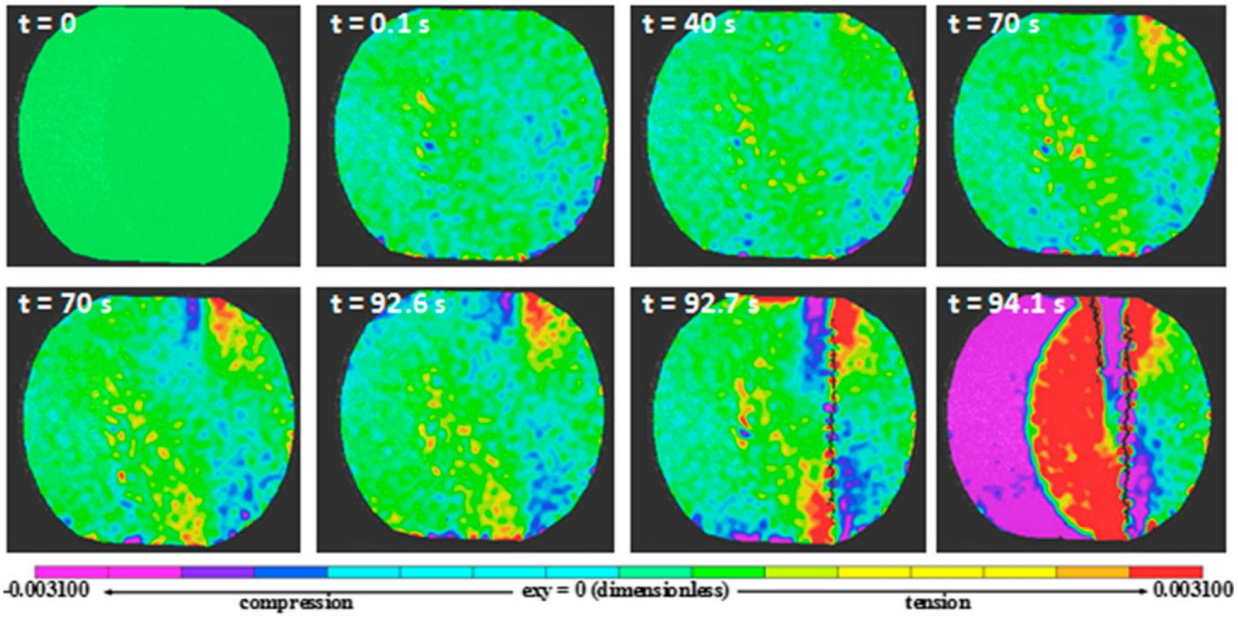

Figure 12: Illustration of stress development during a tensile fracture (Mode I) taken from "Improving measurement accuracy of Brazilian tensile strength of rock by digital image correlation" (He, Chen, Zhang, & Dong, 2018). Tensile stresses shown in red develop along the interface during loading. The sample fractures by opening along the axis of loading.

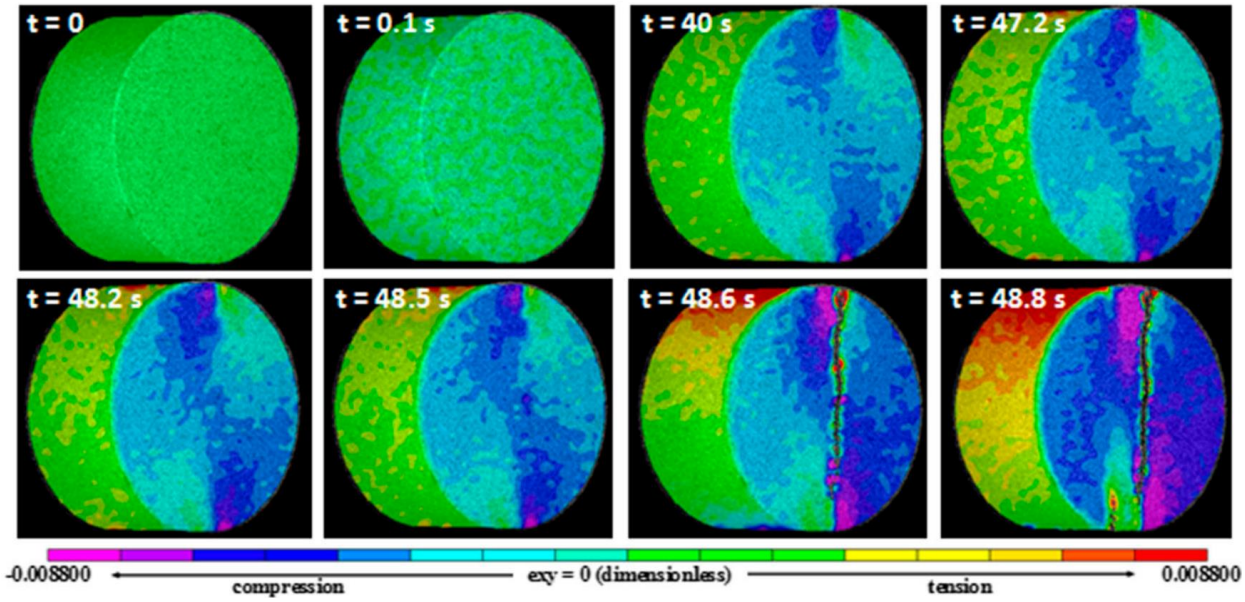

Figure 13: Illustration of stress development during a shear-tensile fracture (mixed-modal) taken from "Improving measurement accuracy of Brazilian tensile strength of rock by digital image correlation" (He et al., 2018). Compression stresses shown in blue develop on opposing sides of the loading axis, resulting in shear stresses which split the sample.

2.6.2. Scanning electron microscopy

Scanning electron microscopy (SEM) is commonly used to produce images of the microstructure of materials (Omidi et al., 2017). Scanning electron microscopes develop an image with a resolution of up to one nanometer by scanning the surface of a material specimen with a beam of electrons (Ebnesajjad, 2006). The specimen is typically encased in a vacuum environment within the SEM, and the surface is coated with a thin layer of conductive material to ensure that it attracts the electrons (Ebnesajjad, 2006). Electrons are emitted by the electron gun located at the top of a column through which the electrons travel. The electron gun is usually a thermal source which emits high energy electrons in the range of 100-30,000 electron volts (Goldstein et al., 2017). The beam of electrons travels through a series of electromagnetic lenses and apertures focusing the beam, and then contacts the surface of the specimen penetrating to a depth of about one micrometer (Ebnesajjad, 2006). This interaction releases photons and electrons from the sample surface which are then detected and used to produce a detailed image (Omidi et al., 2017). There are two main types of electrons used for imaging. A backscattered electron is one that is emitted backwards elastically after the beam interacts with the specimen surface. A secondary electron has a low energy, less than 50 electron volts, and occurs from an inelastic collision with the surface (NANOIMAGES, 2017). Multiple modes of detection exist depending on the type of material under investigation including X-ray mapping, secondary electron imaging, backscattered electron imaging, electron channeling, and Auger electron microscopy (Goldstein et al., 2017). There are three main types of SEM. The first type is a conventional SEM which maintains a high vacuum to allow for electrons to move freely without being deflected or absorbed by air molecules (Goldstein et al., 2017; Omidi et al., 2017). Although, the high vacuum environment is not ideal for concrete as it causes dehydration and

cracking (Goldstein et al., 2017). The second type, environmental SEM, operates at elevated pressures from 0.2 to 20 torr which lessens dehydration and cracking with concrete specimens, but this can cause issues with scattering electrons. Finally, the low vacuum SEM operates at pressures between 0.2 and 2 torr and also reduces the effects of dehydration. The environmental and low vacuum SEM eliminate the need for conductive coatings on the specimen surface and are most suitable for concrete specimens (Goldstein et al., 2017).

3. Methodology

3.1. Materials and mixture proportions

All mixing was done using a Hobart Legacy 120 Mixer, shown in Fig. 14. The mixing procedure was kept consistent for each set of mix designs to ensure that the mixtures were comparable for testing. The mixing procedures for each mix design are detailed in Appendix A. For each mix design containing a new additive, trial mixtures of one liter were qualitatively analyzed to determine preliminary mixture proportions. The trial mixtures were analyzed based on their consistency and workability determined both visually and by touch. Also, using a similar procedure to that of other research on printable concretes (Zhang et al., 2019), a modified slump test was completed on each trial mixture with a 101.6 mm (4 in) diameter by 101.6 mm (4 in) tall PVC cylinder shown in Fig. 15. The cylinder was filled halfway with freshly mixed concrete, rodded 15 times, and then filled to the top and rodded another 15 times. The deformation of the fresh concrete after the cylinder was lifted was recorded and aided in determining the best mixture designs. The specific gravity of all materials and admixtures used are shown in Table 1, and all trial mix designs can be found in Appendices B-E.

Figure 14: Hobart Legacy 120 Mixer used to maintain a consistent mixing speed in each step of the mixing procedure.

Figure 15: 101.6 mm x 101.6 mm Ø cylinder for estimating the pumpability and assessing consistency of trial mixtures.

Table 1: Specific gravities of all materials used to determine mixture proportions on a gram per liter scale.

Material	Cement	Silica Fume	Fine Sand	Superplasticizer	Acti-Gel	PAM	PVA Fiber
Specific Gravity	3.00	2.20	2.58	1.10	1.14	1.30	1.29

In order to have a reference for determining the optimal mixture design for a printable concrete, a base mix design using common concrete materials was created. The base mix design included ASTM C150 type I/II Portland cement, densified silica fume, fine sand, and water. The sand used was an easily accessible fine sand produced by Quikrete with a maximum particle size of 2.36 mm (0.93 in) and a fineness modulus of 1.76. The particle size distribution of the sand is shown in Fig. 16. Seven different trial mixtures were qualitatively analyzed, and the best mixture was used as a reference for the subsequent mix designs. The mixture proportions of the base mixture tested can be found in Table 2.

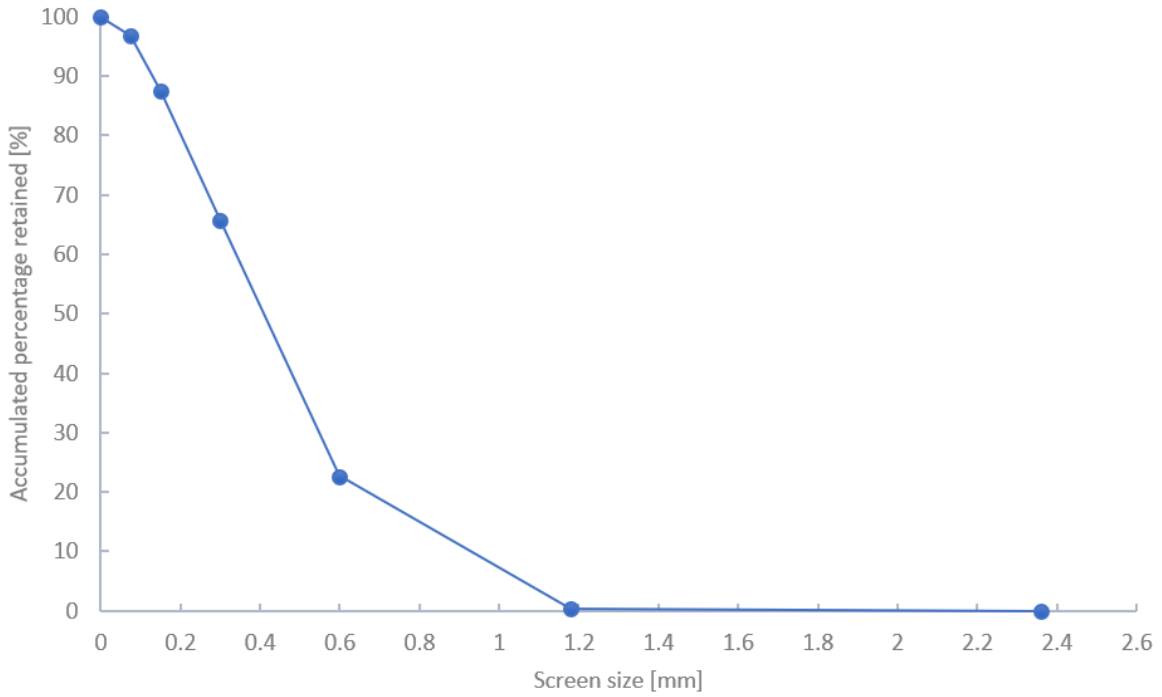

Figure 16: Graph showing the particle size distribution from a sieve analysis done on the fine sand used for all mixtures. This sand had a fineness modulus of 1.76 and a maximum particle size of 2.36 mm.

Table 2: Mix proportions for reference mix design in grams per liter.

Mixture Label	Cement (g/L)	Silica Fume (g/L)	Sand (g/L)	Water (g/L)	W/B
B508SF	457.0	51.0	1366.0	295.0	0.581

Once a reference mix design was determined, mix designs with superplasticizer were investigated. ADVA® Cast 575, a polycarboxylate ether-based superplasticizer, was used for all mixtures. Nine different trial mixtures were created by modifying mixture designs from another source (Zhang et al., 2019), and two were determined to be suitable for further investigation. The mix proportions of the two superplasticizer mixes are shown in Table 3. Superplasticizer was used in all subsequent mix designs because it was determined to be crucial for achieving a pumpable mixture.

Table 3: Mix proportions for mix design with superplasticizer in grams per liter.

Mixture Label	Cement (g/L)	Silica Fume (g/L)	Fine Sand (g/L)	Water (g/L)	W/B	Superplasticizer (g/L)
B719SP1.0	647	72	1317	241	0.335	7.2 (1.0%)
B707SP1.0	636	71	1338	237	0.335	7.1 (1.0%)

Next, mix designs including eight-millimeter PVA fibers were created from the previous superplasticizer mix designs. PVA fiber doses of 0.25% and 0.5% by total volume of concrete were used in the trial mixtures based on other research on PVA fibers (Noushini, Samali, & Vessalas, 2013). The final mix proportions for the mixtures including PVA fibers can be found in Table 4. Fibers were included in all of the subsequent mix designs because they were deemed a critical component for the cohesiveness and cured strength of printable concrete.

Table 4: Mix proportions for mix design with PVA fibers in grams per liter.

Mixture Label	Cement (g/L)	Silica Fume (g/L)	Fine Sand (g/L)	Water (g/L)	W/B	Superplasticizer (g/L)	8 mm PVA Fiber (g/L)
B710SP1.2 PVA0.25	639.0	71.0	1315.0	245.0	0.345	8.5 (1.2%)	3.23 (0.25%)
B690SP1.2 PVA0.25	621.0	69.0	1333.0	245.0	0.355	8.3 (1.2%)	3.23 (0.25%)

Finally, trial mix designs with two different VMAs were completed. The first VMA was PAM, a water-soluble polymer, and the second VMA was liquid Acti-Gel 208, a mixture of attapulgite clay and quartz powder (Active Minerals International, 2017). Approximately 10 gallons of Acti-Gel was supplied for this project by a local contractor, SSG Pools. For the mixtures including PAM, a dose of 9% by weight of binder was initially considered based on the results of another study (Sun & Xu, 2008). However, doses as low as 0.075% were evaluated. The doses for mixtures including Acti-Gel were based off of the recommended dose of 0.2% by weight of dry materials (Active Minerals International, 2017). The most suitable mix proportions for these two VMA mixtures are shown in Table 5.

Table 5: Mix proportions for mix design with VMAs in grams per liter.

Mixture Label	Cement (g/L)	Silica Fume (g/L)	Fine Sand (g/L)	Water (g/L)	W/B	Superplasticizer (g/L)	PVA Fiber (g/L)	PAM (g/L)	Acti-Gel (g/L)
B571.2SP 1.6PAM0.6	514.2	57	1149.6	357	0.625	9.1 (1.6%)	3.23 (0.25%)	3.43 (0.6%)	-
B571.2SP 1.6PAM0.9	514.2	57	1149.6	357	0.625	9.1 (1.6%)	3.23 (0.25%)	5.14 (0.9%)	-
B671SP1. 6AG0.6	604	67	1350	245	0.365	10.7 (1.6%)	3.23 (0.25%)	-	12.13 (0.6%)
B671SP1. 6AG0.8	604	67	1350	245	0.365	10.7 (1.6%)	3.23 (0.25%)	-	16.17 (0.8%)

3.2. Determination of optimal mix design

All mix designs detailed above were evaluated for the three rheological requirements of printable concrete: pumpability, extrudability, and buildability. These tests were performed to determine an optimal mix which could be used for 3D printing. The process for determining the optimal mix design is outlined by the flowchart in Fig. 17.

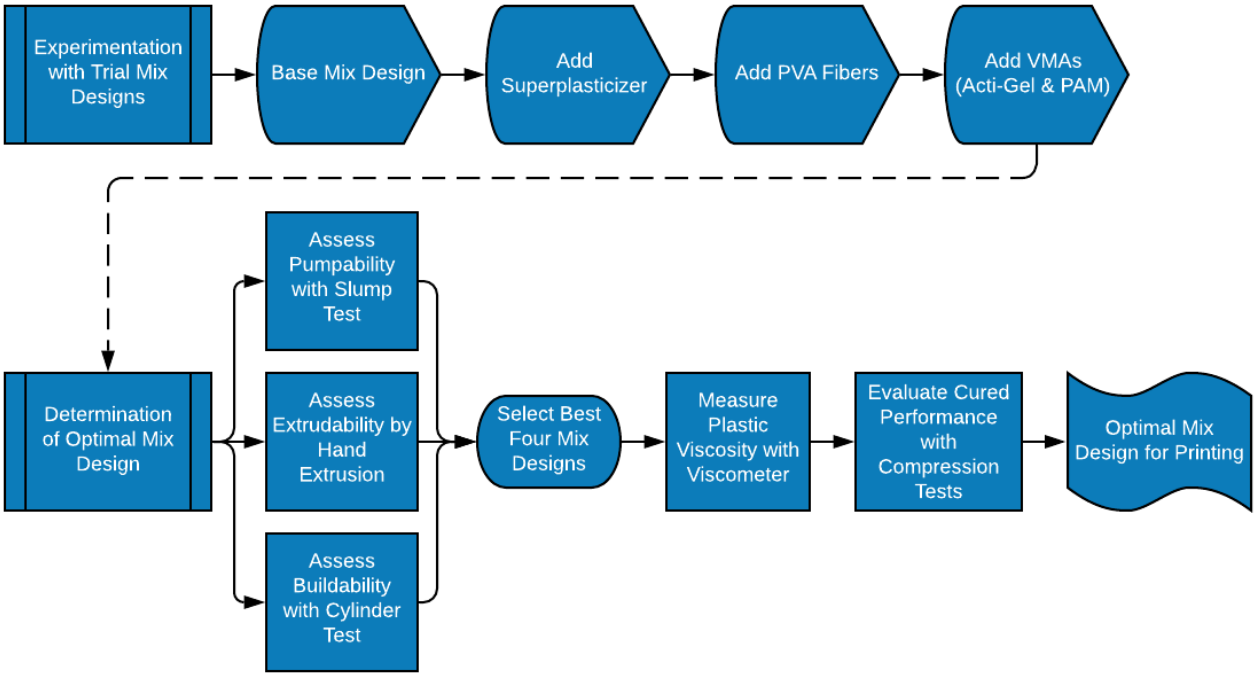

Figure 17: The mix design optimization flowchart shows the process by which the optimal mix design for 3D printing was determined. Experimentation began with trial mix designs containing only cement, silica fume, sand, and water. Admixtures and additives were added to the mix designs one at a time to experiment with the effects of each added component. Once a set number of mixtures were determined, the pumpability, extrudability, and buildability were assessed. Viscometry and compression tests were completed on the top four mix designs resulting in the optimal mix design for printing.

3.2.1. Pumpability

The test chosen to determine the pumpability of the fresh concrete was the standard ASTM C143 slump test. For this test, a standard slump cone was used with an internal diameter of 100 mm (3.94 in) at the top, 200 mm (7.87 in) at the bottom, and a total height of 300 mm (11.81 in) shown in Fig. 18. The concrete was scooped in three equal layers and rodded 25 times as each layer was placed per ASTM C143. Once the concrete had filled the slump cone, the rod was used to remove any excess concrete so that it was flush with the top of the cone. Then, the cone was immediately lifted upwards leaving the concrete in place. When this happened, the concrete experienced one of three slump categories: true slump, shear slump, or collapse slump. For the purpose of accuracy, any slump test that resulted in a shear slump or collapse slump was disregarded. A good pumpability was determined by a slump value that was higher than 50 mm (1.97 in), but no higher than 150 mm (5.91 in) (Draijer, 2007). The slump values for each mix design were used to estimate the initial yield stress of the concrete with Eq. 4 from section 2.1.1.

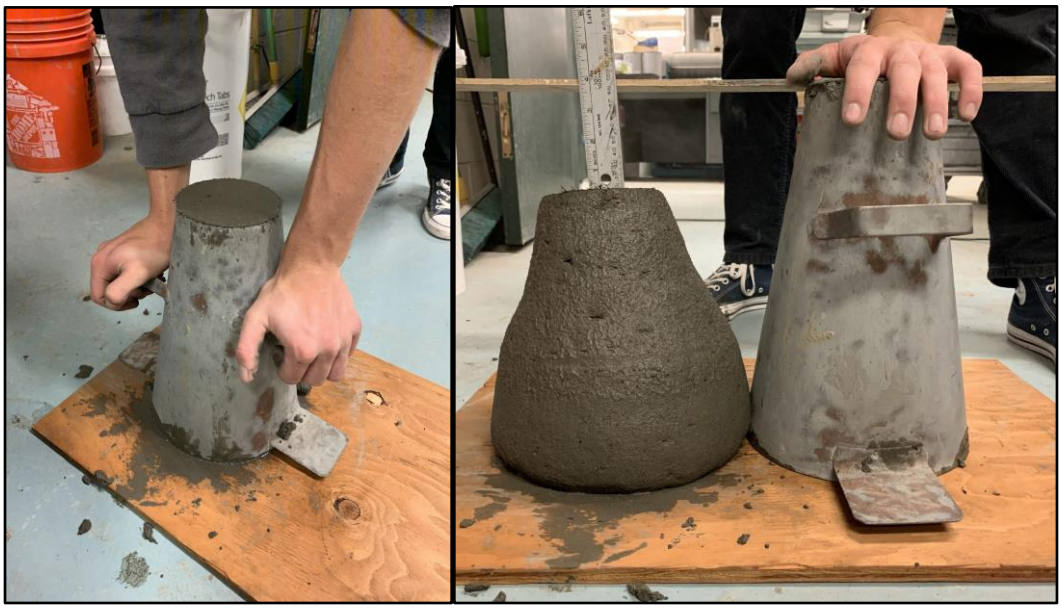

Figure 18: Standard slump cone complying to ASTM C143 used to assess pumpability.

3.2.2. Extrudability

The extrudability of the fresh concrete was determined using a 3D printed polymer nozzle with a rectangular opening measuring 40 mm (1.57 in) by 20 mm (0.79 in). The concrete was loaded into a PVC pipe with a 38.1 mm (1.50 in) inner diameter attached to a wooden frame. A 3D printed plunger was then used to push the concrete through the nozzle to simulate the printing process as seen in Fig. 19. The extrudability of each mix design was based on a visual inspection of the extruded filament. Each mix was then ranked in terms of their extrudability from one to nine, nine being the best and one being the worst. The rating was based on the consistency of the mix's flow during extrusion, the amount of excess water, the surface finish of the filament, and its deformation after extrusion.

Figure 19: Hand extrusion prototype used for extrudability testing consisting of a PVC pipe and 3D printed nozzle fastened to rollers on a wooden frame. Mix designs were ranked based on the consistency of the mix's flow during extrusion, the amount of excess water, the surface finish of the filament, and its deformation after extrusion.

3.2.3. Buildability

To determine the buildability of the concrete, a modified slump test was performed using the 101.6 mm (4 in) diameter by 101.6 mm (4 in) high slump cylinders from section 3.1. Each sample mix design was placed into four identical cylinders, which were removed at intervals of 20 minutes from zero to 60 minutes. The deformation at each interval was recorded to assess the buildability of each mix design. This test was used to compare the initial strength development of each mix design and estimate which mixtures had the highest structuration rates.

3.2.4. Viscometry

After assessing the pumpability, extrudability, and buildability of all mix designs, the best four mixture proportions were selected. These four mixtures were then tested using a Brookfield viscometer as seen in Fig 20. 300 mL of fresh concrete was measured and transferred into a plastic beaker. A number six disk spindle was used for all tests and viscometer readings of percent torque and viscosity were taken at increasing RPMs. The shear rate corresponding to

the spindle size and RPM was calculated using Eq. 12 to provide a data set showing the plastic viscosity versus shear rate (Brookfield Ametek, 2015).

Eq. 12) $$\gamma = \frac{2\omega R_c^2 R_b^2}{x^2(R_c^2 - R_b^2)}$$

$$\omega = \text{ angular velocity of spindle } [rad/sec] = \frac{2\pi}{60}N, where\ N = RPM$$
$$R_c = radius\ of\ container\ [cm]$$
$$R_b = radius\ of\ spindle\ [cm]$$
$$x = radius\ at\ which\ shear\ rate\ is\ being\ calculated\ [cm]$$

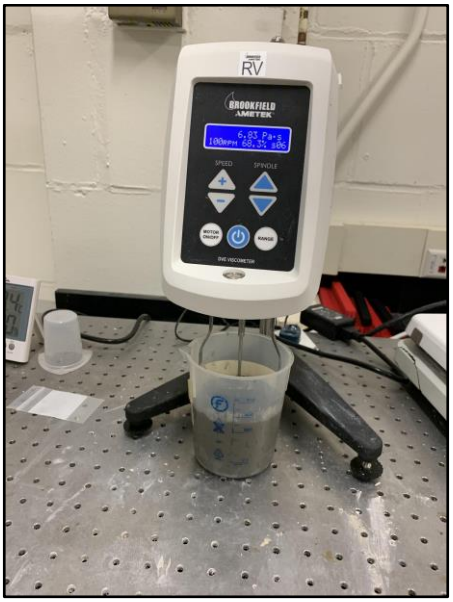

Figure 20: Image of the Brookfield viscometer with a concrete mix being measured.

The plastic viscosities, along with the results from the three previous tests, were used to make a final determination on the optimal mix design for printing. The mix design that had the lowest plastic viscosity while still maintaining a high enough structuration rate was chosen as the optimal mixture design for printable concrete.

3.2.5. Compression testing

Following viscometry, compression tests were conducted on the top four mixes and the base mix design, per ASTM C39/C39M-18. The samples were created by placing concrete into a 76.2 mm (3.0 in) by 152.4 mm (6.0 in) cylindrical mold as can be seen in Fig. 21. The mold was filled in quarters and rodded 25 times between each layer to ensure that the concrete filled the mold evenly. After the mold was full, it was placed on a vibrating table for one minute to eliminate any voids from rodding and to produce a good surface finish. The molds were then lightly covered with a plastic wrap and left to cure at room temperature, approximately 23 ^{o}C (73 ^{o}F), for 24 hours. After the initial curing period, the concrete was taken out of the molds and

placed into a cure room for another 13 days. The curing room maintained a constant temperature and humidity of 23°C (73°F) and 100%, respectively, per ASTM C511. Once the concrete was cured for 14 total days, the specimens were removed from the cylindrical molds (Fig. 22) and tested at a rate of 5.17 MPa/min (750 psi/min) using the Tinius Olsen universal testing machine as shown in Fig 23. An extensometer was attached to the specimens during testing to collect strain data. The compressive strength, Young's modulus, modulus of resilience, and toughness for the four mix designs were calculated from the stress-strain data. These parameters were compared to the ASTM standards for typical mortar, as well as the results for the base sample cylinders, to determine whether the VMAs had any effect on the properties of the cured mixtures.

Figure 21: Molds filled with wet concrete to be cured for the compression test.

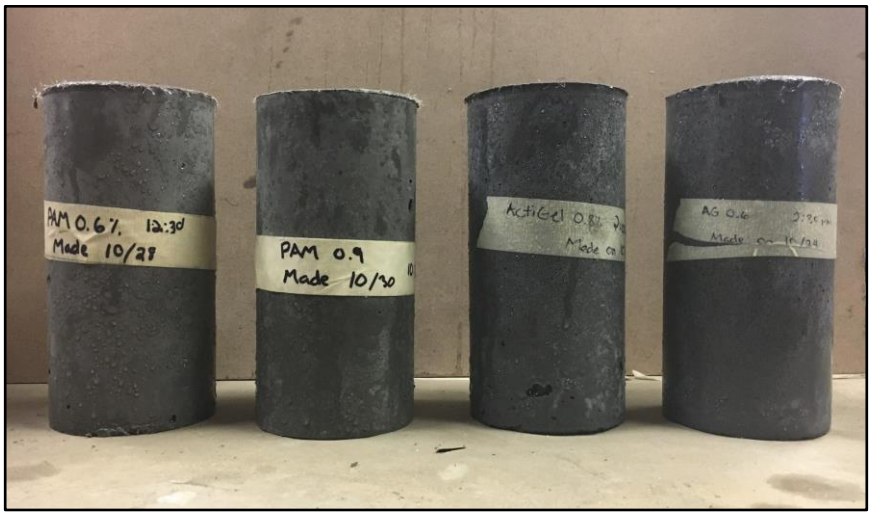

Figure 22: Fully cured cylinders ready for compression testing.

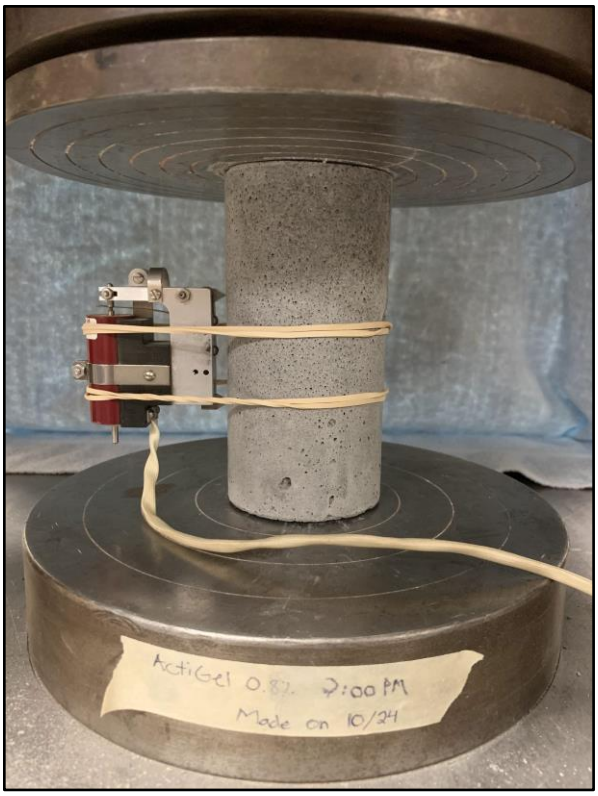

Figure 23: Test setup for compression testing including an extensometer to record strain values for the sample.

3.2.6. Scanning electron microscopy

The use of PAM as a flocculant in cement concrete is a recent development. As discussed in section 2.4.3, it has been suggested that this polymer is the most suitable VMA for printable concrete because of its ability to bridge between cement grains providing strong cohesion and resistance to deformation (Marchon et al., 2018). However, PAM has another benefit for 3D printing. It has been more recently discovered that PAM also provides increased bond strength in research on cement concrete roadway applications (CHINAFLOC, 2014). In order to extend this finding into the field of concrete 3D printing, the behavior of PAM at the layer interface was investigated using SEM. Two layers were extruded for SEM, one on top of the other, using the prototype hand extruder for mix designs B690SP1.2PVA0.25 and B571.2SP1.6PAM0.9. The printed layers for the PVA mixture were used as a control to which the microstructure of the layer interface of those including PAM could be compared. The layers were extruded one after another with an open time of approximately one minute between deposition of the first and second layers. Both printed samples were left at room temperature for one day lightly covered with plastic wrap, then moved into the cure room to cure for six more days. Following curing, the best section from each printed sample in terms of shape and surface quality were cut out of the printed layers using a diamond blade saw. These sections included the layer interface and were approximately 10 mm (0.39 in) thick, 20 mm (0.79 in) wide, and 20 mm (0.79 in) tall. Figure 24 shows an image of the two sections used in SEM. These sections were then vacuum dried for one hour per day for three days. SEM images were taken of the

interface between the layers as well as of the general cross section of the layers using a Phenom G1 SEM. This machine has a magnification range of 120X to 10,000X with a backscatter electron detector. Samples were mounted on specimen mount and blown with compressed air prior to loading them into the sample holder.

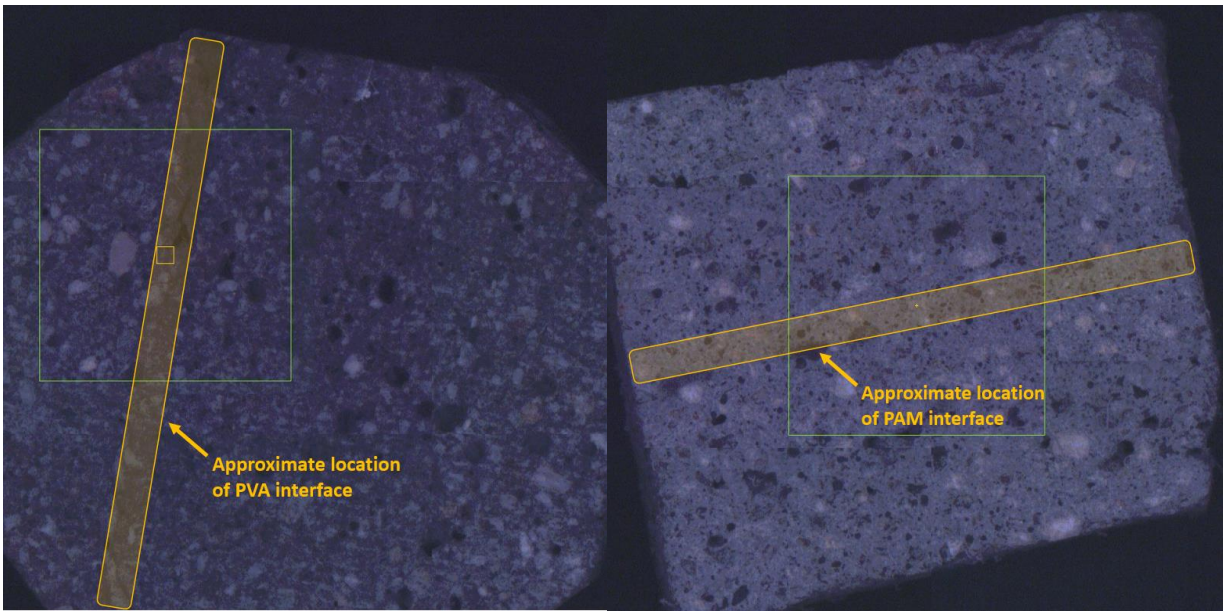

Figure 24: (Left) The section from printed layers with the PVA mix design used in SEM. (Right) The section from the printed layers for the PAM mix design used in SEM. The approximate location of the interface is highlighted in orange in each image.

3.3. Methods of improving interlayer bonding

Once the optimal concrete mix design was selected, experimentation with different methods of improving the interlayer bond strength began. In order to improve the bond between layers, two different methods were considered: spraying chemical adhesives prior to layer deposition and altering the nozzle and filament geometry to improve topological interlocking. In order to test these methods, samples were made to simulate the conditions of printed layers, cured for seven days, and the interfacial strength was tested using a modified version of the Brazilian disk test. The flowchart in Fig. 25 outlines the process for this stage in the research.

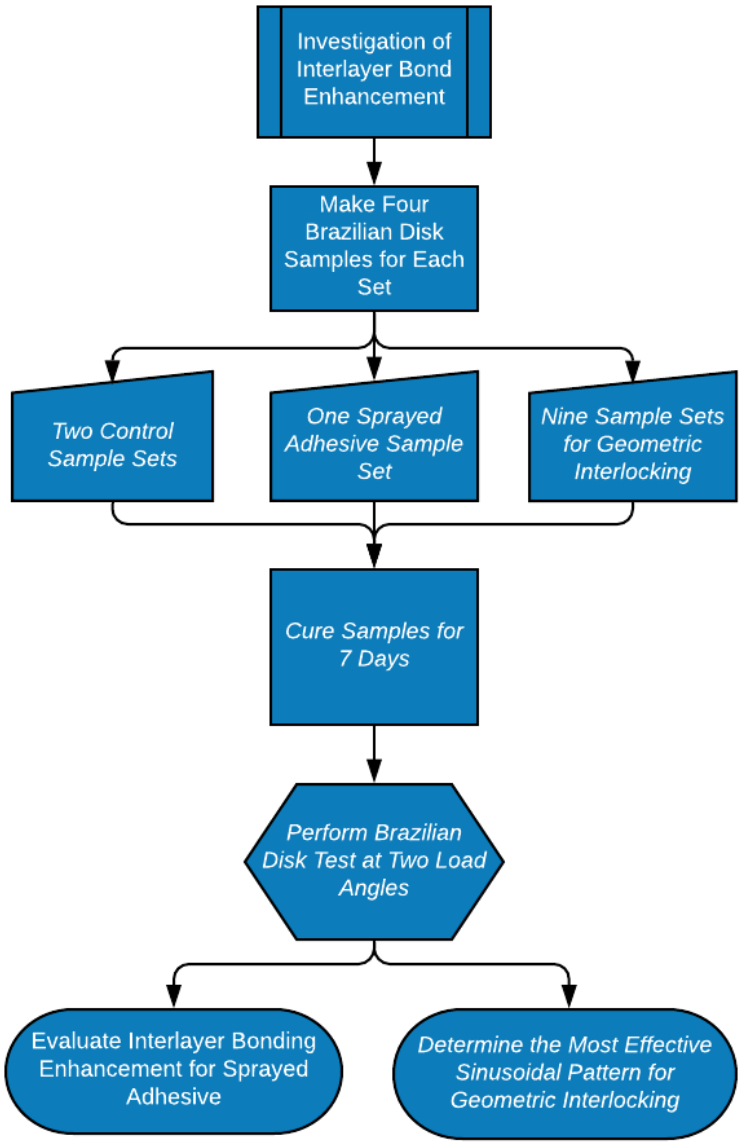

Figure 25: A total of 48 samples were made for the Brazilian disk test: 8 control samples (four whole disks with no interface and four with a flat interface), 36 samples for geometric interlocking using nine different sinusoidal patterns (four for each pattern), and four samples using a sprayed adhesive on a flat interface. Four disks were produced within each sample set to verify reproducibility of the results. These samples were tested at two different load angles, the results were compared to the control samples, and conclusions were made on the improvement to the interlayer bond for each method.

3.3.1. Sprayed chemical adhesive

The first method of enhancing interlayer bond strength that was tested involved using a liquid chemical adhesive at the bond interface. For this project, Concrete Bonding Adhesive by Quikrete was used. This is a polymeric resin and water-based adhesive that bonds fresh

concrete to cured concrete. After seven days of curing, this adhesive can offer up to 0.7 MPa (100 psi) of tensile bond strength (Concrete bonding adhesive.2018). The bonding adhesive was mixed with water to form a sprayable solution that was applied to the surface of the flat-interface disk samples using a brush (the idea being that the application of this adhesive could be automated in the future with a sprayer assembly). The solution consisted of two parts water and one part Quikrete Bonding Adhesive, by volume.

3.3.2. Geometric interlocking

The next means of improving interlayer bond strength was through altering the geometry of the printed filament to achieve a stronger mechanical connection between layers. Nine sinusoidal patterns were investigated for improvement to interlayer bonding. This was accomplished by producing the sinusoidal patterns at the interface between the halves of the Brazilian disk samples, an example of which is shown in Fig. 26. Figure 27 shows how a nozzle would create such sinusoidal patterns in the concrete filaments at extrusion. An added nozzle geometry would create grooves in the top and bottom surfaces of the freshly printed concrete filaments allowing the layers to lock together creating multiple small mechanical joints between the layers. The smooth sinusoidal shape is ideal because it limits the stress concentrations which occur at sharp corners. In theory, the added contact area between layers will enhance interlocking and provide more frictional resistance at the interface.

Figure 26: Example of a fully prepared sample for the Brazil disk test with a sinusoidal wave as the interface between the two halves of the concrete disk.

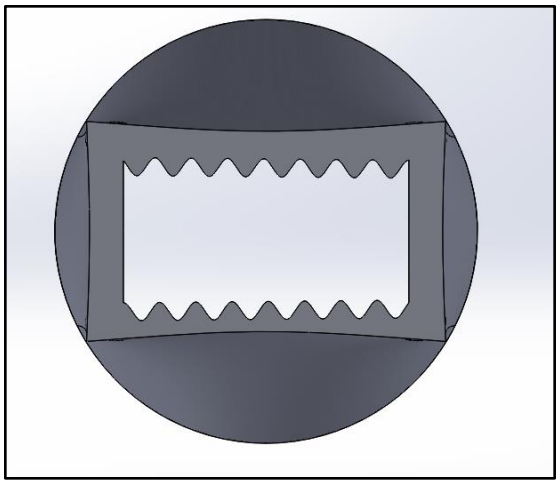

Figure 27: Bottom view, showing the extrusion end of a theoretical Solidworks model illustrating how a sinusoidal nozzle geometry could be used in construction applications to create geometric interlocking between printed layers.

3.3.3. Samples for the Brazilian disk test

In order to produce samples for the Brazilian disk test, silicone rubber molds were casted. These molds were made by pouring Mold Max 29NV silicone rubber compound into four identical forms. Each of these forms had three cylinders with a height of 40 mm (1.57 in) and a radius of 50 mm (1.97 in), equally spaced, as seen in Fig. 28. The formwork was removed from the silicone once it hardened creating four separate molds with three cylindrical pockets in each, providing the capacity to make 12 samples at once. Nine of these pockets were used for the sinusoidal samples, one was used for the sprayed adhesive samples, and two were used for the control samples. The nine sinusoidal patterns were combinations of three frequencies ($\pi/4$, $\pi/6$, and $\pi/12$) and three amplitudes (1 mm (0.04 in), 3 mm (0.12 in) and 5 mm (0.20 in)). The notation used for these patterns, and their corresponding geometries are detailed in Table 6.

Table 6: Sinusoidal patterns for interfacial testing indicating amplitude, frequency, and wavelength.

Notation	Amplitude (mm)	Frequency (rad)	Wavelength (mm)
1A	1	$\pi/4$	8
1B	1	$\pi/6$	12
1C	1	$\pi/12$	24
3A	3	$\pi/4$	8
3B	3	$\pi/6$	12
3C	3	$\pi/12$	24
5A	5	$\pi/4$	8
5B	5	$\pi/6$	12
5C	5	$\pi/12$	24

Figure 28: Pouring silicone rubber into forms to make molds for Brazilian disk samples.

As the silicone molds were solidifying, dividers were 3D printed for each sinusoidal wave, the adhesive sample, and the flat interface sample to cast the interface pattern into the first half of the Brazilian disk samples. Figure 29 is an example of one such divider. Once the silicone rubber was fully hardened, the dividers were placed in each of the molds, and concrete was poured into one half as seen in Fig. 30A and Fig. 30B. The samples were placed on a vibrating table while the molds were filled to ensure even packing of the molds. The concrete mix used was a mix with only superplasticizer and PVA fibers as additives (B690SP1.2PVA0.25) from previous testing to avoid unknown influences that could be caused by PAM or Acti-Gel. The fresh concrete was covered with a plastic wrap and left at room temperature. After one day of curing, the dividers were removed from the mold, leaving half-disk samples as shown in Fig. 30C. These half-disk samples were placed back into the rubber molds, and the other half was filled with the same mix of concrete. The full samples were again covered with plastic wrap and left to dry for one more day. The samples were then removed from the molds and placed in the curing room for six more days resulting in a total cure time of eight days for the first half and seven days for the second half. This process was repeated three more times to have four total samples for each set.

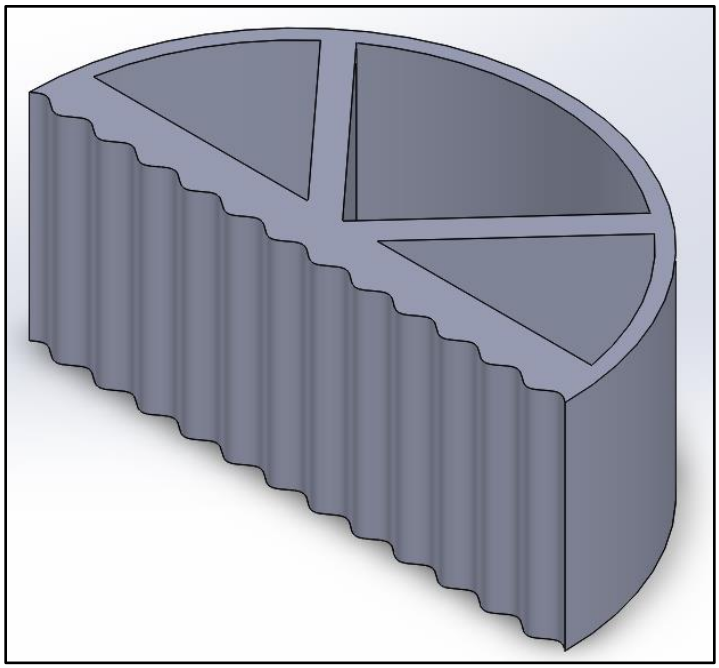

Figure 29: Solidworks model of a divider used to create the sinusoidal interface for the Brazilian disk samples.

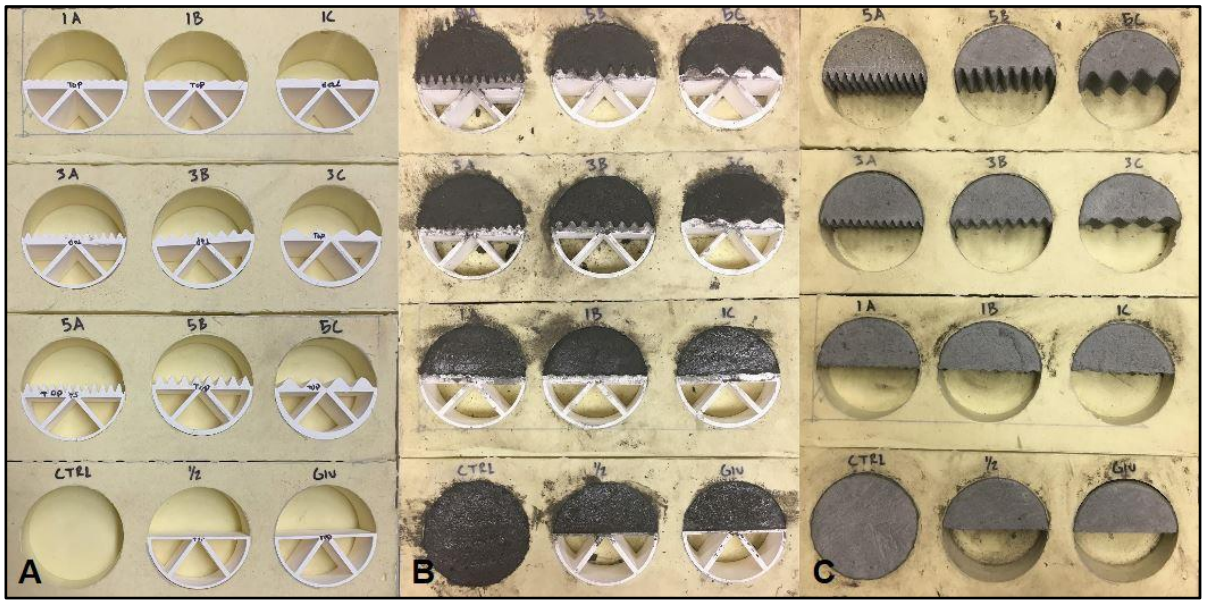

Figure 30: (A) Rubber molds with all 3D printed dividers. (B) All molds filled halfway with wet concrete with dividers. (C) One half of hardened concrete after dividers had been removed.

3.4. Interlayer bond testing

3.4.1 Brazilian disk test

To analyze the effectiveness of each method for improving the interlayer bond strength, the samples were tested with a modified version of the Brazilian disk test. This test is generally performed on samples with a notch along the axis of the interface, but for this project, the specimens were intact, made without a notch along the interface. The test was used to determine the interfacial fracture toughness in shear and tension for the samples (Rahbar, N. et al., 2010). The sample sets for each of the nine geometric interlocking patterns, the sprayed adhesive, and controls were tested with the interface at two different orientations relative to the applied loading. The load angles tested in this project were zero degrees which correlates to Mode I fracture, and 25^{o} which correlates to Mode II fracture (Rahbar et al., 2010; Rahbar et al., 2008). Two samples for each improvement method were tested at the two load angles. The test setup for the Brazilian disk test is shown in Fig. 31. All testing was done at a loading rate of 66,723 N/min (15,000 lb/min) using the Tinius Olsen universal testing machine. The maximum applied load resulting in fracture was recorded from each test and used to determine the fracture toughness for each interlayer bond improvement method with a MATLAB code provided by Professor Nima Rahbar. The results for each sample set were graphed and analyzed to determine which sinusoidal shape provided the greatest improvement in interlayer bond strength, and to determine if the sprayed adhesive provided any relevant improvement in tension or shear.

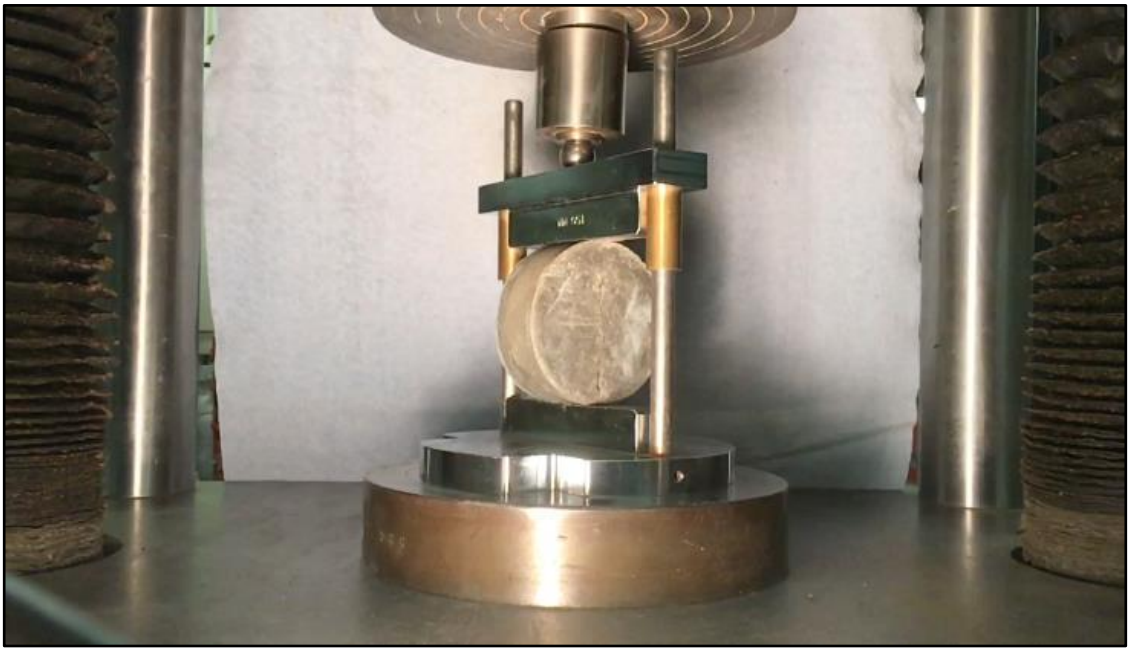

Figure 31: Test setup for Brazilian disk test in the Tinius Olsen universal testing machine.

3.5 Budget

Table 7: Project budget including costs for all materials used.

Item	Price/Unit	Quantity	Total
Materials			
Portland Cement	$12.15	3	$36.45
Fine Sand	$6.70	8	$53.60
Silica Sand	$16.53	1	$16.53
PVA Fibers	$11.79	1	$11.79
Polyacrylamide	$35.00	1	$35.00
Acti-Gel	Donated	-	-
Total			**$153.37**

4. Results

4.1 Trial mixture designs

4.1.1. Base mix designs

Experimentation with the reference design mixture began with a water to binder (W/B) ratio of 0.322. This ratio produced an extremely dry mixture, and the W/B ratio was increased incrementally to 0.581 at which point the mixture was deemed suitable as a reference for printable concrete. During the base mixture design trials, all of which are shown in Appendix B, experimentation with a play sand with a maximum particle size of 0.30 mm (0.012 in) indicated that using a smaller aggregate size significantly increases the workability of the mix. However, because a common fine sand with a maximum particle size of 2.36 mm (0.093 in) was much more available and cost effective for construction applications, the finer play sand was not used for the remainder of the project.

4.1.2. Superplasticizer mix designs

Once superplasticizer was added to the mix design, it was determined that a W/B ratio of 0.335 was ideal for a dose 1.0% superplasticizer by weight of binder. Additionally, it was found that maintaining the same W/B ratio but increasing the sand content increased the workability of the mixtures as shown by the cylinder slumps for trial mixtures B748SP1.0 through B707SP1.0 in Appendix C which tended to increase with increasing sand content. However, there was a limit to the amount of sand that would increase workability and the addition of superplasticizer did introduce some issues with segregation for mixes with less sand as observed with trial

mixture B871SP0.8.

4.1.3. Fiber mix designs

Polyvinyl alcohol fibers were initially added in doses of 0.5% by total volume as other research indicated that larger doses resulted in a loss of cohesiveness of the concrete (Noushini et al., 2013). Trial mixtures with 0.5% PVA fibers by total volume were highly cohesive. This was deemed a strong quality for the extrudability of the mix, but the strong cohesiveness of the 0.5% PVA mixtures limited the workability and made pumping extremely difficult. For instance, mix design B732SP1.0PVA0.5, which was the same proportions as B732SP1.0 only with fibers added, had a cylinder slump of 1.59 mm (0.0625 in) which was 3.175 mm (0.125 in) less than the mix without fibers. As a result, doses of 0.25% by total volume were used for the remainder of the trial mixtures. The 0.25% PVA fiber mixtures maintained a good cohesiveness while being much more workable than the mixes containing 0.5% PVA fibers. For example, using the 101.6 mm (4 in) diameter cylinder, trial mixture B690SP1.2PVA0.25 had a 3.175 mm (0.125 in) larger slump than B690SP1.2PVA0.5 having the same mixture proportions but less fibers. All PVA trial mixtures are shown in Appendix D.

4.1.4. Viscosity modifying admixture mix designs

4.1.4.1. Acti-Gel mix designs

The final trial mixtures experimented with two VMAs, Acti-Gel and PAM. It was found that Acti-Gel had little noticeable effect on the concrete at the recommended doses of 0.2% by weight of dry materials. However, an increasing dose incrementally resulted in a more cohesive mixture with better shape stability and a lower slump while maintaining workability. The largest dose of 1.2%, used in B671SP1.2AG1.2, led to less than a 1.59 mm (0.0625 in) slump with the 101.6 mm (4 in) diameter cylinder. This mixture was far too stiff and was not able to be extruded by hand. It was determined that a dose of about 0.6 to 0.8% provided the best green strength while maintaining pumpability. Mix designs B671SP1.6AG0.6 and B671SP1.6AG0.8 were selected for further testing.

4.1.4.2. Polyacrylamide mix designs

The effects of PAM on fresh concrete were found to be quite variable, as small changes in our mixing process led to drastic changes in fresh properties. The experimentation with PAM began with a dose of 9.0% by weight of binder. Initially, PAM was mixed with the dry materials before adding water or superplasticizer. Mix design B671SP1.6PAM9.0 produced a dry sandy mixture as the PAM seemed to soak up almost all of the water. However, after adding an additional 122.5 g of water, the concrete mix turned into a sticky and cohesive ball that resembled the consistency of dough, as shown in Fig. 32. Interestingly, after a full day of curing, it was found that the material could be deformed with the pressure of one finger. Mixes with lower PAM contents and varying water contents were iteratively tested, but each good mix design was difficult to reproduce. It was hypothesized that PAM's behavior in the concrete mix was entirely dependent on how the contents were mixed and when the water and PAM were added. When PAM was added as the last component, as in mix B571.2SP1.6PAM0.87, the mix changed within a minute from the consistency of soup (Fig. 33A) to that of dirt (Fig. 33B).

Additional water was added to this mix in 0.57 g doses (0.01 W/B) until it could be extruded by hand. Again, this mix procedure was reproduced and slightly altered in iterations, again giving varying results. After 18 trial mixtures, two mixes were deemed suitable for further investigation, one with 0.6% PAM (B571.2SP1.6PAM0.6) and one with 0.9% PAM (B571.2SP1.6PAM0.9) by weight of binder. Although, it should be noted that in one-liter quantities, both of these mix designs required the addition of a small amount of water after the addition of PAM to achieve the desired properties. When mixed in larger quantities, the required amount of excess water decreased. At the end of the mixing process, both of the chosen mix designs had a smooth and sticky consistency that was described in the lab as similar to the consistency of churned butter (Fig. 33C).

Figure 32: The initial PAM mixture B671SP1.6PAM9.0 clumped together during mixing showing the effects of PAM on the cohesiveness of concrete. At a dose of nine percent by weight of binder, PAM created such a cohesive mix that the concrete was labeled unpumpable.

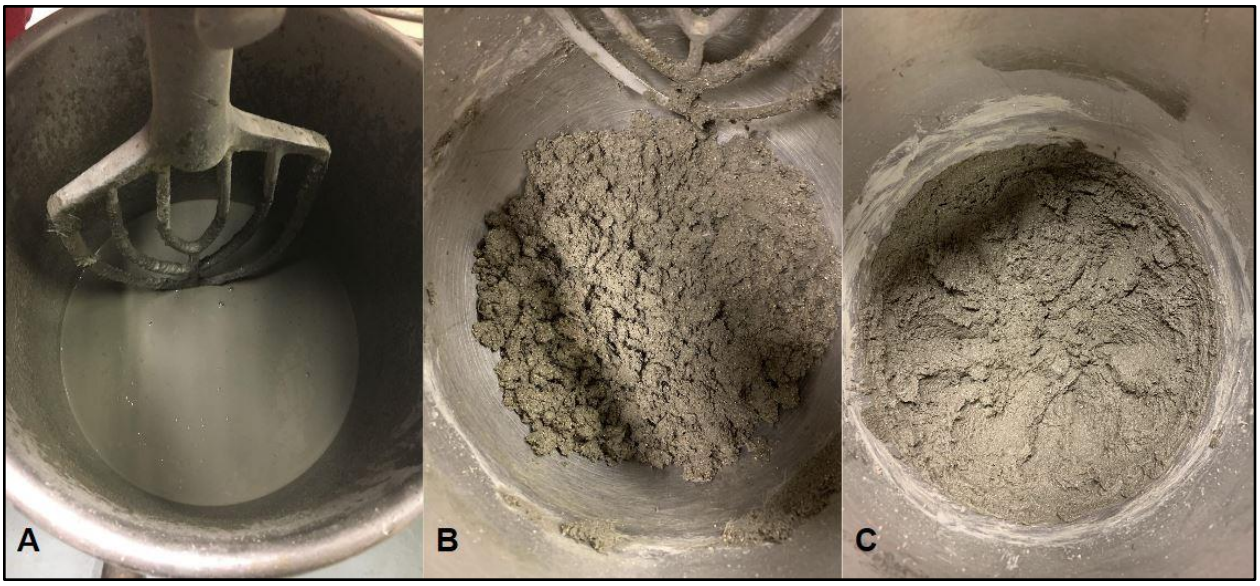

Figure 33: Images showing the effect of PAM during the mixing process: (A) The PAM mix before the addition of PAM was of liquid consistency. (B) Once PAM was added, it soaked up all the water, returning the mix to a dry, non-cohesive consistency. (C) Five grams of additional water mixed in at the end brought the mix to a perfect consistency for pumping.

4.2. Optimal mix design

4.2.1. Pumpability

The slump for each mix design was recorded immediately after mixing to investigate the green strength of the mixtures. Using Eq. 4 in section 2.1.1, the initial yield stress of all of the mixes was estimated from the slump value associated with the mix design. The results are tabulated in Table 8 below. The range of slump values fell between 34 mm (1.34 in) and 141 mm (5.55 in). Only the base mix design, B508SF, was determined to be an unpumpable mixture as its slump was below the lower limit for pumpable concrete of 50 mm (1.97 in) (Draijer, 2007). The high yield stress of 1524 Pa (0.22 psi) for the base mix would demand high pressure in the delivery system to initiate flow which could damage the system during the pumping process. All other mix designs were within pumpable limits. However, it was observed that mix design B571.2SP1.6PAM0.6 with 0.6% PAM adhered to the sides of the slump cone requiring a much slower extraction in order to determine a true slump value. This was also seen in the PAM 0.9% mix, but not to the same extent that was experienced within the PAM 0.6% mix. Figure 34 illustrates a ranked order of the yield stresses for the various mix designs from highest to lowest along with the corresponding slump values on the secondary axis. It should be noted that each yield stress was estimated from a single slump value. The yield stress for most mix designs fell between 1100 Pa and 1300 Pa (0.16 psi and 0.19 psi) which from Eq. 6 means that the mixtures could theoretically reach a printed height of approximately 80 to 90 mm (3.15 to 3.54 in) without accounting for any structuration. The exception is with the Acti-Gel mixes which had the largest slumps and consequently the lowest yield stresses of 918.5 Pa (0.13 psi) and 752.6 Pa (0.11 psi). Like PAM, Acti-Gel is a viscosity modifying admixture meant to increase the structuration of fresh concrete, yet this data demonstrates that the admixture seems to maintain

a low initial yield strength and high workability. This could indicate that effects of Acti-Gel on yield stress are delayed compared to PAM which showed a higher initial yield stress. However, a delay in yield stress development could be beneficial to pumpability as long as the subsequent structuration rate is high enough to satisfy the yield stress requirements for the build stage investigated in section 4.2.3. B671SP1.6AG0.8 did have a slightly higher yield strength than B671SP1.6AG0.6 which indicates that a larger dose of Acti-Gel induces particle flocculation and an increase in green strength. Due to the high workability and low initial yield strength, the two Acti-Gel mixes have the strongest rheological properties for pumpability.

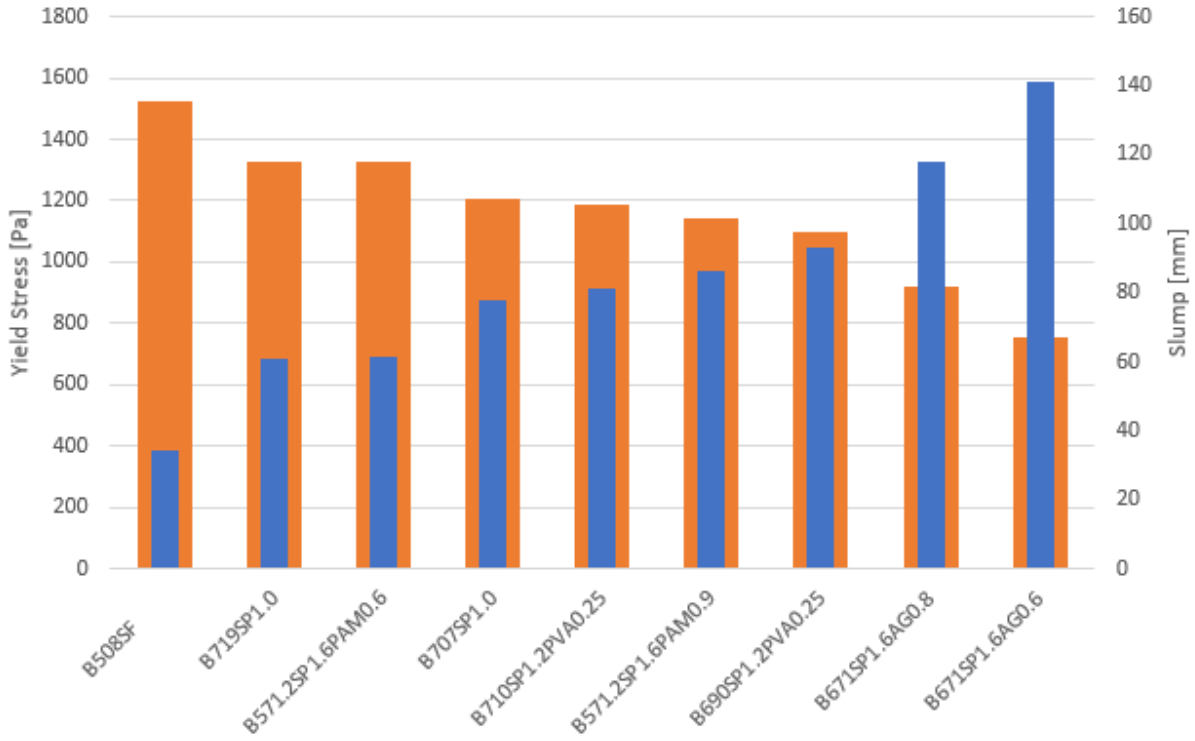

Figure 34: *Estimated yield stress (orange) and associated slump (blue) for each mix design ranked in decreasing and increasing order, respectively. Base mix B508SF was the only mixture with a slump below the pumpable limit. The Acti-Gel mix designs had notably low yield stresses compared to the other mix designs which ranged from 1100 Pa to 1300 Pa*.

Table 8: Slump values and corresponding yield stresses for all mix designs calculated with equation four.

Mix Design Label	Slump (mm)	Yield Stress (Pa)
Base		
B508SF	34	1524
Superplasticizer		
B719SP1.0	61	1330
B707SP1.0	78	1207
PVA Fibers		
B710SP1.2PVA0.25	81	1185
B690SP1.2PVA0.25	93	1099
Acti-Gel		
B671SP1.6AG0.6	141	752.6
B671SP1.6AG0.8	118	918.5
Polyacrylamide		
B571.2SP1.6PAM0.9	86.5	1146
B571.2SP1.6PAM0.6	61.5	1326

4.2.2. Extrudability

Each of the mix designs were ranked from one to nine in terms of extrudability, nine being the best and one being the worst. The rankings are summarized in Table 9.

Table 9: All mix designs ranked one through nine in terms of extrudability, where one corresponds to the worst extrudability and nine the best. The four VMA mix designs showed the best extrudability indicating the necessity of including VMAs in printable concrete. The mix design with 0.9% PAM is the top mix design for extrudability.

Extrudability Test	Ranking
Base	
B508SF	2
Superplasticizer	
B719SP1.0	4
B707SP1.0	1
PVA Fibers	
B710SP1.2PVA0.25	3
B690SP1.2PVA0.25	5
Acti-Gel	
B671SP1.6AG0.6	8
B671SP1.6AG0.8	6
Polyacrylamide	
B571.2SP1.6PAM0.9	9
B571.2SP1.6PAM0.6	7

The mixes that were ranked first through third were difficult to extrude through the nozzle, requiring a lot of pumping force. Due to the excessive force required to pump these mixes, it was challenging to maintain a steady flow of material. As a result, the extruded filaments for these mixes were discontinuous. For example, the extruded filament for the base mix design, B508SF, shown in Fig. 35, was broken into small pieces due to a lack of cohesion and an uneven flow. The mixes ranked fourth and fifth were slightly easier to push through the nozzle resulting in a smoother extrusion, yet still required significant force to initiate flow. Extrusion of these mix designs felt as though material was compacting within the nozzle inhibiting the extrusion of the concrete filament, until a large enough force was applied. Once the mixes began to flow, the filaments were much more cohesive, remaining intact as one filament during the extrusion, but did not hold their shape well after extrusion. Figure 36 shows the filament for mix design B690SP1.2PVA0.25 illustrating the deformed filament shape. The surface quality of the layers for these mix designs showed breaks and uneven thicknesses. The poor quality of these layers was in part a result of human error in controlling flow rate and print speed. Regardless, there was a clear lack of layer cohesion and shape retention for the mix

designs ranked fourth and fifth. The four VMA mix designs were ranked sixth through ninth due to their ease of pumping, the ability of each mix to retain their extruded shape, and the consistent surface quality of their layers. Mix design B571.2SP1.6PAM0.9 was ranked the best for extrudability and the results from its extrusion can be seen in Fig. 37. This mix design maintained its rectangular shape without deformation or inconsistencies along its layer displaying the benefits of PAM's cohesiveness for extrudability. Additionally, this mix was noticeably easier to push through the nozzle, requiring the least amount of pumping force, which allowed for a controlled flow rate. Mix design B671SP1.6AG0.6 was slightly more difficult to control but was otherwise similar to B571.2SP1.6PAM0.9 and was therefore ranked second in terms of extrudability, followed by B571.2SP1.6PAM0.6 and B671SP1.6AG0.8. These results exhibit the necessity of VMAs for printable concrete in order to achieve an extrudable mix with strong cohesiveness and shape stability.

Figure 35: Extrusion of base mix design, B508SF, illustrates the discontinuous filaments seen in the mixes ranked first through third. These mixes were difficult to pump and lacked cohesion.

Figure 36: Filament for mix design B690SP1.2PVA0.25 illustrating the deformed filament shape. The surface quality of the layers for the mix designs ranked fourth and fifth showed breaks and uneven thicknesses. There was a clear lack of layer cohesion and shape retention for these mix designs.

Figure 37: (Left) Extruded filament for PAM mix B571.2SP1.6PAM0.9. (Right) PAM mix B571.2SP1.6PAM0.9 being extruded from the nozzle. This mix retained its shape without noticeable deformation and produced a continuous layer. Any inconsistencies can be attributed to human error during extrusion.

4.2.3. Buildability

The cylinder slump tests conducted on each mix design at 20-minute intervals produced the following curves shown below allowing for assessment of the structuration of each mix. There are four different graphs (Fig. 38-41) for each of the four different admixtures that were used: superplasticizer, PVA fibers, Acti-Gel and polyacrylamide. Each individual graph plots both of the mix designs that were chosen in each group, as well as the buildability slope of the base mix design for reference.

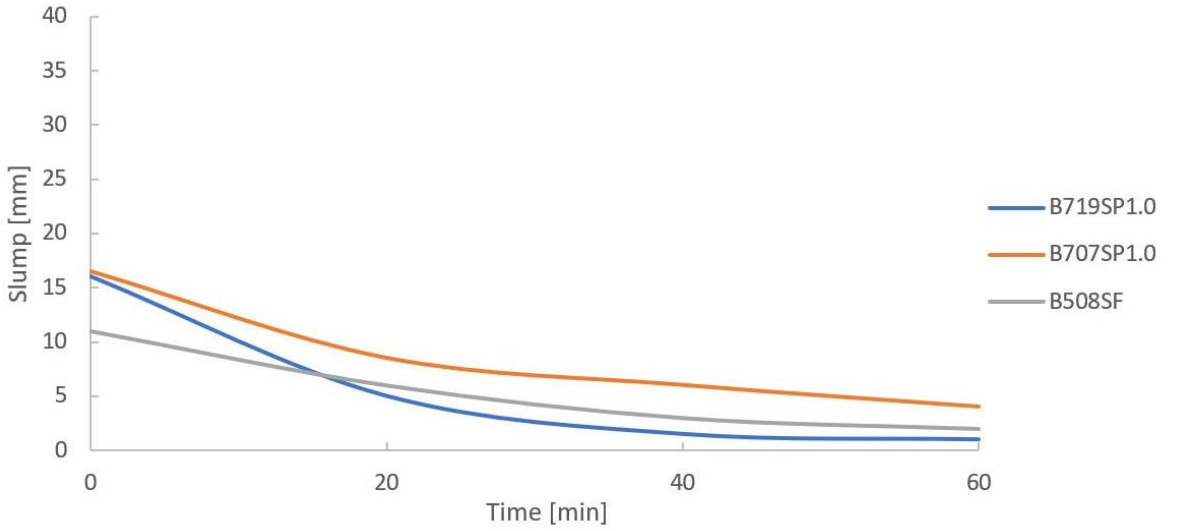

Figure 38: Buildability slopes for superplasticizer mix designs B719SP1.0 and B707SP1.0. Although slightly more workable initially, the slopes match that of the base mix design.

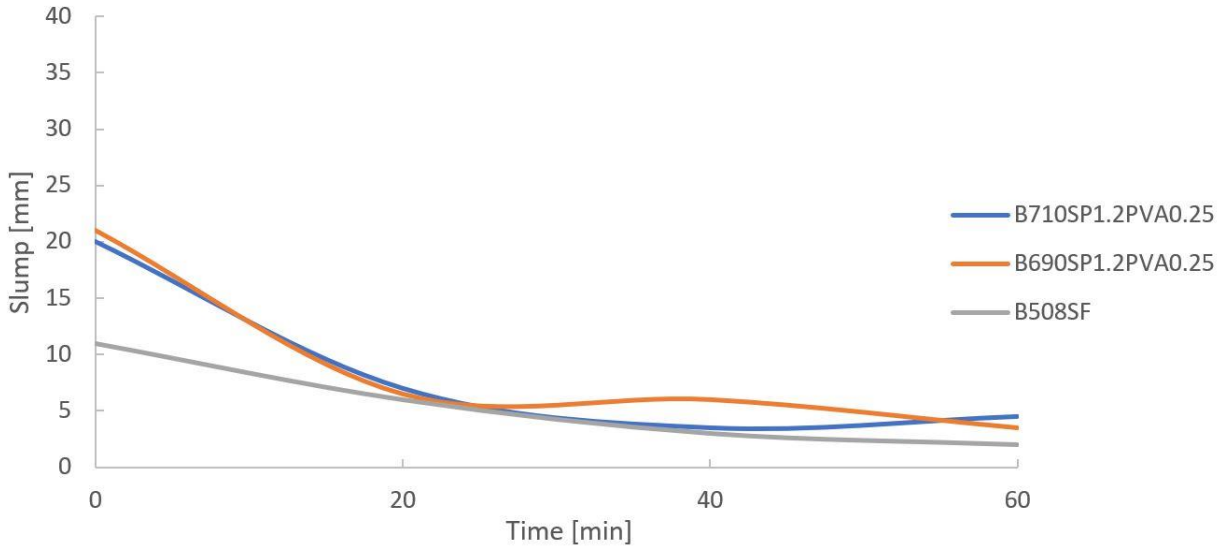

Figure 39: Buildability slopes for PVA fiber mix designs B710SP1.2PVA0.25 and B690SP1.2PVA0.25. The PVA mixes, which included more superplasticizer, also show a higher initial slump but generally follow the same slope of the base mix.

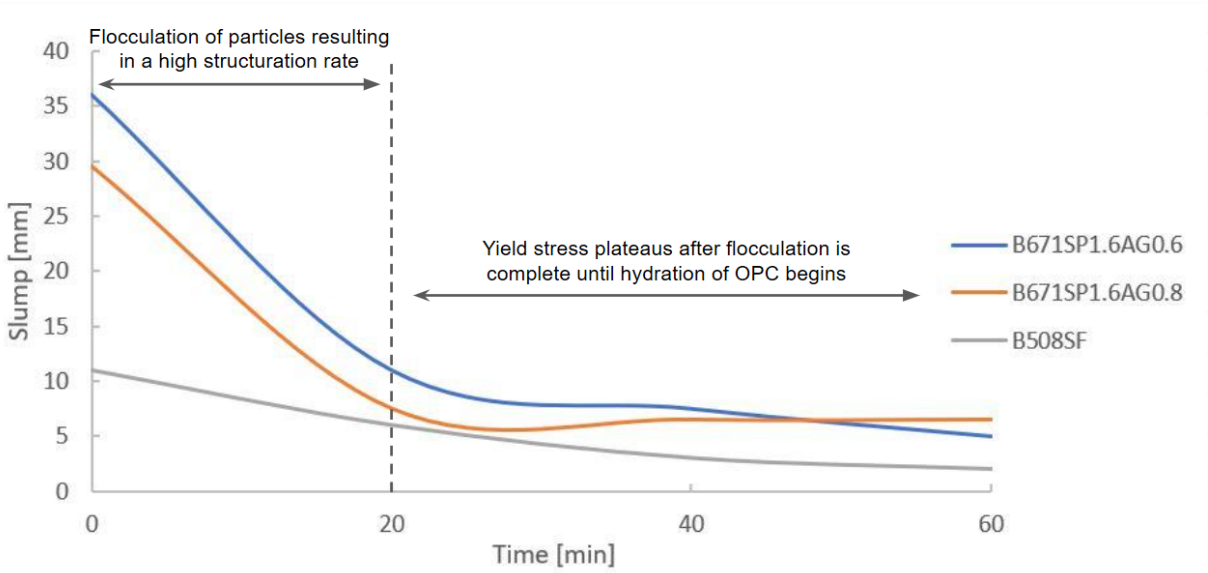

Figure 40: Buildability slopes for Acti-Gel mix designs B671SP1.6AG0.6 B671SP1.6AG0.8. The Acti-Gel mixes showed the lowest initial yield stress and highest structuration rate between zero and 20 minutes. The initial structuration is due to particle flocculation which plateaus after cement particles settle into their final network structure. This plateau is seen after 20 minutes. Although the high initial workability is advantageous for pumpability, the delayed structuration and higher long-term slump values are a disadvantage for the build stage.

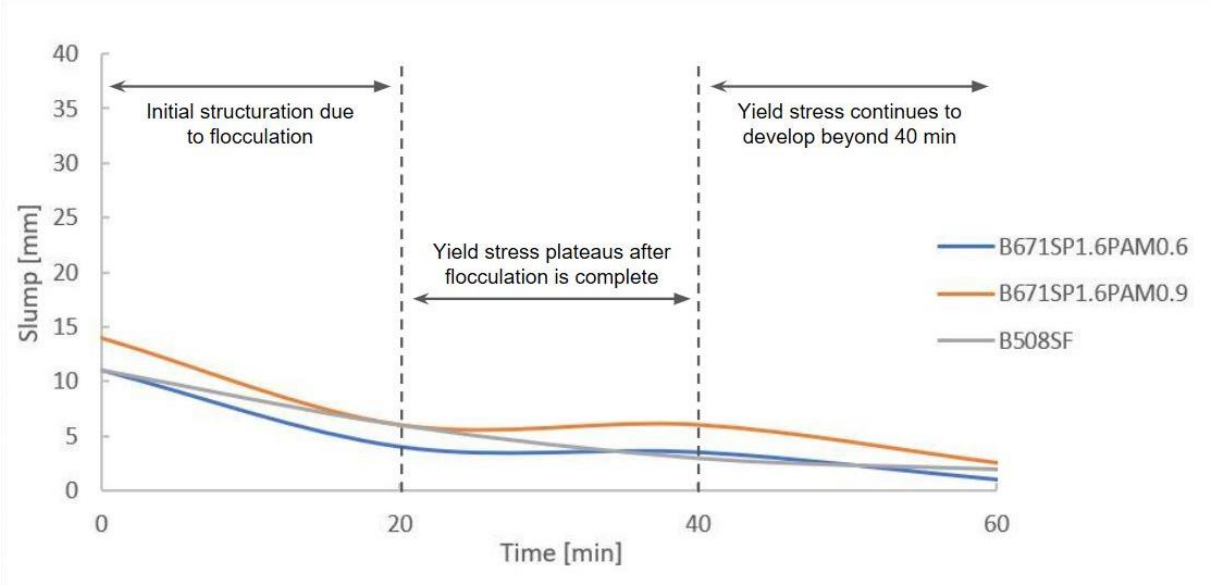

Figure 41: Buildability slopes for polyacrylamide mix designs B671SP1.6PAM0.6 and B671SP1.6PAM0.9. The PAM mix designs show the same initial flocculation period between zero and 20 minutes followed by a constant yield stress between 20 and 40 minutes. The difference with PAM is the continuation of yield stress development beyond 40 minutes. This results in the PAM mixes having higher long-term yield stresses and stronger performance in the build stage when compared to Acti-Gel.

The graphs for mixes with the superplasticizer, PVA fibers, and polyacrylamide have similar curves to one another. Each of these curves closely resemble the slope of the base mix design beginning with a slump of between 11 mm (0.43 in) and 21 mm (0.83 in) and decreasing to a final slump of between 1 mm (0.04 in) and 5 mm (0.20 in). The Acti-Gel mixes were a standout amongst all of the mixes for the buildability tests. They had a noticeably high slump at zero minutes, almost doubling the slump of the PAM mix designs and tripling the slump of the base mix design. Despite the large slump in the first interval, the slump dropped to almost match all the other curves after 20 minutes, at which point the structuration rate began to plateau as indicated in Fig. 40. This plateau was also seen with the PAM mixes between 20 and 40 minutes and is a result of particle flocculation ceasing (Fig. 41). The largest decrease in slump over the full 60 minutes for mixes not including Acti-Gel was 17.5 mm (0.69 in) for mix design B690SP1.2PVA0.25. These results confirm the hypothesis from section 4.2.1 on pumpability that the effects of Acti-Gel on flocculation and structuration take longer to develop than for PAM. This is demonstrated by the steep decrease in slump for the Acti-Gel mixes between zero and 20 minutes, while the PAM curves begin with a low slump value at zero minutes, indicating the effect of PAM on yield stress is more immediate but less dramatic. It can be seen in Fig. 41 that, after plateauing, the yield stress of the PAM mixes continued to develop beyond 40 minutes, whereas, with Acti-Gel, the yield stress remained relatively constant beyond 20 minutes. This could be a result of PAM interacting with the hydroxyl groups in the PVA fibers which enhances the absorption of PAM on cement grains (Bessaies-Bey et al., 2015).

Analysis of these graphs lead to the conclusion that the mixtures containing Acti-Gel had the highest structuration rate of all the mixes between zero and 20 minutes. The effects of Acti-

Gel on yield strength are ideal for the pumping stage as the mixes containing the VMA remained more workable than the others. However, the PAM mix designs, although not displaying the dramatic structuration rate seen in Acti-Gel, continued to develop yield stress beyond 40 minutes and had about 4 mm (0.16 in) less slump on average than the Acti-Gel mixes at 60 minutes indicating that they displayed a higher long-term yield strength. Furthermore, the delayed structuration seen with Acti-Gel would require slower print speeds and longer build times to allow for sufficient yield stress to develop when compared to the PAM mix designs. Due to its ability to induce quick and lasting structuration, PAM has a slight edge over Acti-Gel for buildability, as additional filaments can be layered almost immediately after each extrusion.

4.2.4. Viscometry

From the previous testing on pumpability, extrudability, and buildability, the four VMA mix designs were found to display the best rheological properties for printing. For simplicity, the four mix designs B671SP1.6AG0.6, B671SP1.6AG0.8, B571.2SP1.6PAM0.6, and B571.2SP1.6PAM0.9 will be referred to as Acti-Gel 0.6%, Acti-Gel 0.8%, PAM 0.6%, and PAM 0.9%, respectively. Viscometry on these four mix designs yielded data to help understand the non-Newtonian behavior of each mix. The raw data is compiled in Appendices F-J. Readings of viscosity are graphed against the shear rate on a logarithmic scale in Fig. 42. The viscosity data for the base mix design is plotted as a reference. In this graph, the slope of each line indicates the degree of non-Newtonian flow (Brookfield Ametek, 2015). At the lowest shear rate, Acti-Gel 0.8% had the lowest viscosity for the VMA mix designs, 1853 Pa•s (0.27 psi•s), followed by PAM 0.6% with a viscosity of 1937 Pa•s (0.28 psi•s), Acti-Gel 0.6% with a viscosity of 2127 Pa•s (0.31 psi•s), and finally PAM 0.9% with the highest viscosity of 2317 Pa•s (0.34 psi•s). However, the viscosity of PAM 0.6% quickly dropped with increasing shear rate and remained the VMA mixture with the lowest plastic viscosity until the shear rate reaches 10.784 s^{-1}. All four VMA mixes displayed higher viscosities than the base mix for all shear rates. Another notable result from this graph is the spike in viscosity for both Acti-Gel mixtures from a shear rate of 0.1078 s^{-1} (0.5 RPM) to 0.1294 s^{-1} (0.6 RPM) indicated on Fig. 42 while the curves for both PAM mixtures remained smooth. This could be due to the material reconfiguring after the spindle reached a high enough rate. The base mix design also had a slight discontinuity at the same change in shear rate. In general, the PAM mixes were much more cohesive which may have allowed for more accurate viscosity readings, avoiding this discontinuity. The Acti-Gel 0.6% appears to have maintained the second lowest viscosity, but the difference between PAM 0.9% and Acti-Gel 0.8% is difficult to discern, and the curves for all four mixes appear to converge as the shear rate increases. All mix designs, including the base mix, displayed pseudo-plastic, non-Newtonian flow behavior meaning that the apparent viscosity decreased with increasing shear rate (Brookfield Ametek, 2015). This inverse relationship between viscosity and shear rate illustrates the property called shear-thinning discussed with nano-clays in section 2.4.2.2. Interestingly, the viscosity of all four VMA mix designs dropped significantly faster than the viscosity of the base mix design, indicating that the VMA mixes exhibit greater shear-thinning than a standard mortar mix. From the plot, it can be seen that PAM 0.9% exhibited the highest degree of shear-thinning as it displayed the largest drop in viscosity over the range of shear rates. In terms of shear-thinning, PAM 0.9% is followed by Acti-Gel 0.6%, PAM 0.6%, and finally Acti-Gel 0.8%. This ranking in terms of shear-thinning parallels the ranking of the VMA mixes for

extrudability shown in Table 9. This is a notable observation as it confirms that greater shear-thinning behavior allows for easier pumping and extrusion.

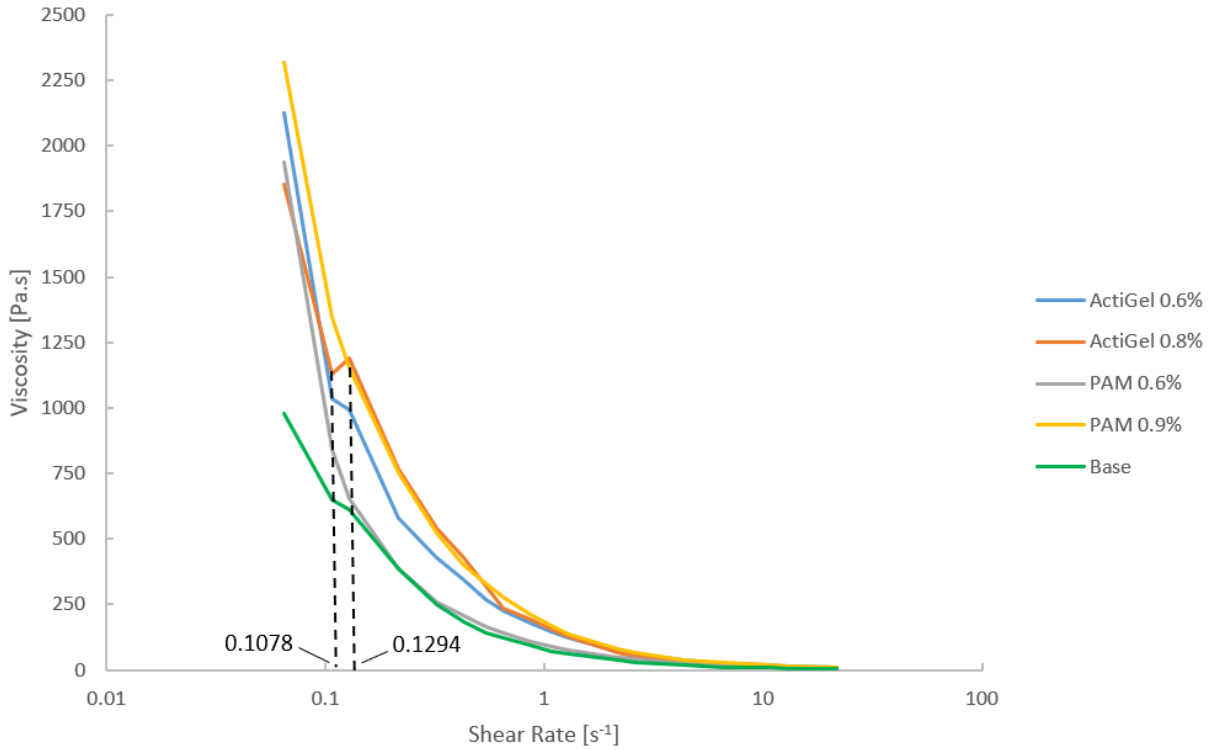

Figure 42: Plot of viscosity versus shear rate on a logarithmic scale. This graph shows the non-Newtonian behavior of all VMA mix designs compared to the base mix. Each mix exhibits the thixotropic property called shear-thinning, displaying lower viscosities with increasing shear rate. PAM 0.9% demonstrates the highest shear-thinning, and interestingly was also the easiest mix to pump during extrusion testing. A notable discontinuity appears between the shear rates of 0.1078 s^{-1} to 0.1294 s^{-1} for all mixes except for those including PAM.

Figure 43 gives another representation of the data showing spindle speed versus viscosity on a log-log scale. This plot provides a clearer distinction in the viscosities of the mixtures at higher shear rates. PAM 0.6% and Acti-Gel 0.8% had lower viscosities at high shear rates than PAM 0.9% and Acti-Gel 0.6%. This plot is also further evidence of the difference in viscosities of the VMA mix designs compared to the base which was clearly lower for all shear rates. The base mix, having a significantly lower plastic viscosity, indicates a lack of cohesiveness for concrete without VMAs. Because PAM and Acti-Gel act as flocculants, they provide cohesiveness to the fresh concrete which holds the mix together as it is sheared by the spindle, increasing the viscosity. Conversely, the base mix had significantly less cohesion, and as a result, the mix was easily sheared apart, and the apparent viscosity was much lower. PAM 0.9%, with the highest overall viscosity, was the most cohesive mix. This cohesiveness is beneficial to extrudability providing a continuous and well-controlled filament as seen in the extrusion results, while maintaining pumpability due to its shear-thinning behavior exhibited in Fig. 42.

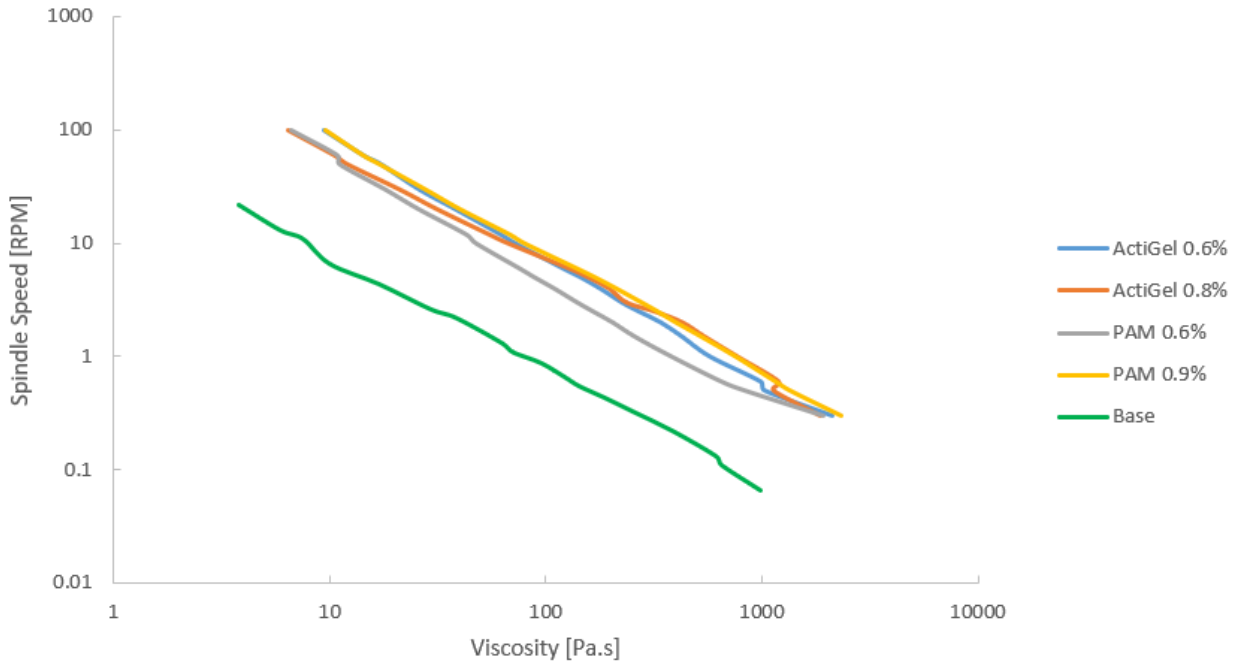

Figure 43: Plot of spindle speed versus viscosity on a log-log scale showing the difference between the base mix and the VMA mixes. The VMA mixes have higher viscosities at all shear rates corresponding to the high cohesiveness of all VMA mixes. These results suggest that PAM 0.9% is overall the most cohesive mix which was confirmed in the extrusion results by the well-controlled, continuous filament.

4.2.5. Compression testing

4.2.5.1. Stress-strain data

Plots of stress versus strain for the base and four VMA mix designs are shown in Appendix K. From the stress-strain data, four key parameters were calculated for each mix design: compressive strength, Young's modulus, modulus of resilience, and toughness. An illustration of how these parameters were obtained is shown on the stress-strain plot for Acti-Gel 0.8% in Fig. 44 and Fig. 45. The values for each parameter are tabulated in Table 10 below.

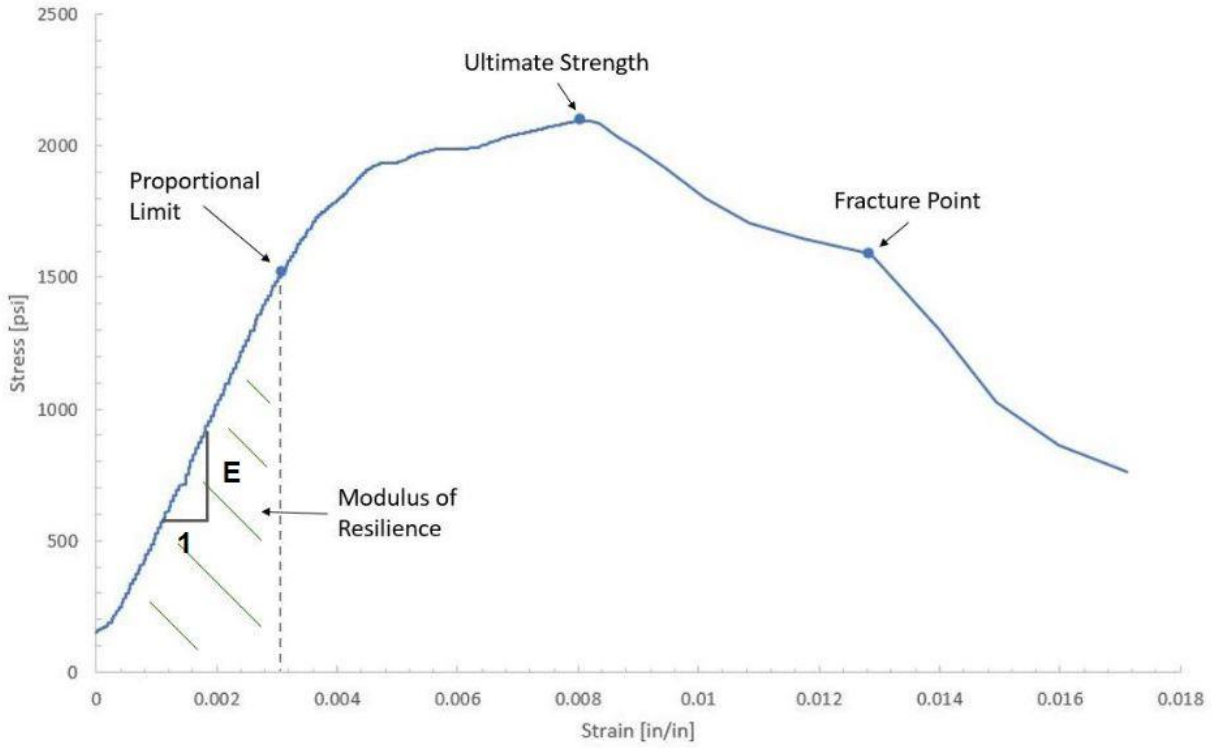

Figure 44: Illustration of modulus of resilience shaded in green as the area under the elastic region of the stress-strain curve. The modulus of resilience corresponds to the energy absorbed prior to plastic deformation. Young's modulus, proportional limit, ultimate strength, and fracture point are also indicated on the curve.

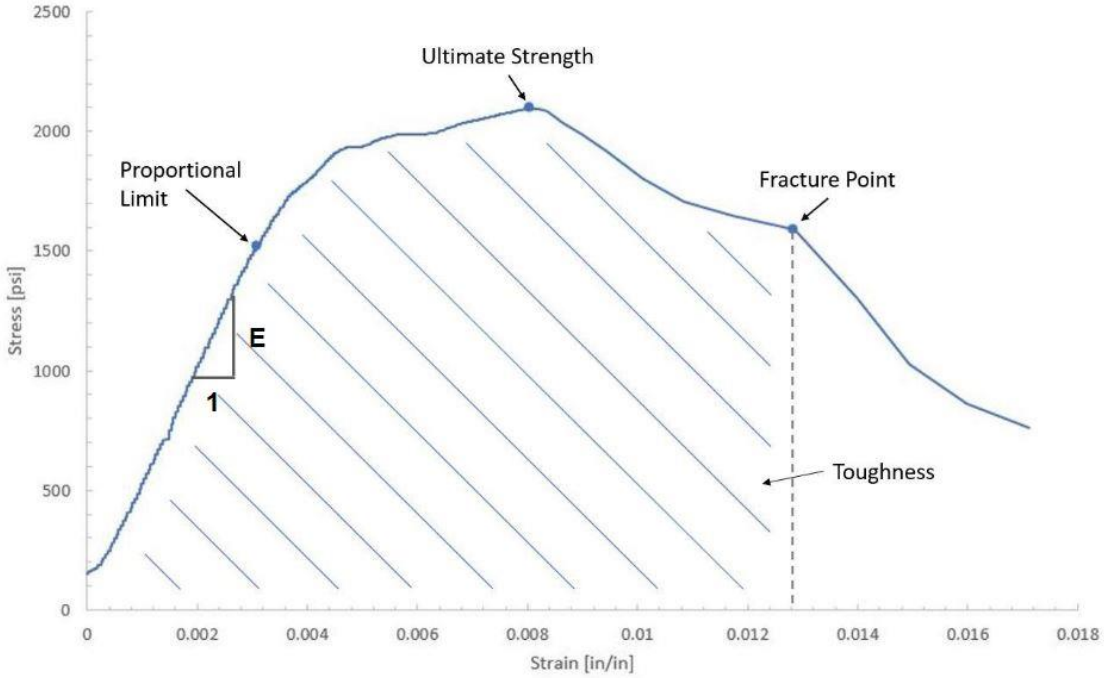

Figure 45: Illustration of toughness shaded in blue as the area under the stress-strain curve up to the point of fracture. The toughness corresponds to the total energy absorbed prior to fracture. Young's modulus, proportional limit, ultimate strength, and fracture point are also indicated on the curve.

Table 10: Parameters obtained from compression test data. Values of compressive strength, Young's modulus, modulus of resilience, and toughness are provided for the four VMA mix designs and the base mix.

Mix Design	**Compressive Strength, f'_c (MPa)**	**Young's Modulus, E (GPa)**	**Modulus of Resilience, U_r (kJ/m^3)**	**Toughness, U_T (kJ/m^3)**
Base	15.72	3.19	30.68	110.52
Acti-Gel 0.6%	16.89	2.83	22.48	108.87
Acti-Gel 0.8%	14.45	3.31	15.31	129.41
PAM 0.6%	14.61	2.34	23.79	107.56
PAM 0.9%	14.55	2.55	14.13	120.24

Acti-Gel 0.6% had a slightly higher compressive strength than the other mixes, but overall the strengths were similar for all mix designs. The compressive strengths for the PAM mix designs were only about 7% less than that of the base mix, and Acti-Gel 0.8% had about the same strength. This data does not indicate any notable effects on strength due to the

addition of PAM or Acti-Gel. As a comparison, typical Type N mortar has a compressive strength between 10.34 and 16.55 MPa (1500 and 2400 psi) within which all of the mixes fell except Acti-Gel 0.6% which showed a slightly higher strength. The values for Young's modulus, which correlate to the material's stiffness, show that the Acti-Gel mix designs were stiffer than the mix designs containing PAM. This is not a surprising result as it was hypothesized with trial mixture B671SP1.6PAM9.0 that large doses of PAM reduce the stiffness of the cured concrete. However, PAM 0.6% had a lower Young's modulus than PAM 0.9% which is contrary to this hypothesis. The modulus of PAM 0.6% and PAM 0.9% remained close to the typical modulus of mortar which is around 2.65 GPa ($3.84x10^5$ psi) (Narayanan & Sirajuddin, n.d.). These results do not indicate that small doses of PAM have a significant effect on the strength or stiffness of cured concrete.

The values for modulus of resilience, which correlates to the amount of energy a material is able to absorb within its elastic region, show that the mix designs with less VMA, Acti-Gel 0.6% and PAM 0.6%, were able to absorb a greater amount of energy prior to plastic deformation. These mix designs had a longer elastic region extending to a strain of approximately 0.004, whereas the elastic region for Acti-Gel 0.8% and PAM 0.9% ended at a strain of about 0.003. However, the base mix had the largest modulus of resilience of 30.68 kJ/m^3 and the largest elastic region, extending to a strain of approximately 0.0043. Conversely, the specimens with a larger quantity of VMA had a higher toughness meaning they were able to absorb more energy prior to fracture. The higher toughness and smaller resilience of Acti-Gel 0.8% and PAM 0.9% indicates that the mixes with more PAM and Acti-Gel were able to absorb more overall energy before fracture than the other three mix designs.

When the stress-strain graphs for base and Acti-Gel are compared to those of PAM, it is apparent that the transitions on the PAM graphs are much more subtle. The proportional limit, compressive strength, and fracture point are much less defined on the PAM curves. As a result, it is difficult to accurately distinguish the exact point of fracture for the PAM specimens, and the overall toughness values could be slightly higher than those estimated in Table 10. This smooth stress-strain behavior demonstrates that PAM, which is a ductile material, likely enhances the plastic behavior of concrete which otherwise is a brittle material with distinct transitions, as seen with the base and Acti-Gel mixes. In particular, the base mix, with a small plastic region and sharp transitions, was more brittle than the other mixes. The inclusion of fibers may have also increased the plasticity of the VMA mixes. Overall, neither PAM nor Acti-Gel, in the doses investigated, had any obvious negative effects that would inhibit their use in printable concretes.

4.2.5.2. Macroscopic investigation of compression specimens

A macroscopic investigation of the compression samples after failure showed the behavior of the fibers at failure. Images of the interior of cracks in the specimens displayed fiber bridging and fracture across the cracks. From the macroscopic images shown in Fig. 46 and Fig. 47, it can be seen that a majority of the fibers fractured across the crack interfaces while only a few remained intact bridging the crack. For instance, in Fig. 46, only one bridging fiber could be seen while approximately six fractured fibers were visible. This suggests that the dose of 0.25% fibers by volume may not provide sufficient reinforcement to resist crack propagation, but further investigation would need to be conducted with varying doses of fibers. Another pertinent observation is the even distribution and random orientation of the fibers throughout the

samples. This indicates that the mixing procedure of adding the fibers slowly to the wet materials while mixing sufficiently distributes the fibers throughout the mix (Appendix A). Conversely, at the surface of the samples, the fibers were oriented longitudinally along the length of the sample. This is most likely a result of the preparation of the compression cylinders. While filing the molds and tamping, the contact between the concrete and mold surface oriented the surface fibers vertically in the direction that the material was placed into the molds. Microscopic images of an extruded layer illustrate that the extrusion of a mixture through the nozzle also resulted in orientation of surface fibers along the length of the layers (Fig. 48). Figure 49 shows the fibers on the interior of the same layer also oriented along the layer. If the pumping and extrusion of layers orients a majority of fibers in the same direction, the fibers would provide a reduced resistance to cracking and tensile forces in the other directions. Further investigation of the behavior of fibers during printing is necessary to confirm these results as fiber reinforcement may not be an adequate method of reinforcing printable concrete due to their tendency to orient in one direction during printing.

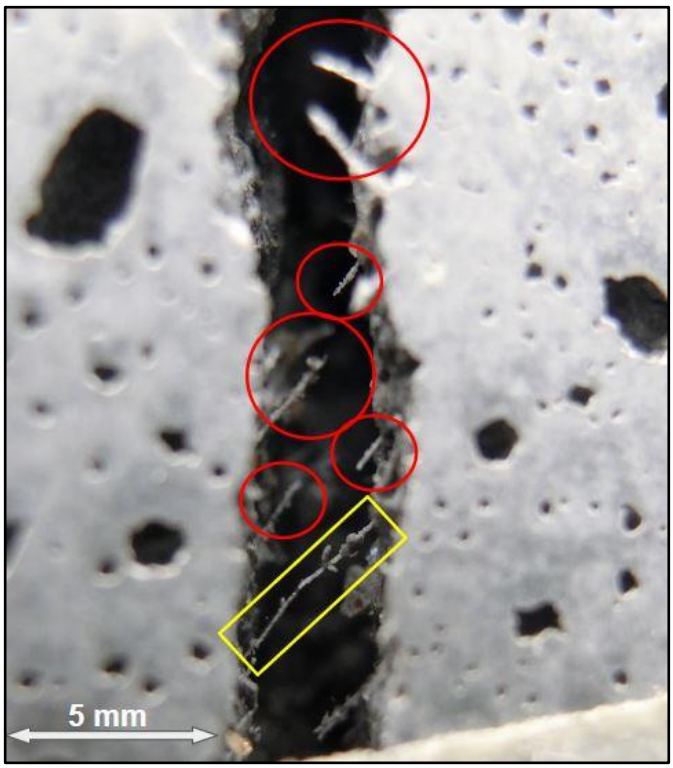

Figure 46: Macroscopic image of fibers across a crack in the Acti-Gel 0.8% compression specimen. Only one fiber can be seen bridging the crack while a majority are fractured suggesting the fiber content of 0.25% by total volume may be insufficient to resist cracking.

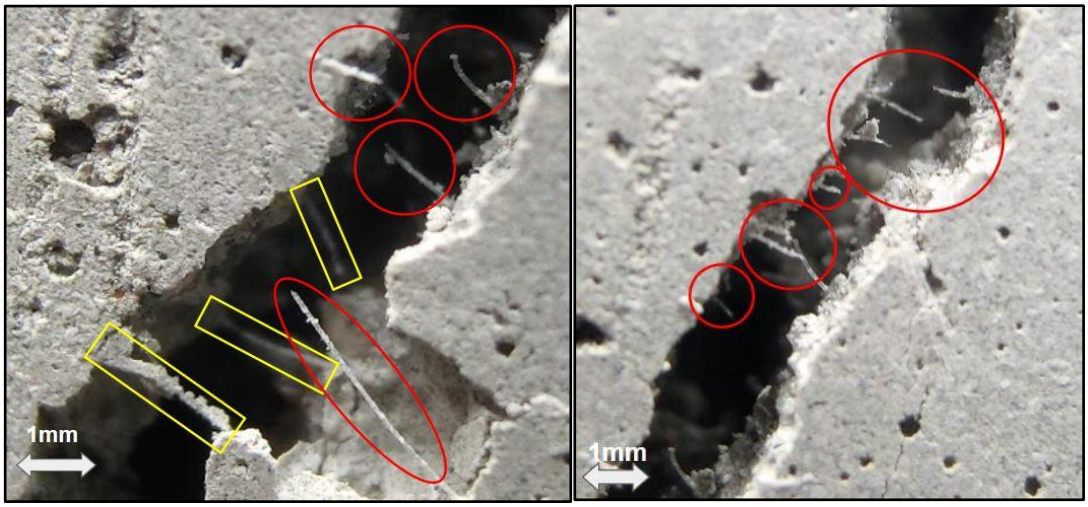

Figure 47: Macroscopic images of fibers across a crack in the PAM 0.6% specimen. Again, fibers are seen to be mostly fractured across the crack. However, the images confirm that the mixing procedures outlined in Appendix A are sufficient to ensure even distribution and random orientation of fibers in the samples.

Figure 48: Macroscopic image of the surface of a printed layer showing fibers at the layer surface oriented longitudinally along the length of the layer.

Figure 49: Macroscopic image of the end of a printed layer showing interior fibers also orientated longitudinally along the length of the layer. This consistent fiber orientation could result in reduced shrinkage and cracking resistance perpendicular to the length of the layer.

4.2.6. Scanning electron microscopy

The microscopic investigation of the layer interface completed on PVA mix design, B690SP1.2PVA0.25, and PAM mix design, B571.2SP1.6PAM0.9, revealed the benefit of PAM for interlayer bonding and homogeneity. Figure 50 depicts a section of the interface for the mix design without PAM. Hydrated cement grains can be seen on both sides of the interface, but even where the layers are extremely close, hydration appears to have occurred independently within each layer substrate. As illustrated on the figure, there are few instances where bonding appears to have occurred across the interface between layers. A majority of the interface is clearly distinguished displaying little evidence of chemical or mechanical bonding.

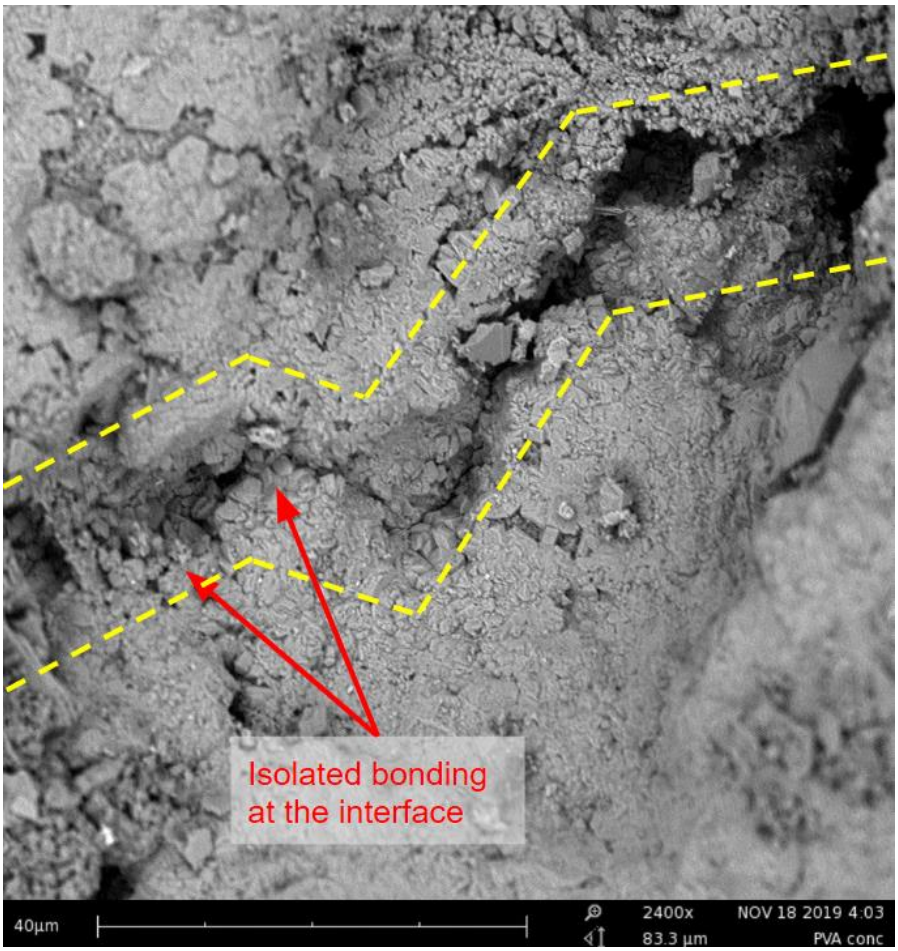

Figure 50: SEM image showing a section of the PVA interface with the interfacial region outlined by the dashed yellow lines. This image shows distinct hydration occurring within each layer substrate with isolated bonding across the interface. The lack of hydration across the interface results in a weak interlayer bond.

Figure 51 gives a perspective at another section of the interface for the PVA mix design. This image clearly displays the issue of interlayer bonding. A sizable portion of the interface in the PVA sample showed the two layers making no contact. In this image, the surface of each layer is smooth with no signs of interfacial bonding. Figure 52 shows another type of microstructure commonly seen at the interface: air voids. Although not continuous like the obvious gap in Fig. 51, these isolated air voids are detrimental to the interfacial strength. The tips of these voids are sites for crack propagation along the interface as they are locations for stress concentrations. Voids such as these, with nothing bonding the layers together, are unable to resist loading at the interface. These images illustrate why the interface is a weak point in printed structures and the need for some sort of matrix capable of bridging the interface.

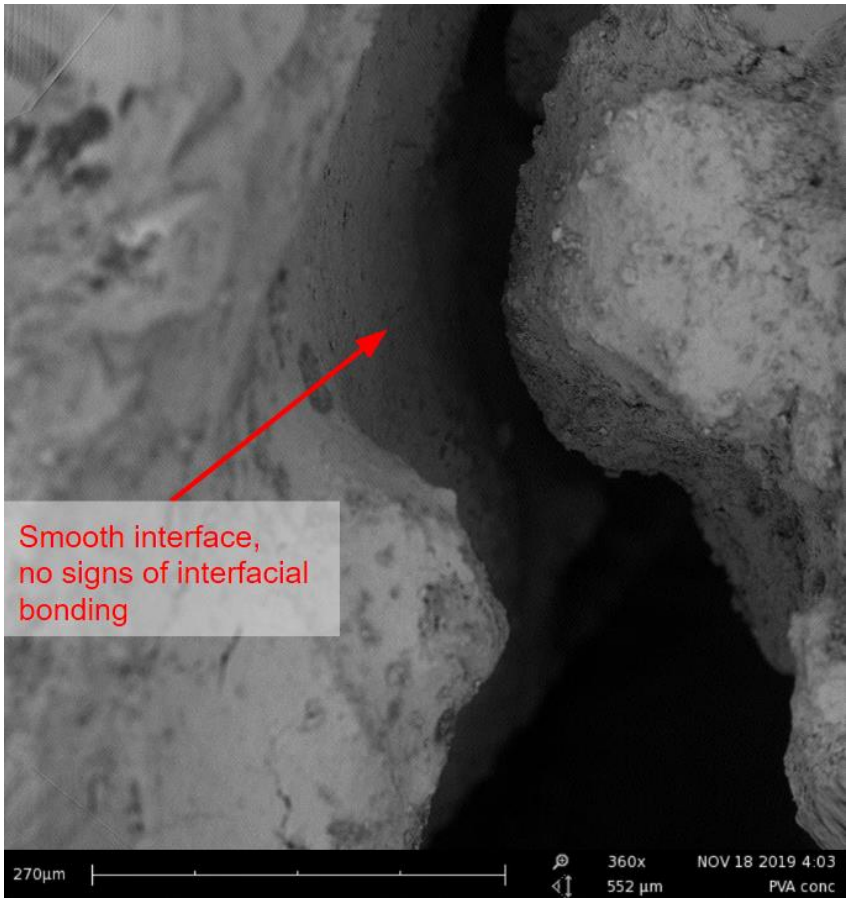

Figure 51: SEM image showing a large gap at the PVA interface with no signs of interfacial bonding. These types of gaps were common for the PVA interface and illustrate the issue of interlayer bonding.

Figure 52: SEM image showing air voids at the PVA interface. These voids are sites for crack propagation along the interface as the tips are locations of stress concentrations.

The SEM investigation of the layers including PAM showed the polymer's behavior both at the interface and within the substrate. Figure 53 gives an overview of the interface outlined in yellow. The interface itself is similar to that of the PVA sample, but notable in this image is the network structure of PAM which is interwoven throughout the substrate creating a 3D matrix of PAM throughout each layer.

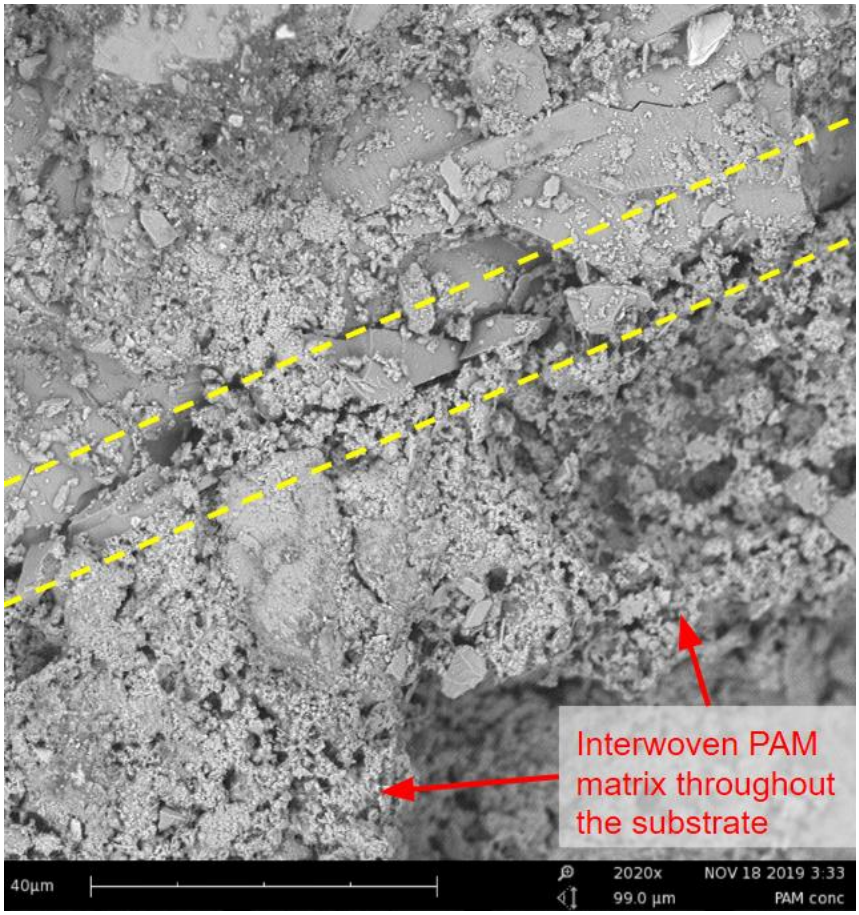

Figure 53: SEM image showing a section of the PAM interface. PAM is seen not only bridging across the interface of the two layers but interwoven throughout the rest of the layer substrates.

A closer look at the interface reveals the real advantage of using PAM in printable concrete. Figures 54 and 55 display how the PAM network bridges between cement and sand grains at the interface bonding the two layers together. The web-like structure spans the interfacial gaps which otherwise have nothing bonding the layers together as was the case with the PVA interface. Additionally, the ability of PAM to anchor itself to sand and cement grains can be seen in both images. This is crucial for the interlayer bond strength on a microscopic level as it seems the interwoven PAM matrix is able to achieve composite behavior with the hydrated cement structure. As opposed to other forms of reinforcement such as fibers or rebar which rely solely on mechanical bonds to adhere them to the cement structure, PAM seems to be able to chemically bond with cement and sand grains. This SEM investigation indicates that PAM provides resistance to shear and tensile forces by bridging the interface and anchoring to the hydrated structure within the layer substrates. This confirms that PAM improves interlayer bonding and further reinforces PAM as the ideal VMA for printable concrete.

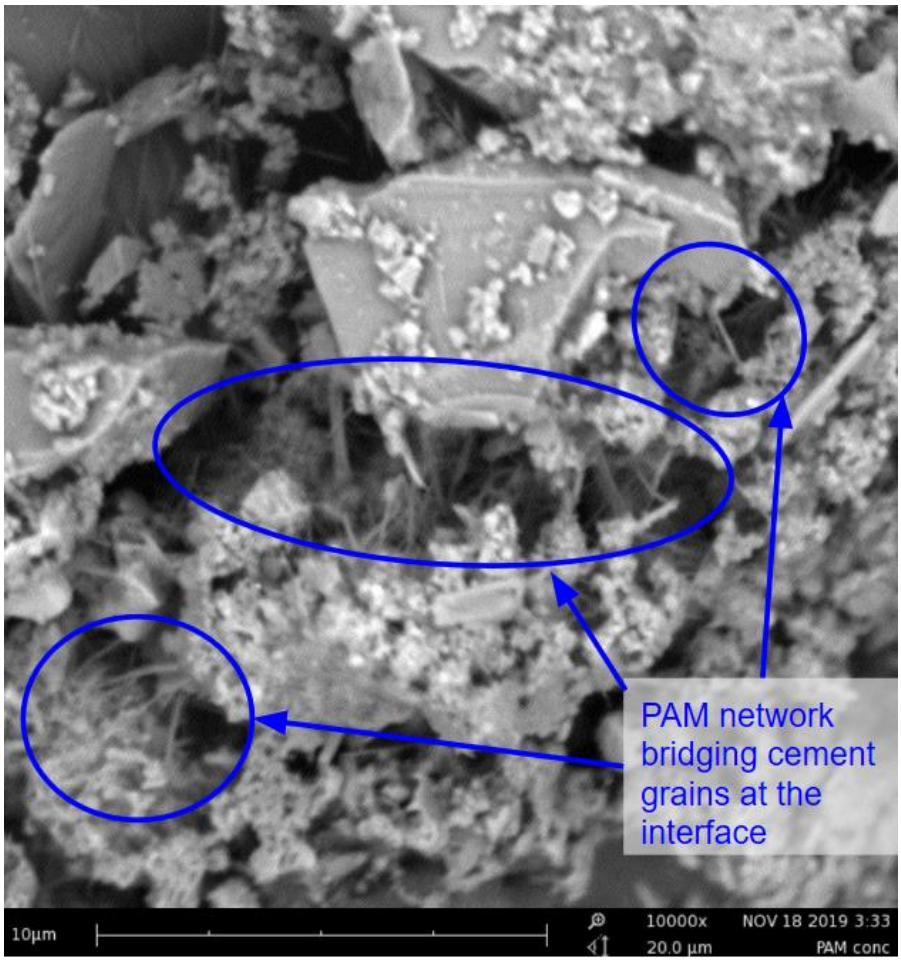

Figure 54: SEM image showing PAM matrix bridging cement grains at the interface. This bridging, combined with PAM's ability to anchor to cement and sand grains, demonstrates that PAM is able to achieve composite behavior with the hydrated cement structure.

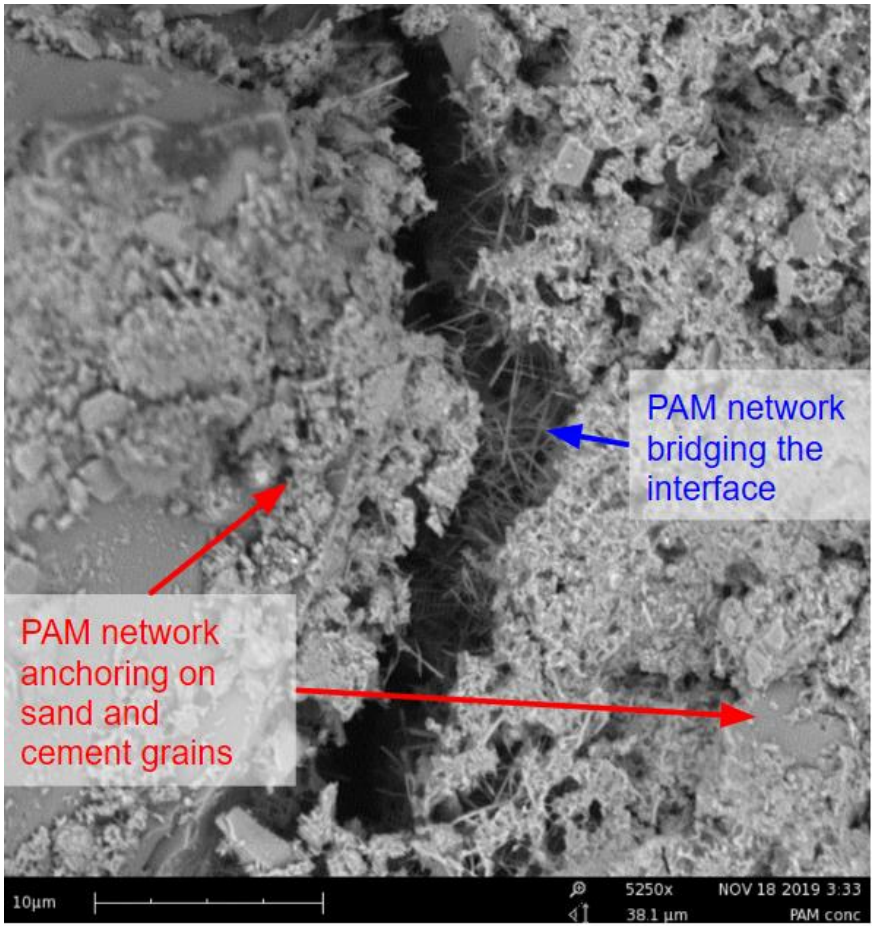

Figure 55: SEM image showing the PAM bridging the interface. The web-like matrix of PAM connects the two layers and improves interlayer bonding and homogeneity by providing resistance to stresses at the interface.

4.2.7. Discussion of optimal mix design

The aim of the experimentation and testing with different mix designs was to determine a particular mix design or admixture which would be ideal for printable concrete. After the investigation and results for pumpability, extrudability, buildability, viscometry, and material properties, it can be concluded that PAM 0.9% is the optimal mix design out of those considered in this report. This mix design displayed outstanding extrudability despite the inconsistencies present during extrusion tests with the prototype extruder. Further, this mix design also displayed the largest shear-thinning which allowed for easy pumping and lower slump values during the buildability test than the Acti-Gel mixes despite their high structuration rate. The real differentiator for the PAM 0.9%, as well as for PAM 0.6%, was the cohesiveness induced by PAM in the fresh mix. PAM 0.9% held together so well that it displayed a high initial yield stress of 1146 Pa (0.17 psi) indicating that it would be difficult to pump while also demonstrating that it was the easiest mixture to extrude through the nozzle. The thixotropic properties of PAM 0.9% allow this mix to satisfy the contrary rheological requirements of printable concrete: being liquid enough to flow through a delivery system and, immediately after being extruded, having sufficient green strength to hold its own weight without significant deformation. PAM acts as a

flocculant developing green strength, but also, its reaction with the PVA hydroxyl groups further accelerates flocculation and the onset of early hydration which are responsible for initial structuration. Additionally, SEM revealed PAM's ability to improve the bond between layers by both bridging the interface and displaying composite behavior with the cement structure. It is believed from this research that PAM is a promising additive for use in printable concretes, especially due to the small doses required to drastically change the fresh-state behavior of concrete, and deserves further research.

4.2.7.1 Cost analysis of polyacrylamide for construction applications

To address the economic impact of using PAM as a VMA for printable concrete, the mix proportions for PAM 0.9% were scaled to a cubic yard in order to approximate the material cost for this mix design on a construction scale. The quantities and estimated prices per cubic yard of raw materials are listed below in Table 11. For reference, these proportions yielded approximately 950 lbs of cementitious materials per cubic yard. Excluding the addition of PAM, the cost is roughly $93.35 per cubic yard which is typical for commercial concrete prices. The addition of 0.9% PAM by weight of binder at the rate of $0.50 per pound increases this price to $97.68 per cubic yard. This 4.4% increase in price due to PAM may seem steep, especially on larger projects. However, its contribution to 3D printing has the potential to create huge savings on labor and formwork depending on the complexity of the project. Cost associated with formwork can account for anywhere from a quarter to half of the total cost of concrete construction (De Schutter et al., 2018), so a 4.4% increase to possibly obtain 25%-50% savings is worth the initial investment. The cost associated with 3D printing must also be considered, but as the technology advances, this method will become both more economical and more sustainable than traditional concrete construction.

Table 11: Cost analysis for one cubic yard of mix design PAM 0.9% to estimate economic impact of using PAM on a construction scale.

Material	**Quantity (lbs/yd^3)**	**Unit Price ($/lb)**	**Total Cost ($/yd^3)**
Cement	866.7	$ 0.04	$ 32.50
Silica Fume	96.0	$ 0.30	$ 28.82
Fine Sand	1937.7	$ 0.01	$ 19.38
Superplasticizer	15.3	$ 0.07	$ 1.00
PVA Fibers	5.4	$ 2.14	$ 11.65
Polyacrylamide	8.7	$ 0.50	$ 4.33
		Total	$ 97.68

4.3. Brazilian disk test

The Brazilian disk test showed the performance of the adhesive and sinusoidal geometries on the interlayer bond strength of printable concrete in comparison to a flat interface. After all specimens were tested, peak load and fracture toughness were tabulated for each sample. All tables can be located in Appendix L. For this report, the samples are labeled by their amplitude first and then frequency with A, B, C correlating to frequencies $\pi/4$, $\pi/6$, and $\pi/12$, respectively. Figure 56 shows test sample 1A after its failure in Mode I. The test set up at Mode I had a load angle of zero degrees, and as such the interface was loaded in tension. This can be seen in Fig. 56 as the sample split at the interface leaving the sinusoidal pattern intact on each half. The test set up at Mode II had a load angle of 25 degrees. It can be seen in Fig. 57 that the test samples for 25 degrees broke in shear as indicated by the shearing of the waves down the middle of the sample.

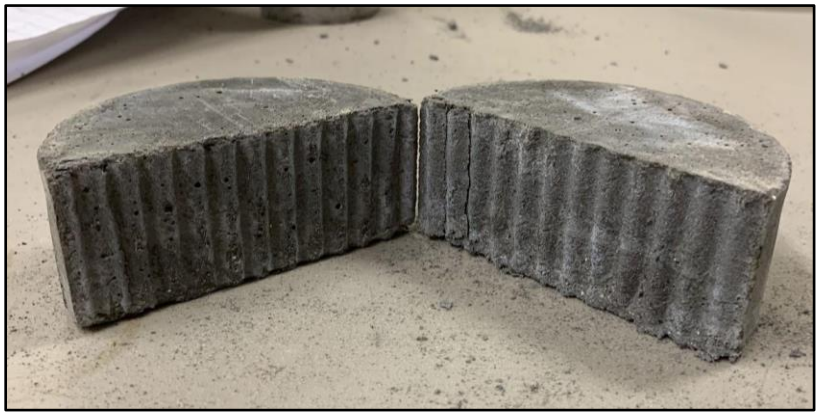

Figure 56: Interface of sample 1A from Brazilian disk test (Mode I), splitting perfectly along the interface in tension. Sample 1A had the highest peak load of Mode I fracture at 5,489 lbs.

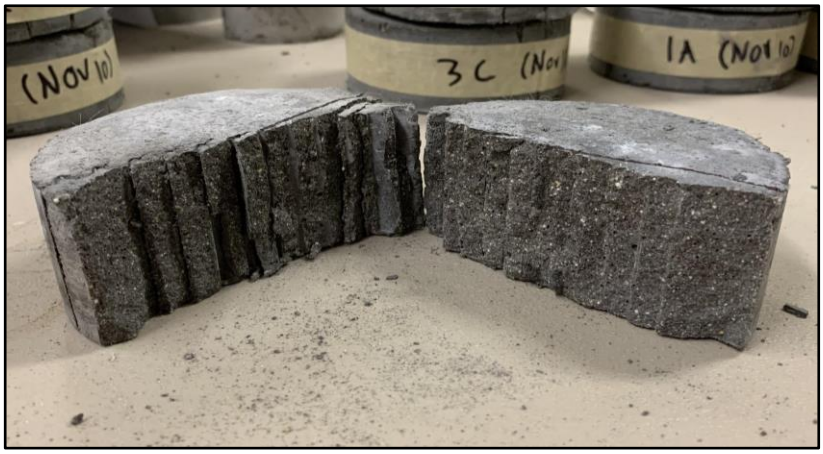

Figure 57: Interface of sample 3A from Brazilian disk test (Mode II). The sinusoidal pattern in Sample 3A displayed ideal Mode II fracture, with the sinusoidal peaks shearing along the interfacial axis.

Within Mode I testing, sample 1A yielded the highest peak load of the sinusoidal patterns at 5,489 lbs. Within Mode II testing, sample 3C yielded the highest peak load of the sinusoidal patterns at 7,406 lbs. Sample 3C, shown in Fig. 58, showed an increased resistance to shear at the 25-degree load angle. Unlike all other samples at the 25-degree loading angle, 3C showed signs of Mode I failure. The crack propagated along the load axis, then continued along the sinusoidal pattern after intersecting with the interface. This showed the ability of 3C in shear to essentially create a homogenous sample as the crack propagated through the portion of solid concrete, rather than at the interface. From the tables in Appendix L, the data showed that geometric interlocking with sinusoidal patterns tends to improve the interlayer shear strength. The average of all the sinusoidal waves in shear gave a mean of 3,849 lbs for max load, which is higher than the flat interface average of 3,325 lbs in shear. One area to note from the tables is that the adhesive decreased the shear strength, breaking at loads of 1,619 lbs and 942 lbs. However, in tension, the adhesive resulted in a consistent strength of around 4,000 lbs, while the flat interface without adhesive was inconsistent with peak loading at both 2,311 lbs and 6,261 lbs. Due to this consistent strength in tension, the adhesive could benefit the interlayer bond but further testing would need to be completed to determine the strength of the flat interface samples as insufficient data was collected to make specific conclusions. Fracture toughness for Modes I and II were plotted against the ratio of amplitude to wavelength (A/λ) to investigate the scalability of the sinusoidal geometries by ratio of amplitude to wavelength (Fig. 59 and Fig. 60).

Figure 58: Top view of 3C after breaking at a 25-degree load angle. Within Mode II fracture, sample 3C broke at the highest load of 7,406 lbs. Sample 3C created an essentially homogeneous interface in shear as the sample broke initially in tension through the solid portion of the sample, then sheared once the crack met with the interface.

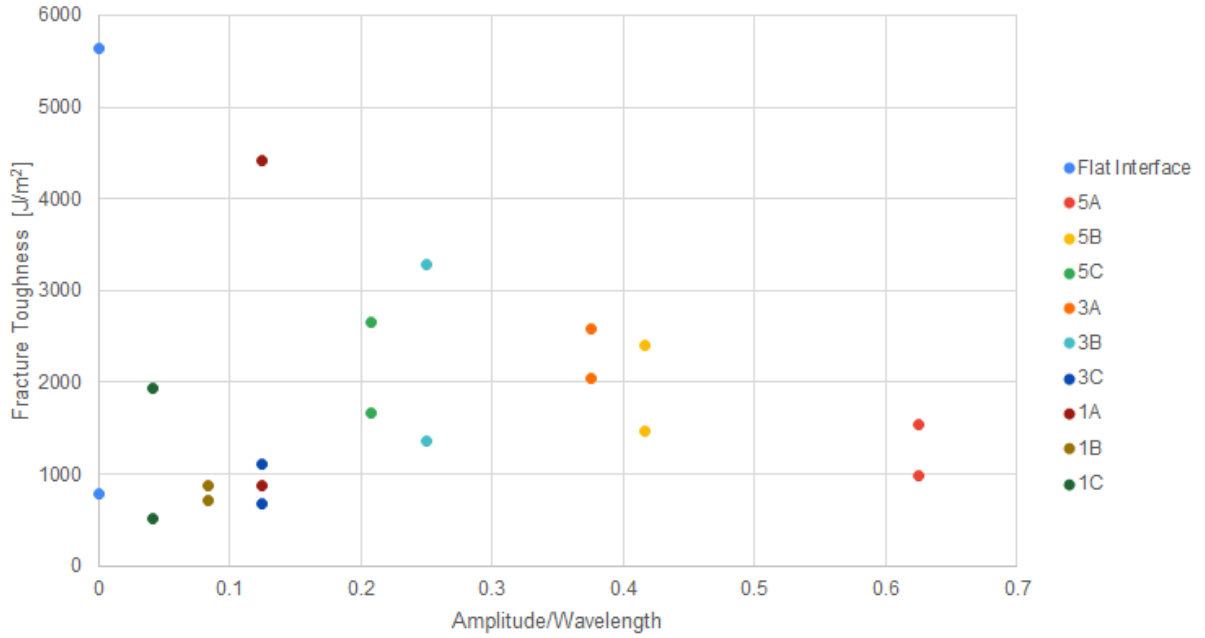

Figure 59: A graph of fracture toughness by the ratio of amplitude to wavelength (A/λ) for Mode I. The graph suggests that there is a higher fracture toughness for samples with an A/λ ratio between 0.2 and 0.4, disregarding outliers.

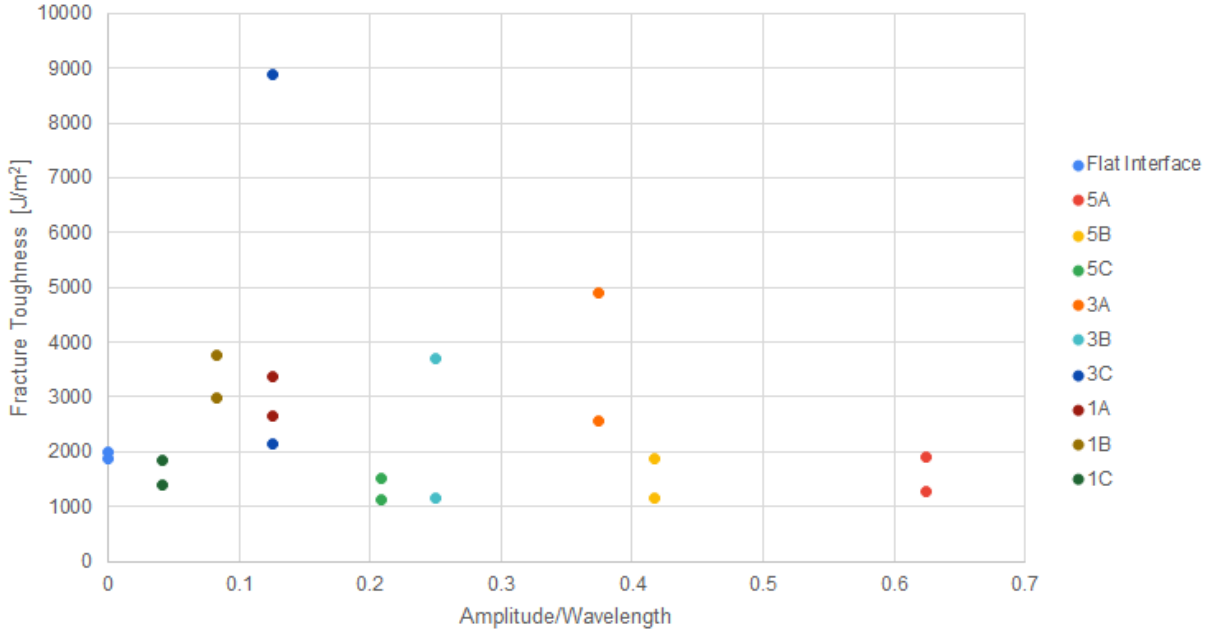

Figure 60: A graph of fracture toughness by the ratio of amplitude to wavelength (A/λ) for Mode II. The graph suggests a peak fracture toughness for shear around an A/λ ratio of 0.1, however more data must be collected to confirm trends and conclusions.

In the graph for Mode I, shown in Fig. 59, the flat interface control sample dataset (A/λ=0) is an outlier. Due to a large difference in fracture toughness between the two tests, the baseline in terms of fracture toughness is unclear. Neglecting outliers, the data suggests that

the toughness in Mode I is generally higher for the samples with an A/λ ratio ranging from 0.2 to 0.4. It should be noted that samples 1A and 3C which both have an A/λ ratio of 0.125 have a significant difference in fracture toughness. This result demonstrates that the sinusoidal patterns are most likely not scalable by amplitude and wavelength. The plot for Mode II in Fig. 60 suggests a peak shear performance around the A/λ ratio of 0.1, but as with the Mode I plot, there is not a clear trend in the data, and therefore more data should be collected to draw definite conclusions. From this graph, it can be concluded that geometries 1C, 5A, 5B, and 5C all have a Mode II fracture toughness less than the flat interface control. 1C has the least roughness which is why this sample showed no increase in shear strength. The data signifies a limit to the height of the sinusoidal waves as all samples with an amplitude of 5 mm were weaker than the control, and the waves sheared off at failure. The data from the Brazilian disk test was variable as can be expected with a brittle material such as concrete. Some variability may be due to the creation of the samples. It was observed that some of the samples did not fully achieve the sinusoidal shape of the insert resulting in voids at certain portions along the interface. The applicability of using geometric interlocking on a construction scale may be limited unless high enough printer precision can ensure that the layers make sufficient contact with each other. Again, more samples should be tested for each shape to get an accurate picture of the behavior of each interlocking pattern in both Mode I and Mode II.

5. Conclusions and recommendations

The first objective of the research discussed in this report was to investigate two VMAs, Acti-Gel and polyacrylamide, for use in printable concrete. This involved experimentation with different mix designs including cement, silica fume, fine aggregate, superplasticizer, PVA fibers, and water. The experimentation resulted in mix designs with approximately a 1:2 ratio of binder to sand. Based on an investigation of pumpability, extrudability, buildability, viscosity, compressive strength, and microscopic structure, it was determined that PAM is the ideal VMA for printable concrete for a number of reasons:

- The inclusion of PAM promotes a high initial yield stress compared to Acti-Gel, which results in optimal shape stability, as seen in the printed filaments.
- PAM significantly increases the cohesiveness of concrete, which enhances the ability of the mix to produce a smooth, continuous layer with good surface quality.
- PAM induces shear-thinning allowing for ease of pumping despite the high initial yield stress and cohesiveness. This property allows for PAM mix designs to achieve all three rheological requirements of printable concrete (pumpability, extrudability, and buildability) at the desired stages in the printing process.
- PAM increases the ductility of cured concrete which is beneficial for structural purposes, as brittle failure is sudden and therefore much more difficult to predict. Additionally, using PAM in the concrete mix has no significant reduction to the compressive strength of the concrete.
- On a microscopic level, the web-like network of PAM achieves composite behavior with the hydrated C-S-H structure of concrete and bridges the interface between layers, thus providing increased interlayer bond strength.

- On a construction scale, the addition of PAM in concrete results in a 4.4% increase in material cost. However, the potential savings enabled by 3D printing concrete with PAM could offset this added cost.

Further research should be completed to confirm the applicability of PAM for printing. A few areas requiring investigation arose over the course of this research. The variability of PAM could be an obstacle in mixing on a construction scale, and further experimentation to determine the best mixing procedure for PAM should be completed. Additionally, the long-term effects of PAM on the cured concrete were not considered in this project, and it should be confirmed that PAM does not negatively affect the long-term strength and durability of the concrete. Finally, the SEM imaging and other research indicates that PAM increases the interlayer bond, but the optimal PAM content for interlayer bonding as well as the specific increase in bond strength for printed layers including PAM should be determined.

As a second objective, this project tested the improvement to interlayer bonding for nine different sinusoidal layer geometries, as well as for a common concrete bonding adhesive. The data was sporadic for the nine sinusoidal samples indicating the difficulties in creating perfect contact between the layers with the added geometry. This finding would most likely be amplified if the nozzle geometry was implemented for construction applications, however the sample size used was not large enough to make any substantial conclusions as to whether or not geometric interlocking could provide enhanced bond strength at the layer interface. The results should also be verified by printing layers with the chosen geometry as inaccuracies with printing could reduce any added benefit from geometric interlocking. It was determined that the commonly available Quikrete Bonding Adhesive provided consistent strength in tension, as expected, but showed no benefit in shear. Because the sinusoidal wave geometry improved shear strength between layers, and the bonding adhesive improved tensile strength between layers, these two different methods should be used in combination.

6. References

References

Active Minerals International. (2017). Acti-gel® 208. Retrieved from https://acti-gel.com/acti-gel/

Belhadj, E., Diliberto, C., & Lecomte, A. (2012). *Characterization and activation of basic oxygen furnace slag* doi://doi.org/10.1016/j.cemconcomp.2011.08.012

Belous, N., Koshevar, V., & Rodtsevich, S. (2009). Composite retardants of hydrophobic-structuring type and their effect on properties of plasticized concretes. *Russian Journal of Applied Chemistry, 82*(9), 1669-1674. doi:10.1134/S1070427209090286

Bessaies-Bey, H., Baumann, R., Schmitz, M., Radler, M., & Roussel, N. (2015). *Effect of polyacrylamide on rheology of fresh cement pastes* doi://doi.org/10.1016/j.cemconres.2015.05.012

Brookfield Ametek. (2015). *More solutions to sticky problems: A guide to getting more from your brookfield viscometer & rheometer*. Middleboro, MA:

Buswell, R. A., Leal, d. S., Jones, S. Z., & Dirrenberger, J. (2018). 3D printing using concrete extrusion: A roadmap for research. *Cement and Concrete Research; SI : Digital Concrete 2018, 112*, 37-49. doi://doi.org/10.1016/j.cemconres.2018.05.006

Carvalho, S. Z., Vernilli, F., Almeida, B., Demarco, M., & Silva, S. N. (2017). *The recycling effect of BOF slag in the portland cement properties* doi://doi.org/10.1016/j.resconrec.2017.08.021

Chan, N., Young-Rojanschi, C., & Li, S. (2018). Effect of water-to-cement ratio and curing method on the strength, shrinkage and slump of the biosand filter concrete body. *Water Science and Technology, 77*(6), 1744-1750. doi:10.2166/wst.2018.063

CHINAFLOC. (2014). Polyacrylamide in cement concrete modification. Retrieved from http://www.chinafloc.com/Polyacrylamide-in-Cement-Concrete-Modification_936.html

COBOD International. (2019). Modular 3D construction printers - 3D printed buildings. Retrieved from https://cobod.com/

Concrete bonding adhesive. (2018). Retrieved from https://quikrete.com/productlines/concretebondingadhesive.asp

Contour Crafting Corporation. (2017). Building construction. Retrieved from http://contourcrafting.com/building-construction/

Craveiro, F., Duarte, J., Bártolo, H., & Bártolo, P. (2019). Additive manufacturing as an enabling technology for digital construction: A perspective on construction 4.0. *Automation in Construction, 103*, 251-267. doi:10.1016/j.autcon.2019.03.011

De Schutter, G., Lesage, K., Mechtcherine, V., Nerella, V. N., Habert, G., & Agusti-Juan, I. (2018). Vision of 3D printing with concrete — technical, economic and environmental potentials. *Cement and Concrete Research; SI : Digital Concrete 2018, 112*, 25-36. doi://doi.org/10.1016/j.cemconres.2018.06.001

Draijer, W. M. (2007). *Assessing the pumpability of concrete with the slump and pressure bleeding test*

Ebnesajjad, S. (2006). 4 - surface and material characterization techniques. In S. Ebnesajjad (Ed.), *Surface treatment of materials for adhesion bonding* (pp. 43-75). Norwich, NY: William Andrew Publishing. doi:https://doi.org/10.1016/B978-081551523-4.50006-7 Retrieved from http://www.sciencedirect.com/science/article/pii/B9780815515234500067

Flatt, R., & Schober, I. (2012). In Roussel N. (Ed.), *7 - superplasticizers and the rheology of concrete* Woodhead Publishing. doi://doi-org.ezproxy.wpi.edu/10.1533/9780857095282.2.144

Goldstein, J. I., Newbury, D. E., Michael, J. R., Ritchie, N. W. M., Scott, J. H. J., & Joy, D. C. (2017). *Scanning electron microscopy and X-ray microanalysis* (4th ed. 2018 ed.). New York, NY: Springer. doi:10.1007/978-1-4939-6676-9 Retrieved from https://ebookcentral.proquest.com/lib/[SITE_ID]/detail.action?docID=5591777

He, W., Chen, K., Zhang, B., & Dong, K. (2018). Improving measurement accuracy of brazilian tensile strength of rock by digital image correlation. *Review of Scientific Instruments, 89*(11) Retrieved from https://doi.org/10.1063/1.5065541

Huang, Y., Liu, C., & Stout, M. G. (1996). A brazilian disk for measuring fracture toughness of orthotropic materials. *Acta Materialia, 44*(3), 1223-1232. doi:10.1016/1359-6454(95)00229-4

Jewett, J. L., & Carstensen, J. V. (2019). Topology-optimized design, construction and experimental evaluation of concrete beams. *Automation in Construction, 102*, 59-67. doi://doi.org/10.1016/j.autcon.2019.02.001

Jiao, D., El Cheikh, K., Shi, C., Lesage, K., & De Schutter, G. (2019). Structural build-up of cementitious paste with nano-Fe3O4 under time-varying magnetic fields. *Cement and Concrete Research, 124*,

105857. doi://doi.org/10.1016/j.cemconres.2019.105857

Juenger, M. C. G., Winnefeld, F., Provis, J. L., & Ideker, J. H. (2011). Advances in alternative cementitious binders. *Cement and Concrete Research; Conferences Special: Cement Hydration Kinetics and Modeling, Quebec City, 2009 & CONMOD10, Lausanne, 2010, 41*(12), 1232-1243. doi://doi.org/10.1016/j.cemconres.2010.11.012

Kaci, A., Chaouche, M., & Andréani, P. (2011). *Influence of bentonite clay on the rheological behaviour of fresh mortars* doi://doi.org/10.1016/j.cemconres.2011.01.002

Kazemian, A., Yuan, X., Cochran, E., & Khoshnevis, B. (2017). *Cementitious materials for construction-scale 3D printing: Laboratory testing of fresh printing mixture* doi://doi.org/10.1016/j.conbuildmat.2017.04.015

Keita, E., Bessaies-Bey, H., Zuo, W., Belin, P., & Roussel, N. (2019). Weak bond strength between successive layers in extrusion-based additive manufacturing: Measurement and physical origin. *Cement and Concrete Research, 123*, 105787. doi://doi.org/10.1016/j.cemconres.2019.105787

Khoshnevis, B. (2004). Automated construction by contour crafting—related robotics and information technologies. *Automation in Construction; the Best of ISARC 2002, 13*(1), 5-19. doi://doi.org/10.1016/j.autcon.2003.08.012

Labonnote, N., & Rüther, P. (2016). *Additive manufacturing: An opportunity for functional and sustainable constructions* doi:10.1201/9781315198101-41

Le, T. T., Austin, S. A., Lim, S., Buswell, R. A., Gibb, A. G. F., & Thorpe, T. (2012). Mix design and fresh properties for high-performance printing concrete. *Materials and Structures, 45*(8), 1221-1232. doi:10.1617/s11527-012-9828-z

Marchment, T., Sanjayan, J., & Xia, M. (2019). Method of enhancing interlayer bond strength in construction scale 3D printing with mortar by effective bond area amplification. *Materials & Design, 169*, 107684. doi://doi.org/10.1016/j.matdes.2019.107684

Marchon, D., Kawashima, S., Bessaies-Bey, H., Mantellato, S., & Ng, S. (2018). Hydration and rheology control of concrete for digital fabrication: Potential admixtures and cement chemistry. *Cement and Concrete Research; SI : Digital Concrete 2018, 112*, 96-110. doi://doi.org/10.1016/j.cemconres.2018.05.014

Markides, C. F., Pasiou, E. D., & Kourkoulis, S. K. (2015). The bi-material circular disc compressed between the jaws of the ISRM standardized apparatus for the brazilian test. *Clinical Microbiology Newsletter, 37*(4), 33. doi:10.1016/j.clinmicnews.2015.01.008

Martins, J. P., Ferreira, M. P. A., Ezazi, N. Z., Hirvonen, J. T., Santos, H. A., Thrivikraman, G., . . . Bertassoni, L. E. (2018). In Uskoković V., Uskoković D. P.(Eds.), *Chapter 4 - 3D printing: Prospects and challenges* Elsevier. doi://doi.org/10.1016/B978-0-323-48063-5.00004-6

NANOIMAGES. (2017). SEM technology overview – scanning electron microscopy. Retrieved from https://www.nanoimages.com/sem-technology-overview/?msclkid=5c6a23b4683917d0fb2d7e76a0275ab5&utm_source=bing&utm_medium=cpc&utm_campaign=**LP%20DSA%20-%20Categories&utm_term=technology&utm_content=Technology

Narayanan, S. P., & Sirajuddin, M. (n.d.). Properties of brick masonry for FE modeling. *American Journal of Engineering Research, 1*

Nerella, V. N., Hempel, S., & Mechtcherine, V. (2019). Effects of layer-interface properties on mechanical performance of concrete elements produced by extrusion-based 3D-printing. *Construction and Building Materials, 205*, 586-601. doi://doi.org/10.1016/j.conbuildmat.2019.01.235

Nicoleau, L., Schreiner, E., & Nonat, A. (2014). *Ion-specific effects influencing the dissolution of tricalcium silicate* doi://doi.org/10.1016/j.cemconres.2014.02.006

Noushini, A., Samali, B., & Vessalas, K. (2013). *Effect of polyvinyl alcohol (PVA) fibre on dynamic and material properties of fibre reinforced concrete* doi://doi.org/10.1016/j.conbuildmat.2013.08.035

Omidi, M., Fatehinya, A., Farahani, M., Akbari, Z., Shahmoradi, S., Yazdian, F., . . . Vashaee, D. (2017). 7 - characterization of biomaterials. In L. Tayebi, & K. Moharamzadeh (Eds.), *Biomaterials for oral and dental tissue engineering* (pp. 97-115) Woodhead Publishing. doi:https://doi.org/10.1016/B978-0-08-100961-1.00007-4 Retrieved from http://www.sciencedirect.com/science/article/pii/B9780081009611000074

Pailyn, T., Watcharapong, W., & Arnon, C. (2014). Hydration and compressive strength of blended cement containing fly ash and limestone as cement replacement. *Journal of Materials in Civil Engineering, 26*(12), 04014088. doi:10.1061/(ASCE)MT.1943-5533.0001002

Rahbar, N., Jorjani, M., Riccardelli, C., Wheeler, G., Yakub, I., Tan, T., & Soboyejo, W. O. (2010). Mixed

mode fracture of marble/adhesive interfaces. *Materials Science and Engineering: A, 527*(18), 4939-4946. doi:https://doi.org/10.1016/j.msea.2010.04.029

Rahbar, N., Yang, Y., & Soboyejo, W. (2008). Mixed mode fracture of dental interfaces. *Materials Science and Engineering: A, 488*(1), 381-388. doi:https://doi.org/10.1016/j.msea.2007.11.038

Ramachandran, V. S. (n.d.). 7.1 introduction. *Concrete admixtures handbook - properties, science, and technology (2nd edition)* () William Andrew Publishing/Noyes. Retrieved from https://app.knovel.com/hotlink/pdf/id:kt00538EI2/concrete-admixtures-handbook/superplasticizers-introduction

Reiter, L., Wangler, T., Roussel, N., & Flatt, R. J. (2018). The role of early age structural build-up in digital fabrication with concrete. *Cement and Concrete Research; SI : Digital Concrete 2018, 112*, 86-95. doi://doi.org/10.1016/j.cemconres.2018.05.011

Rodríguez, E. D., Bernal, S. A., Provis, J. L., Payá Jordi, Monzó José, M., & Borrachero María Victoria. (2012). Structure of portland cement pastes blended with sonicated silica fume. *Journal of Materials in Civil Engineering, 24*(10), 1295-1304. doi:10.1061/(ASCE)MT.1943-5533.0000502

Roussel, N. (2018). Rheological requirements for printable concretes. *Cement and Concrete Research; SI : Digital Concrete 2018, 112*, 76-85. doi://doi.org/10.1016/j.cemconres.2018.04.005

Sanjayan, J. G., Nematollahi, B., Xia, M., & Marchment, T. (2018). Effect of surface moisture on inter-layer strength of 3D printed concrete. *Construction and Building Materials, 172*, 468-475. doi://doi.org/10.1016/j.conbuildmat.2018.03.232

Seraderian, R. (2019). In Prestressed Concrete Class (Ed.), *Prestressed and precast concrete
*

Shi, C., Jiménez, A. F., & Palomo, A. (2011). New cements for the 21st century: The pursuit of an alternative to portland cement. *Cement and Concrete Research; Special Issue: 13th International Congress on the Chemistry of Cement, 41*(7), 750-763. doi://doi.org/10.1016/j.cemconres.2011.03.016

Sikora, P., Horszczaruk, E., Cendrowski, K., & Mijowska, E. (2016). The influence of nano-Fe3O4 on the microstructure and mechanical properties of cementitious composites. *Nanoscale Research Letters, 11* doi:10.1186/s11671-016-1401-1

Sun, Z., & Xu, Q. (2008). Micromechanical analysis of polyacrylamide-modified concrete for improving strengths. *Materials Science and Engineering: A, 490*(1), 181-192.

doi://doi.org/10.1016/j.msea.2008.01.026

Taylor, H. F. (1990). *Cement chemistry*. London u.a: Acad. Press.

Thomas, N. L., & Birchall, J. D. (1983). *The retarding action of sugars on cement hydration* doi://doi.org/10.1016/0008-8846(83)90084-4

Tolinski, M. (2009). In Tolinski M. (Ed.), *Chapter 7 - overview of fillers and fibers*. Oxford: William Andrew Publishing. doi://doi.org/10.1016/B978-0-8155-2051-1.00007-8

Total Kustom. (n.d.). 3D concrete printers. Retrieved from http://www.totalkustom.com/3d-concrete-printers.html

University of Illinois. (n.d.). Scientific principles. Retrieved from http://matse1.matse.illinois.edu/concrete/prin.html

Verian, K., Carli, M., Bright, R., & Maandi, E. (2018). *Research development in 3DCP: Cured-on-demand with adhesion enhancement delivery system* doi:10.13140/RG.2.2.26245.60641

Wallevik, J. E. (2006). Relationship between the bingham parameters and slump. *Cement and Concrete Research, 36*(7), 1214-1221. doi://doi.org/10.1016/j.cemconres.2006.03.001

Wangler, T. (Nov 11, 2018). Digital concrete processing: A review. Paper presented at the *1st International Conference on 3D Construction Printing,*

Wangler, T., Lloret, E., Reiter, L., Hack, N., Gramazio, F., Kohler, M., . . . Flatt, R. (2016). Digital concrete: Opportunities and challenges. *RILEM Technical Letters, 1*, 67. doi:10.21809/rilemtechlett.2016.16

Wangler, T., Roussel, N., Bos, F. P., Salet, T. A. M., & Flatt, R. J. (2019). *Digital concrete: A review* doi://doi.org/10.1016/j.cemconres.2019.105780

Winnefeld, F., & Lothenbach, B. (2010). Hydration of calcium sulfoaluminate cements — experimental findings and thermodynamic modelling. *Cement and Concrete Research, 40*(8), 1239-1247. doi://doi.org/10.1016/j.cemconres.2009.08.014

XTreeE. (n.d.). The large-scale 3D. Retrieved from https://www.xtreee.eu/news/

Young, J. F. (1972). *A review of the mechanisms of set-retardation in portland cement pastes containing organic admixtures* doi://doi.org/10.1016/0008-8846(72)90057-9

Zareiyan, B., & Khoshnevis, B. (2017). Effects of interlocking on interlayer adhesion and strength of structures in 3D printing of concrete. *Automation in Construction, 83*, 212-221.

doi://doi.org/10.1016/j.autcon.2017.08.019

Zhang, C., Hou, Z., Chen, C., Zhang, Y., Mechtcherine, V., & Sun, Z. (2019). Design of 3D printable concrete based on the relationship between flowability of cement paste and optimum aggregate content. *Cement and Concrete Composites, 104*, 103406. doi://doi.org/10.1016/j.cemconcomp.2019.103406

7. Appendices

Appendix A: Mixing Procedures

Prior to mixing, all Portland cement was sieved through a number 30 sieve to separate out any hydrated clumps. All sand was also sieved through a number 8 sieve with a maximum particle size of 2.36mm. Mixing procedures for each set of mix designs are as follows:

Base Mixtures:

1. Mix dry materials (sand, silica fume, and cement) on setting two (113 RPM) for 2:00 minutes
2. Use a spatula to scrape the contents off the side of the bowl
3. Add 1/2 water and mix on setting three (207 RPM) for 3:00 minutes
4. Use a spatula to scrape the contents off the side of the bowl
5. Add rest of water and mix on setting three (207 RPM) for 3:00 minutes

Superplasticizer Mixtures:

1. Mix dry materials on setting two (113 RPM) for 2:00 minutes
2. Use a spatula to scrape the contents off the side of the bowl
3. Combine the superplasticizer with the water
4. Add half of the water-superplasticizer solution and mix on setting three (207 RPM) for 3:00 minutes
5. Use a spatula to scrape the contents off the side of the bowl
6. Add second half of the water-superplasticizer solution and mix on setting three (207 RPM) for 3:00 minutes

PVA Fiber Mixtures:

1. Mix dry materials on setting two (113 RPM) for 2:00 minutes
2. Use a spatula to scrape the contents off the side of the bowl
3. Combine the superplasticizer with the water
4. Add half of the water-superplasticizer solution and mix on setting three (207 RPM) for 3:00 minutes
5. Use a spatula to scrape the contents off the side of the bowl
6. Add second half of the water-superplasticizer solution and mix on setting three (207 RPM) for 3:00 minutes
7. Break up the clumps of PVA fibers by hand
8. Add fibers in small doses to the mix while mixing on setting one (61 RPM)
9. Once all fibers are added, mix contents on setting two (113 RPM) for 1:00 minute

Acti-Gel Mixtures:

1. Mix dry materials on setting two (113 RPM) for 2:00 minutes
2. Use a spatula to scrape the contents off the side of the bowl
3. Combine the superplasticizer with the water
4. Add half of the water-superplasticizer solution and mix on setting three (207 RPM) for 3:00 minutes

5. Use a spatula to scrape the contents off the side of the bowl
6. Add second half of the water-superplasticizer solution and mix on setting three (207 RPM) for 3:00 minutes
7. Break up the clumps of PVA fibers by hand
8. Add fibers in small doses to the mix while mixing on setting one (61 RPM)
9. Once all fibers are added, mix contents on setting two (113 RPM) for 1:00 minute
10. Add the liquid Acti-Gel and mix onsetting two for 2:00 minutes

PAM Mixtures:

1. Mix dry materials on setting two (113 RPM) for 2:00 minutes
2. Use a spatula to scrape the contents off the side of the bowl
3. Combine the superplasticizer with the water
4. Add half of the water-superplasticizer solution and mix on setting three (207 RPM) for 3:00 minutes
5. Use a spatula to scrape the contents off the side of the bowl
6. Add second half of the water-superplasticizer solution and mix on setting two (113 RPM) for 3:00 minutes
7. Break up the clumps of PVA fibers by hand
8. Add fibers in small doses to the mix while mixing on setting one (61 RPM)
9. Once all fibers are added, mix contents on setting two (113 RPM) for 1:00 minute
10. Add PAM slowly to the mix on setting stir (33 RPM)
11. Once all PAM is added mix on setting two (113 RPM) for 4:00 minutes
12. Add excess water and mix on setting two (113 RPM) for 5:00 minutes
13. Use a spatula to scrape the contents off the side of the bowl
14. Mix contents on setting two (113 RPM) for 5:00 minutes

Appendix B: Base Mix Designs

Mixture Label	Cement (g/L)	Silica Fume (g/L)	Sand (g/L)	Water (g/L)	W/B
1. B575SF	529.0	46.0	1500.0	185.0	0.322
2. B443SF	400.0	43.0	1585.0	200.0	0.451
3. B515SF	477.0	38.0	1418.0	245.0	0.476
4. B485SF	447.0	38.0	1418.0	245.0	0.505
5.B500SF	450.0	50.0	1515.0	240.0	0.480
6. B485SF	447.0	38.0	1418.0	245.0	0.505
7. B508SF	457.0	51.0	1366.0	295.0	0.581

Notes	
1.	Natural sand. Mix not workable at all. Added 483g of water then scrapped the mix
2.	Natural sand. Not workable. Sandy. Added 400g of cement and 341g of water
3.	Natural sand. Not workable enough. Segregated during cylinder slump: water on bottom dry on top
4.	Grade 50 play sand. 1" cylinder slump. Very fine sand made mix very workable
5.	Fine Sand. Too much sand, not enough water/cement. Dry, not flowable at all
6.	Fine Sand. Not as workable as with play sand. Added 40g of water. Final cylinder slump of 0"
7.	Fine Sand. Cylinder slump of 1/4". Best STD mix. Decently workable, uniform throughout; held together well in cylinder

Appendix C: Superplasticizer Mix Designs

Mixture Label	Cement (g/L)	Silica Fume (g/L)	Fine Sand (g/L)	Water (g/L)	W/B	Superplasticizer (g/L)
8. B650SP0.8	598.0	52.0	1455.0	170.0	0.262	5.2 (0.8%)
9. B850SP0.8	782.0	68.0	1195.0	183.0	0.215	6.25 (0.8%)
10.B871SP0.8	792.0	79.0	1252.0	256.0	0.294	6.4 (0.8%)
11.B748SP0.8	673.0	75.0	1318.0	240.0	0.321	6.0 (0.8%)
12. B748SP1.0	673.0	75.0	1318.0	240.0	0.321	7.5 (1.0%)
13. B732SP1.0	659.0	73.0	1295.0	245.0	0.335	7.3 (1.0%)
14. B726SP1.0	653.0	73.0	1306.0	243.0	0.335	7.3 (1.0%)
15. B719SP1.0	647.0	72.0	1317.0	241.0	0.335	7.2 (1.0%)
16. B707SP1.0	636.0	71.0	1338.0	237.0	0.335	7.1 (1.0%)

Notes
8.Scrapped the Mix. Basically Dirt
9. Scrapped the Mix. Basically Dirt. Tried again but using 255g of water: still not workable. Added 21.3g twice then way too soupy. Tried Mix again with mixing in 0.5 water/SP at a time and ended with final water of 276g, cylinder slump of 3/8". Lots of open pores
10. Low workability, very sandy. Moisture seeped to bottom of cylinder. Tried this mix again but mixed sand with half water/SP then binders, then the second half of water/SP. Added 8.7g of water twice. 3/8" cylinder slump. Good consistency even moisture
11. 1/16" cylinder slump. On the dry side, pretty porous. Held shape well but hard, not pumpable
12. 1/16" cylinder slump. Almost the same consistency as above. A little wetter and less porous but still not pumpable
13. 3/16" cylinder slump. Best SP mix yet. Definitely pumpable, good consistency, no segregation, Not porous
14. 3/16" cylinder slump. very similar to the last mix but slightly more pumpable
15. 3/16" cylinder slump. Looked slightly dryer but cylinder came up easily and it felt pretty wet. Held together very well and good consistency throughout.
16. 1/4" slump for 4" cylinder. Wet, definitely pumpable, no segregation, looked good, slightly more workable than others.
Increasing sand seems to improve workability

Appendix D: PVA Fiber Mix Designs

Mixture Label	Cement (g/L)	Silica Fume (g/L)	Fine Sand (g/L)	Water (g/L)	W/B	Superplasticizer (g/L)	8mm PVA Fiber (g/L)
17. B732SP1.0PVA 0.5	659.0	73.0	1295.0	245.0	0.335	7.3 (1.0%)	6.45 (0.5%)
18. B732SP1.2PVA 0.5	659.0	73.0	1295.0	245.0	0.335	8.8 (1.2%)	6.45 (0.5%)
19. B710SP1.2PVA 0.5	639.0	71.0	1315.0	245.0	0.345	8.5 (1.2%)	6.45 (0.5%)
20. B690SP1.2PVA 0.5	621.0	69.0	1333.0	245.0	0.355	8.3 (1.2%)	6.45 (0.5%)
21. B710SP1.2PVA 0.25	639.0	71.0	1315.0	245.0	0.345	8.5 (1.2%)	3.23 (0.25%)
22. B690SP1.2PVA 0.25	621.0	69.0	1333.0	245.0	0.355	8.3 (1.2%)	3.23 (0.25%)
23. B671SP1.2PVA 0.25	604.0	67.0	1350.0	245.0	0.365	8.05 (1.2%)	3.23 (0.25%)
24. B653SP1.2PVA 0.25	588.0	65.0	1366.0	245.0	0.375	7.8 (1.2%)	3.23 (0.25%)

Notes
17. 1/16" cylinder slump; held together super well; Not quite pumpable, needs more SP or higher w/b ratio
18. 1/16' cylinder slump; Basically the same so increase w/b and then vary sand content
19. 1/8" cylinder slump; a little bit more workable but still probably not pumpable; held together like glue; might be too much fiber
20. 1/4" cylinder slump; more workable, possible pumpable, decrease the amount of fibers to 0.25% by total volume
21. 1/2"cylinder slump; much more workable; consistency of play doh but wet; definitely could be pumped; not porous, good consistency
22. 3/8” cylinder slump; about the same consistency as the one before; good mix

23. 1/2" cylinder slump; a little bit more workable but same consistency and slump behavior as past two mixes
24. 1/4" cylinder slump; odd; we expected the slump to increase; it did look wetter on the outside though

Appendix E: VMA Mix Designs

Mixture Label	Cement (g/L)	Silica Fume (g/L)	Fine Sand (g/L)	Water (g/L)	W/B	Superplasticizer (g/L)	PVA Fiber (g/L)	PAM (g/L)	Acti-Gel (g/L)
25. B653SP1.2 AG0.2	588.0	65.0	1366.0	245.0	0.375	7.8 (1.2%)	3.23 (0.25%)	-	4.04 (0.2%)
26. B653SP1.2 AG0.56	588.0	65.0	1366.0	245.0	0.375	8.3 (1.3%)	3.23 (0.25%)	-	11.31 (0.56%)
27. B671SP1.2 AG0.6	604.0	67.0	1350.0	245.0	0.365	8.1 (1.2%)	3.23 (0.25%)	-	12.13 (0.6%)
28. B671SP1.2 AG1.2	604.0	67.0	1350.0	245.0	0.365	8.1 (1.2%)	3.23 (0.25%)	-	24.25 (1.2%)
29. B653SP1.8 AG0.6	588.0	65.0	1366.0	245.0	0.375	11.8 (1.8%)	3.23 (0.25%)	-	12.11 (0.6%)
30. B671SP1.8 AG0.6	604.0	67.0	1350.0	245.0	0.365	12.1 (1.8%)	3.23 (0.25%)	-	12.13 (0.6%)
31. B671SP1.6 AG0.6	604.0	67.0	1350.0	245.0	0.365	10.7 (1.6%)	3.23 (0.25%)	-	12.13 (0.6%)
32. B690SP1.6 AG0.6	621.0	69.0	1333.0	245.0	0.355	11.0 (1.6%)	3.23 (0.25%)	-	12.14 (0.6%)
33. B671SP1.6 AG0.8	604.0	67.0	1350.0	245.0	0.365	10.7 (1.6%)	3.23 (0.25%)	-	16.17 (0.8%)
34. B671SP1.6 AG1.0	604.0	67.0	1350.0	245.0	0.365	10.7 (1.6%)	3.23 (0.25%)	-	20.21 (1.0%)
35. B671SP1.6 PAM9.0	604.0	67.0	1350.0	245.0	0.365	10.7 (1.6%)	3.23 (0.25%)	60.39 (9.0%)	-
36. B671SP1.6 PAM0.9	604.0	67.0	1350.0	245.0	0.365	10.7 (1.6%)	3.23 (0.25%)	6.04 (0.9%)	-
37. B571.2SP1.6PAM0.9	514.2	57.0	1149.6	357.0	0.625	9.1 (1.6%)	3.23 (0.25%)	5.14 (0.9%)	-

38. B571.2SP1.8PAM0.9	514.2	57.0	1149.6	357.0	0.625	10.3 (1.8%)	3.23 (0.25%)	5.14 (0.9%)	-
39. B571.2SP2.0PAM0.9	514.2	57.0	1149.6	357.0	0.625	11.4 (2.0%)	3.23 (0.25%)	5.14 (0.9%)	-
40. B571.2SP1.6PAM0.9	514.2	57.0	1149.6	357.0	0.625	9.1 (1.6%)	3.23 (0.25%)	5.14 (0.9%)	-
41. B553.5SP1.6PAM0.9	498.2	55.3	1165.6	357.0	0.645	8.9 (1.6%)	3.23 (0.25%)	4.98 (0.9%)	-
42. B571.2SP1.6PAM0.6	514.2	57.0	1149.6	357.0	0.625	9.1 (1.6%)	3.23 (0.25%)	3.43 (0.6%)	-
43. B571.2SP1.6PAM0.87	514.2	57.0	1149.6	357.0	0.625	9.1 (1.6%)	3.23 (0.25%)	5.00 (0.87%)	-
44. B571.2SP1.6PAM0.2	514.2	57.0	1149.6	357.0	0.625	9.1 (1.6%)	3.23 (0.25%)	1.14 (0.2%)	-
45. B571.2SP1.6PAM0.1	514.2	57.0	1149.6	357.0	0.625	9.1 (1.6%)	3.23 (0.25%)	0.57 (0.1%)	-
46. B571.2SP1.6PAM0.075	514.2	57.0	1149.6	357.0	0.625	9.1 (1.6%)	3.23 (0.25%)	0.43 (0.075%)	-
47. B571.2SP1.6PAM0.08	514.2	57.0	1149.6	357.0	0.625	9.1 (1.6%)	3.23 (0.25%)	0.46 (0.08%)	-
48. B571.2SP1.6PAM0.9	514.2	57.0	1149.6	357.0	0.625	9.1 (1.6%)	3.23 (0.25%)	5.14 (0.9%)	-
49. B571.2SP1.6PAM0.9	514.2	57.0	1149.6	357.0	0.625	9.1 (1.6%)	3.23 (0.25%)	5.14 (0.9%)	-
50. B571.2SP1.6PAM0.9	514.2	57.0	1149.6	357.0	0.625	9.1 (1.6%)	3.23 (0.25%)	5.14 (0.9%)	-
51. B571.2SP1.6PAM0.45	514.2	57.0	1149.6	357.0	0.625	9.1 (1.6%)	3.23 (0.25%)	2.57 (0.45%)	-
52.	514.2	57.0	1149.6	357.0	0.625	9.1 (1.6%)	3.23	3.43	-

B571.2SP1.6PAM0.6							(0.25%)	(0.6%)	

Notes
25. 1/4" cylinder slump; try more ActiGel; couldn't see any significant change from mix without ActiGel
26. 3/16" cylinder slump; best mix yet; high workability; low slump; maybe try lower ActiGel but lower W/B ratio
27. 3/16" cylinder slump; looked dry but then felt more pumpable than the PVA mix only; Solid mix
28. 1/16" cylinder slump; too stiff: ActiGel reduces slump; first trial with the 4cm x 1cm nozzle, did not pump at all; need a bigger nozzle area; too much reduction
29. 1 1/4" cylinder slump; most workable mix by far; using more SP is definitely better; extruded through the 4cm x 2cm nozzle
30. 15/16" cylinder slump; a little bit less workable than the last mix; still visually wet; printed well out of 4cm x 2cm nozzle; almost too easy, may not hold up to buildability; lower SP
31. 1/2" cylinder slump; nice and wet; good consistency; pumped well; try increasing ActiGel to see if it still pumps or lower W/B
32. 9/16" cylinder slump; very workable; harder to start pumping but extruded easily after getting started; definitely harder to pump though; not as much surface moisture on the printed filament
33. 3/8" cylinder slump; still pumped very well; well controlled filament; stood up better
34. 1/4" cylinder slump; workable and pumpable but concerned the it would get stuck in the pump; use B671SP1.6AG0.6 and B671SP1.6AG0.8
35. Consistency of dirt; added an additional 122.5g of water and it turned into one giant ball of flubber
36. Added 174.2 g of excess water in total after mixing for a final W/B of 0.625; Printed extremely well; sticky but also slippery; pumped with ease.
37. This was the last mix converted into g/L; 3/8" cylinder slump; sticks together so well that it has gaps in it from rodding; A little harder to pump than the last one; the consistency with PAM is entirely dependent on mixing time and mixing procedure
38. 1/4" cylinder slump; this was not extrudable; felt almost dry; barely pumpable by hand; confusing because less SP extruded better
39. Small trial mixture; Still too dry; need more water
40. Tried B571.2SP1.6PAM0.9 again but added 5.71g (0.01 W/B) until it looked good; One dose of water significantly changed it from dry to pumpable; second dosage got it almost perfect; final W/B of 0.645
41. 1/8" cylinder slump; Had to add an additional 5.5g of water in order to pump because it was too dry; allow it to pump but still not acceptably pumpable; Mix stiffened very quickly after ceasing mixing; Try less PAM
42. Could not pump this at all; Dried up so fast; looked okay initially but then turned very dry
43. Changed the Mix procedure to adding PAM at the end; Scraped this mix: turned into dirt
44. Added PAM in 0.57g dosages at the end: first 5.71g, Still soupy, starting to change; second 0.57g,

turned too dry; scraped
45. Tried the same mix design but after adding the first 0.57g of PAM mixed for longer and the mix turned too dry; mixing time affects the consistency significantly
46. Tried the same mix design adding PAM in smaller doses and mixing for longer in between; looked good
47. Same consistency as the previous but a little stickier; still wet looking, but too sandy; Not enough PAM to get the type of filament we had before
48. 2nd try at this mix design with new mixing procedures; Seemed like the PAM worked best when water was added at the end, so 1/3 of the water/SP was saved until the end and added after the PAM was mixed in; Still dry like dirt; added 11.42g of excess water - 11.5mm cylinder slump; put it back in mixer and mixed another 11.42g of water - 10.5mm cylinder slump; no change
49. 3rd try at this mix design but added 28.55g of excess water at the end. 28.5mm cylinder slump; much wetter and slimier than when we added the water slowly; pumped easily almost too wet; try less excess water
50. 4th try at this mix design; added 25.70g of excess water; 29mm cylinder slump; sticky but good surface finish; slightly less soupy; consistency of churned butter
51. Added 17.13g of excess water; not enough water; hardened fast; try 0.6% PAM
52. Added 22.84g of excess water; churned butter; similar to the 0.9% PAM mix

Appendix F: Viscometry Raw Data for Acti-Gel 0.6%

Spindle	Spindle radius	RPM	Final reading [% torque]	Viscosity [Pa.s]	Shear rate [s-1]
6	7.3	0.3	63.8	2127	0.064706561
6	7.3	0.5	51.8	1036	0.107844269
6	7.3	0.6	59.5	991.7	0.129413122
6	7.3	1	57.7	577	0.215688537
6	7.3	1.5	64.3	428.7	0.323532806
6	7.3	2	68.4	342	0.431377074
6	7.3	2.5	67.7	270.8	0.539221343
6	7.3	3	67.8	226	0.647065611
6	7.3	4	71.5	178.8	0.862754148
6	7.3	5	72.9	145.8	1.078442685
6	7.3	6	72.4	120.7	1.294131222
6	7.3	10	72.5	72.5	2.15688537
6	7.3	12	74.2	61.83	2.588262444
6	7.3	20	76.3	38.3	4.31377074
6	7.3	30	77.8	25.93	6.47065611
6	7.3	50	86.4	17.28	10.78442685

6	7.3	60	85.9	14.32	12.94131222
6	7.3	100	94.1	9.41	21.5688537

Appendix G: Viscometry Raw Data Acti-Gel 0.8%

Spindle	Spindle radius	RPM	Final reading [% torque]	Viscosity [Pa.s]	Shear rate [s-1]
6	7.3	0.3	55.6	1853	0.064706561
6	7.3	0.5	56.4	1128	0.107844269
6	7.3	0.6	71.4	1190	0.129413122
6	7.3	1	76.6	766	0.215688537
6	7.3	1.5	81	540	0.323532806
6	7.3	2	85.4	427	0.431377074
6	7.3	2.5	79.6	318.4	0.539221343
6	7.3	3	70.5	235	0.647065611
6	7.3	4	78.1	195.3	0.862754148
6	7.3	5	78.4	156.8	1.078442685
6	7.3	6	76.6	127.7	1.294131222
6	7.3	10	66.7	66.7	2.15688537
6	7.3	12	65.3	54.42	2.588262444
6	7.3	20	62.7	31.35	4.31377074
6	7.3	30	62.8	20.93	6.47065611
6	7.3	50	60.1	12.02	10.78442685

6	7.3	60	62.8	10.47	12.94131222
6	7.3	100	64	6.4	21.5688537

Appendix H: Viscometry Raw Data PAM 0.6%

Spindle	Spindle radius	RPM	Final reading [% torque]	Viscosity [Pa.s]	Shear rate [s-1]
6	7.3	0.3	58.1	1937	0.064706561
6	7.3	0.5	42	840	0.107844269
6	7.3	0.6	39.3	655	0.129413122
6	7.3	1	38.4	384	0.215688537
6	7.3	1.5	39	260	0.323532806
6	7.3	2	41.1	205.5	0.431377074
6	7.3	2.5	41.7	166.8	0.539221343
6	7.3	3	42.3	141	0.647065611
6	7.3	4	44	110	0.862754148
6	7.3	5	44.7	89.4	1.078442685
6	7.3	6	45.7	76.17	1.294131222
6	7.3	10	47.9	47.9	2.15688537
6	7.3	12	51.7	43.08	2.588262444
6	7.3	20	52.1	26.05	4.31377074
6	7.3	30	54.5	18.17	6.47065611
6	7.3	50	56	11.2	10.78442685

6	7.3	60	65.6	10.93	12.94131222
6	7.3	100	66.8	6.68	21.5688537

Appendix I: Viscometry Raw Data PAM 0.9%

Spindle	Spindle radius	RPM	Final reading [% torque]	Viscosity [Pa.s]	Shear rate [s-1]
6	7.3	0.3	69.5	2317	0.064706561
6	7.3	0.5	67.2	1344	0.107844269
6	7.3	0.6	69.2	1153	0.129413122
6	7.3	1	75.3	753	0.215688537
6	7.3	1.5	78.3	522	0.323532806
6	7.3	2	79.8	399	0.431377074
6	7.3	2.5	82	328	0.539221343
6	7.3	3	83.1	277	0.647065611
6	7.3	4	84.3	210.8	0.862754148
6	7.3	5	84.4	168.8	1.078442685
6	7.3	6	82.8	138.8	1.294131222
6	7.3	10	79.5	79.5	2.15688537
6	7.3	12	81.3	67.75	2.588262444
6	7.3	20	80.2	40.1	4.31377074
6	7.3	30	82.9	27.63	6.47065611
6	7.3	50	85.1	17.02	10.78442685

6	7.3	60	85.6	14.27	12.94131222
6	7.3	100	95.6	9.56	21.5688537

Appendix J: Viscometry Raw Data Base Mix Design

Spindle	Spindle radius	RPM	Final reading [% torque]	Viscosity [Pa.s]	Shear rate [s-1]
6	7.3	0.3	29.4	980	0.064706561
6	7.3	0.5	32.5	650	0.107844269
6	7.3	0.6	36.7	611.7	0.129413122
6	7.3	1	38.7	387	0.215688537
6	7.3	1.5	37.7	251.3	0.323532806
6	7.3	2	36.9	184.5	0.431377074
6	7.3	2.5	35.7	142.8	0.539221343
6	7.3	3	36.8	122.7	0.647065611
6	7.3	4	38.1	95.25	0.862754148
6	7.3	5	35.2	70.4	1.078442685
6	7.3	6	37.7	62.83	1.294131222
6	7.3	10	38.7	38.7	2.15688537
6	7.3	12	35.2	29.33	2.588262444
6	7.3	20	33.9	16.95	4.31377074
6	7.3	30	30.3	10.1	6.47065611
6	7.3	50	37.9	7.58	10.78442685

6	7.3	60	35.6	5.93	12.94131222
6	7.3	100	38.3	3.83	21.5688537

Appendix K: Compression Testing Graphs

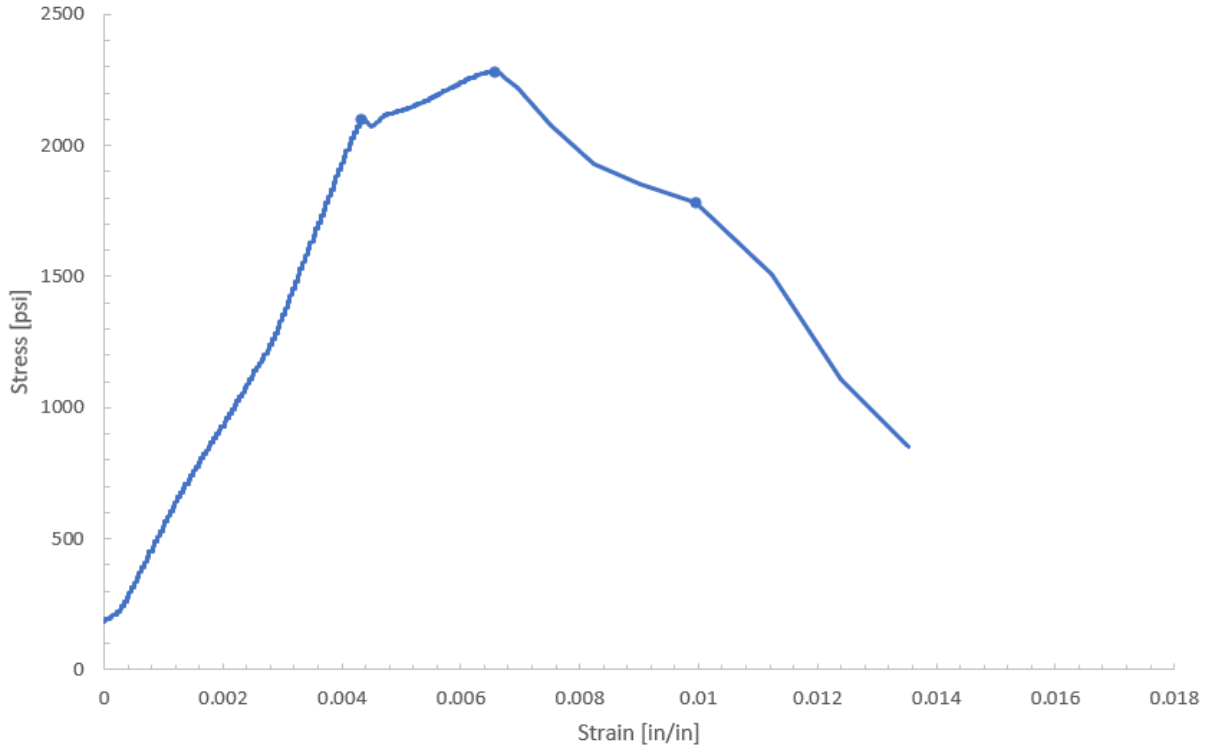

Stress-strain plot for compression test on base mix

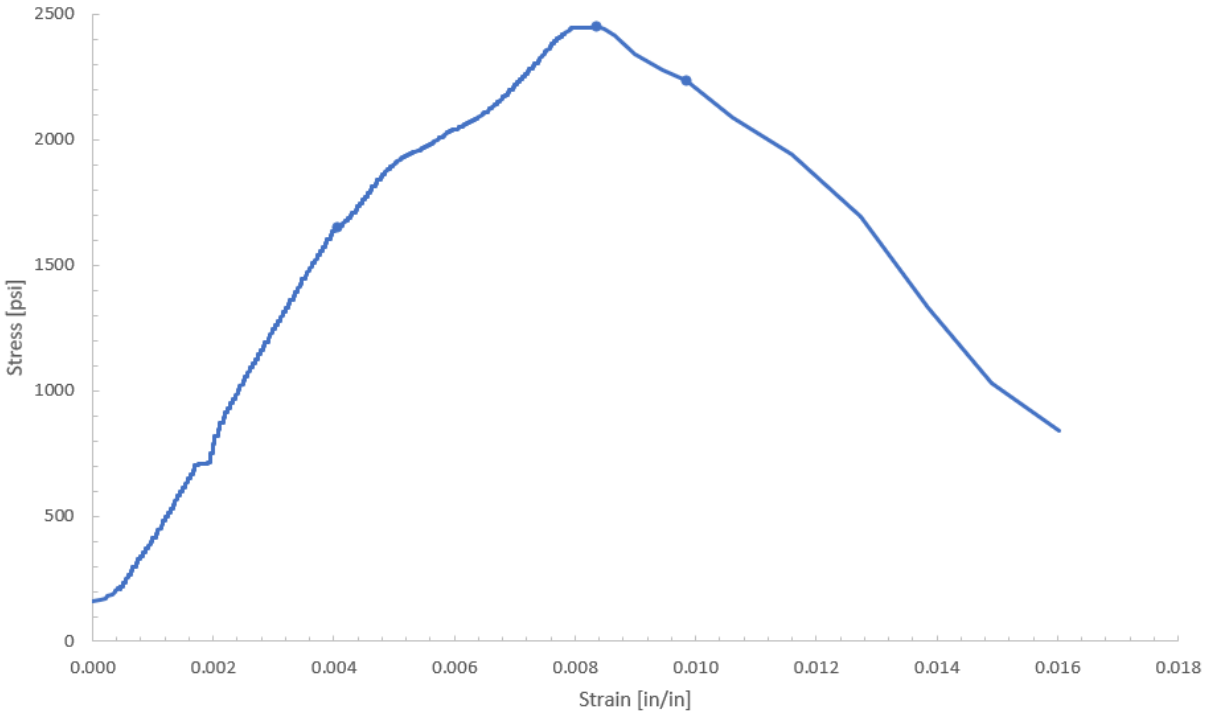

Stress-strain plot for compression test on Acti-Gel 0.6%

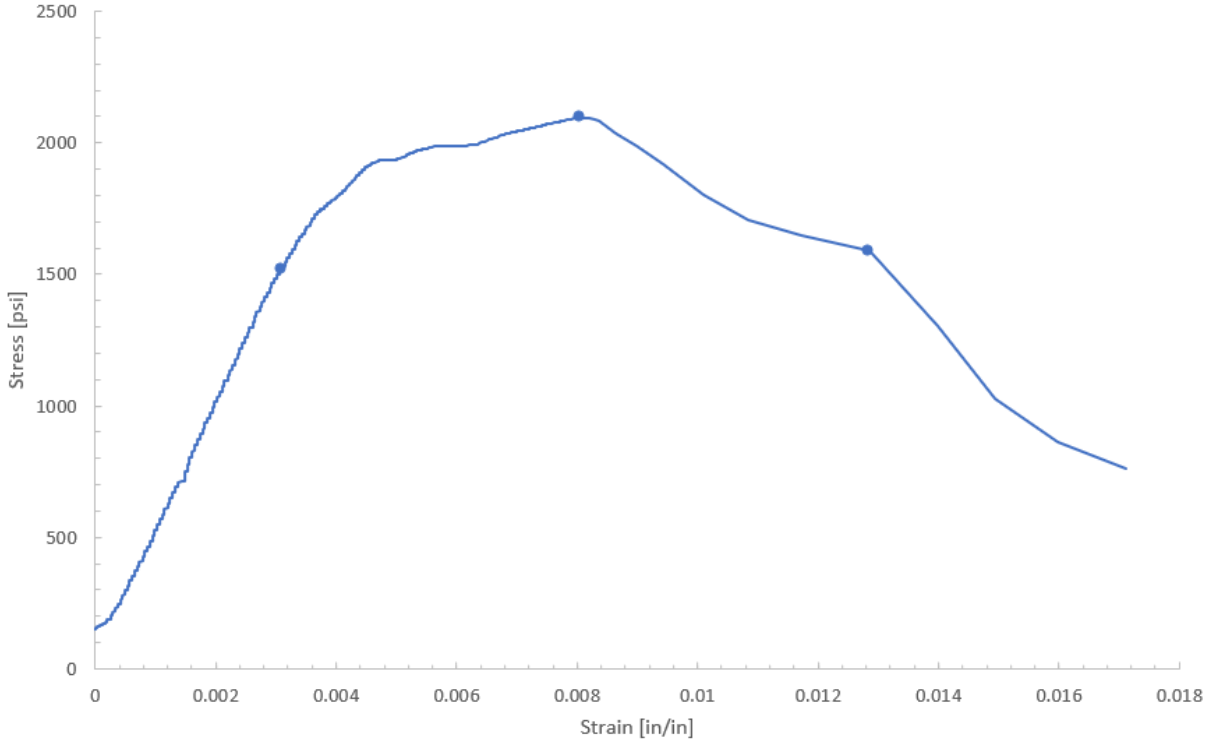

Stress-strain plot for compression test on Acti-Gel 0.8%

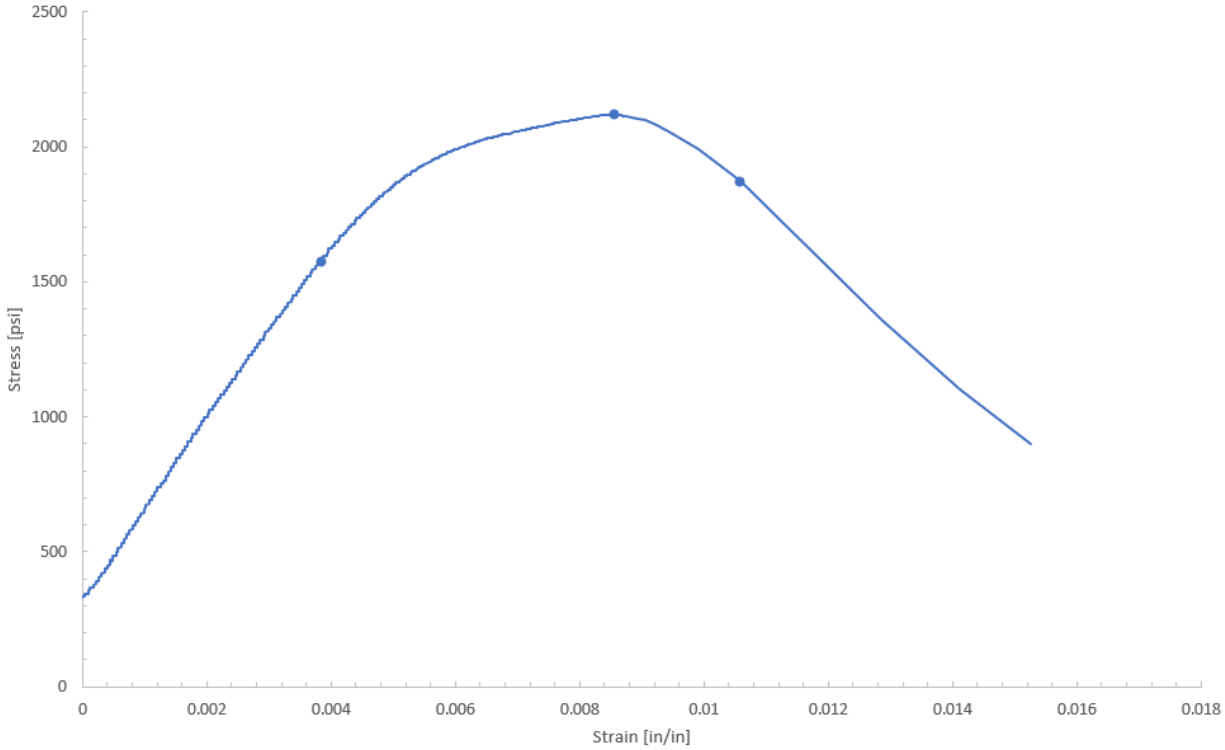

Stress-strain plot for compression test on PAM 0.6%

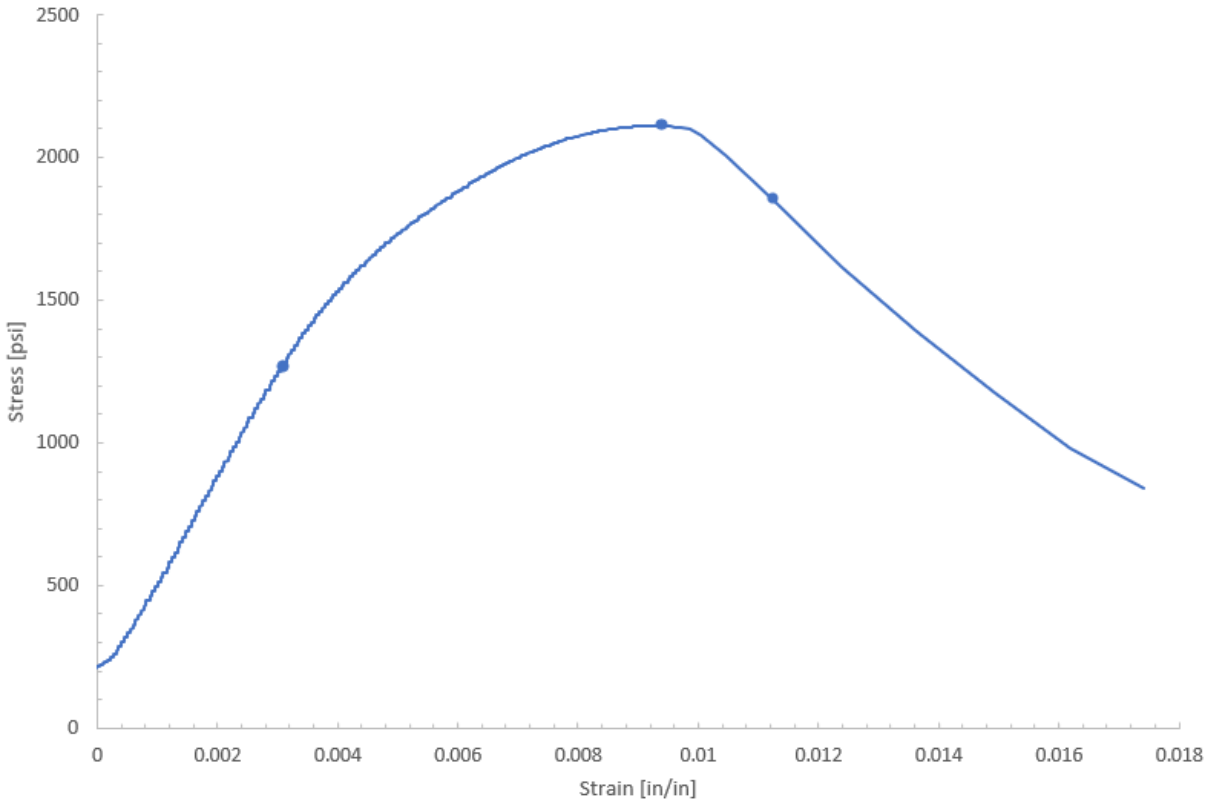

Stress-strain plot for compression test on PAM 0.9%

Appendix L: Brazil disk test data

Raw Data for Round 1 of Brazilian disk test samples

Load Angle 0 (Round 1)					
Sample	Avg Diameter [in]	Avg Height [in]	Peak Load [Lbf]	Splitting Tensile Strength (psi)	Fracture Toughness (J/m^2)
Control Full	3.909333333	1.688333333	9421	908.6910053	N/A
Control Flat Interface	3.900666667	1.657	6261	616.683714	5637.1
Adhesive	3.875	1.570666667	4008	419.2297575	2598.9
5A	3.893	1.701333333	3318	318.9206863	1541.1
5B	3.884	1.623333333	3948	398.6303301	2400.1
5C	3.902333333	1.677333333	4407	428.6269088	2664.4
3A	3.901	1.656666667	4244	418.065581	2590
3B	3.877666667	1.655333333	4735	469.6173921	3289.8
3C	3.901666667	1.674333333	2783	271.2072172	1113.8
1A	3.877	1.662	5489	542.3086521	4421
1B	3.895	1.643	2451	243.8250987	881.4941
1C	3.906	1.649666667	3675	363.0856027	1942.8

Raw Data for Round 2 of Brazilian disk test samples

Load Angle 0 (Round 2)					
Sample	Avg Diameter [in]	Avg Height [in]	Max Load [lbf]	Splitting Tensile Strength (psi)	Fracture Toughness (J/m^2)
Control Full	3.878	1.592	6392	659.122324	N/A
Control Flat Interface	3.884	1.657	2311	228.6011121	783.6259
Adhesive	3.869333333	1.547666667	3905	415.133315	2594.9
5A	3.876666667	1.565	2457	257.8175503	976.6669
5B	3.874	1.561666667	3011	316.8421281	1466.7
5C	3.884333333	1.561333333	3215	337.4807276	1672.1
3A	3.861	1.580333333	3550	370.3906149	2038.7
3B	3.850333333	1.557333333	2892	307.0425068	1353.1
3C	3.873333333	1.558	2051	216.3682122	680.5291
1A	3.860333333	1.598333333	2410	248.659469	894.3911
1B	3.861333333	1.565666667	2093	220.4005895	708.6911
1C	3.88	1.558333333	1799	189.4171074	523.5731

Raw Data for Round 3 of Brazilian disk test samples

Load Angle 25 (Round 3)				
Sample	Avg Diameter [in]	Avg Height [in]	Max Load [lbf]	Fracture Toughness (J/m^2)
Control Full	3.885666667	1.572666667	9459	N/A
Control Flat Interface	3.882	1.549	3340	1999.9
Adhesive	3.843333333	1.585666667	1619	446.7302
5A	3.885666667	1.595333333	3429	1907.3
5B	3.880333333	1.606666667	2665	1152.1
5C	3.899666667	1.615666667	3082	1510.1
3A	3.887	1.609333333	5495	4898.3
3B	3.861	1.620333333	4779	3704.9
3C	3.887333333	1.616666667	7406	8897.7
1A	3.874	1.569333333	3951	2660.5
1B	3.878666667	1.582666667	4186	2986.3
1C	3.882333333	1.599666667	2940	1402.1

Raw Data for Round 4 of Brazilian disk test samples

Load Angle 25 (Round 4)				
Sample	Avg Diameter [in]	Avg Height [in]	Max Load [lbf]	Fracture Toughness (J/m^2)
Control Full	3.882666667	1.572666667	5169	N/A
Control Flat Interface	3.882666667	1.586	3309	1866
Adhesive	3.834	1.564333333	942	151.2347
5A	3.867333333	1.589333333	2742	1281.3
5B	3.858	1.604333333	3396	1870.8
5C	3.864	1.591	2568	1123.8
3A	3.855666667	1.589	3887	2574.9
3B	3.846	1.600666667	2670	1156.4
3C	3.863	1.593333333	3540	2135.8
1A	3.86	1.592333333	4452	3377.9
1B	3.869666667	1.613666667	4812	3756.3
1C	3.864	1.567333333	3282	1835.7

Appendix M: Testing Schedule

OCTOBER 2019						
Sunday	Monday	Tuesday	Wednesday	Thursday	Friday	Saturday
29	30	1	2	3	4	5
6	7	8	9	10	11	12
13	14	15	16	17	18	19
20	21	22	23	24 Make AG Cyl.	25	26
27	28 Make PAM Cyl. BDT set #1	29	30 Make PAM Cyl. Print SEM Samples	31 BDT set #2	1	2

NOVEMBER 2019

Sunday	Monday	Tuesday	Wednesday	Thursday	Friday	Saturday
27	28 BDT set #1	29	30 Print SEM Samples	31	1	2 BDT set #2
3	4	5 Break BDT set #1	6 Cut/Dry SEM Samples	7 Test AG0.6 & AG0.8 Cyl.	8 Make Base Cyl. BDT set #3	9
10 Test BDT set #2 BDT set #4	11 Test PAM0.6 Cyl. SEM on Prints	12	13 Break PAM0.9 Cyl.	14	15	16 Break BDT set #3
17	18 Break BDT set #4	19	20	21	22 Break Base Cyl.	23
24	25	26	27	28	29	30